The Dissertation Committee for Daniel Lee Worthington certifies that this is the approved version of the following dissertation:

Characteristics of Dynamic Abnormal Grain Growth In Commercial-Purity Molybdenum

Committee:

Eric M. Taleff, Supervisor

Todd Ditmire

Desiderio Kovar

Llewellyn K. Rabenberg

Kenneth M. Ralls

Characteristics of Dynamic Abnormal Grain Growth In Commercial-Purity Molybdenum

by

Daniel Lee Worthington, B.S.

Dissertation

Presented to the Faculty of the Graduate School of

The University of Texas at Austin

in Partial Fulfillment

of the Requirements

for the Degree of

Doctor of Philosophy

The University of Texas at Austin

December 2011

Dedication

This dissertation is dedicated to my family:

Roland Worthington,

Susy Ting,

and

Brian Worthington.

Acknowledgements

I would like to acknowledge my adviser, Eric M. Taleff, for his persistent enthusiasm and guidance throughout my time at UT. A strong dedication to his students is one of his most outstanding qualities. I thank my committee members, Professors Ditmire, Kovar, Rabenberg, and Ralls, for their suggestions and advice, as well as their time and effort, in the review of this dissertation. I would also like to recognize the many students who I spent time with in the Taleff research group. I believe our research group shares a unique camaraderie and collaborative spirit. During frustrating moments in research, a little humor is great medicine.

Nick Pedrazas deserves special recognition for his invaluable assistance and advice on several experiments in this research. Furthermore, I am immensely grateful to Dr. Jim Ciulik who helped get me up to speed when I first began this project.

A few more thank-you's are in order: I thank Clarissa Peña for steering me through the program, Steve Sanders for his help on fixing instrumentation, Danny Jares for machining the test coupons, and Bassem El-Dasher of Lawrence Livermore National Laboratory for his assistance with Electron Backscatter Diffraction.

Characteristics of Dynamic Abnormal Grain Growth In Commercial-Purity Molybdenum

Daniel Lee Worthington, Ph.D.

The University of Texas at Austin, 2011

Supervisor: Eric M. Taleff

Abstract: Dynamic abnormal grain growth (DAGG) in commercial-purity molybdenum sheets was investigated through a series of tensile tests at temperatures between 1450°C and 1800°C. DAGG is abnormal grain growth (AGG) which requires the presence of concurrent plastic strain. Most AGG phenomena previously documented in the literature can be categorized as static abnormal grain growth (SAGG) because they occur during static annealing, sometimes following plastic strain, but do not occur during plastic deformation. The DAGG boundary migration rate is much faster than the SAGG boundary migration rate, and DAGG may be utilized to obtain large single crystals in the solid state. Dynamic abnormal grains were found to exhibit a crystallographic orientation preference with respect to the specimen geometry, generally described as derivative from a ⟨101⟩ fiber texture. DAGG was found to prefer growth on the surface of the specimen rather than the interior. The growth of dynamic abnormal grains, which initiated and grew during plastic strain, generally ceased when the application of plastic strain was removed. The DAGG boundary migration rate was found to be a direct function of plastic strain accumulation, regardless of the strain-rate. Therefore, it is hypothesized that the rapid boundary migration rate during DAGG results from an enhanced mobility of certain

boundaries. A model is proposed based on the rate of boundary unpinning, as mediated by the emission of dislocations from pinning sites.

Table of Contents

1 INTRODUCTION

Dynamic abnormal grain growth (DAGG) is a phenomenon which produces some abnormally large grains during plastic deformation at elevated temperature. It is the dynamic aspect of DAGG that distinguishes it from abnormal grain growth (AGG) phenomena previously documented in the literature [1, p.368-378, 2, p.113-117]. Those can be generally categorized as static abnormal grain growth (SAGG) because they occur during static annealing, sometimes following plastic strain, but do not occur during plastic deformation. Abnormal grain growth is defined as the rapid growth of a few, large *abnormal* grains at the expense of smaller surrounding grains in a microstructure. DAGG was observed in several commercial-purity molybdenum materials at elevated temperatures, generally greater than 1800 K [3-5], and has been used to produce quite large single crystals, several centimeters in length, in the solid state. It is the goal of this dissertation to develop a greater understanding of the mechanisms behind DAGG through further characterization of the phenomenon.

1.1 Motivation

Dynamic abnormal grain growth is a phenomenon of fundamental scientific importance. The specific cause(s) of AGG phenomena is not well understood, as noted by A. Rollett et al. [6]. The discovery of DAGG contributed to this understanding by delineating the important distinction between SAGG and DAGG phenomena. Further research, such as that contained in the present investigation, is necessary to better understand DAGG.

Dynamic abnormal grain growth is also of potential importance to technological applications. Recrystallized molybdenum exhibits nearly zero bend ductility at room temperature. This brittle behavior has limited the widespread use of molybdenum alloys

[7]. Although multiple reasons exist for embrittlement in molybdenum [7], oxygen segregation to grain boundaries is at least partially responsible [7-9, 10, p. 394-407]. As a result, brittle fracture at room temperature occurs at grain boundaries. A fracture surface depicting this behavior is shown in Figure 1-1. DAGG may be utilized to produce large single crystals of molybdenum in the solid state and eliminate grain boundaries completely. Figure 1-2a,b contains pictures of a molybdenum single crystal with a length of 2.5 cm produced through DAGG. This single crystal exhibited exceptional ductility, as demonstrated in Figure 1-2c by a 180º twist performed at room temperature.

Single crystals may also be desirable in high-temperature applications because of superior creep resistance. Tungsten filaments are used in resistive heating and incandescent lighting. These filaments creep under their own weight, and creep rupture occurs at grain boundaries [11-13]. For these applications, a coarse microstructure is intentionally produced in tungsten wire through SAGG to reduce the number of grain boundaries. It is known that the presence of a dispersed second phase generally promotes SAGG [1, p.293-304, 14]. For that reason, potassium bubbles are introduced into the microstructure. The largest abnormal grains produced through this SAGG technique are several millimeters in length [12]. Figure 1-3 is a picture of a single crystal of molybdenum wire produced through DAGG. The length of this molybdenum single crystal was 10 cm. DAGG may occur in other refractory metals (i.e. W, V, Nb, and Ta) because those metals have the same body-centered-cubic crystal structure as molybdenum. If DAGG occurs in tungsten, then a single crystal wire similar to the molybdenum wire of Figure 1-3 might also be produced in tungsten. Single crystal tungsten filaments could yield substantially longer service lives than the coarse-grained filaments currently used.

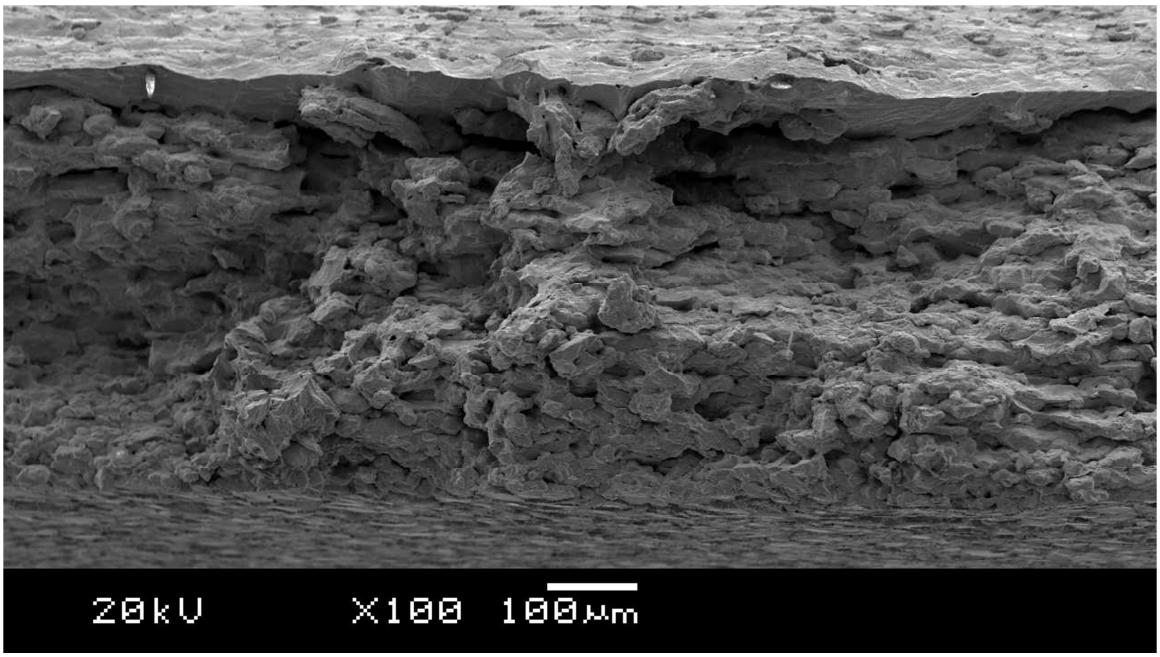

Figure 1-1: Scanning electron microscope micrograph of a recrystallized molybdenum fracture surface. The brittle fracture is intergranular and occurred at room temperature.

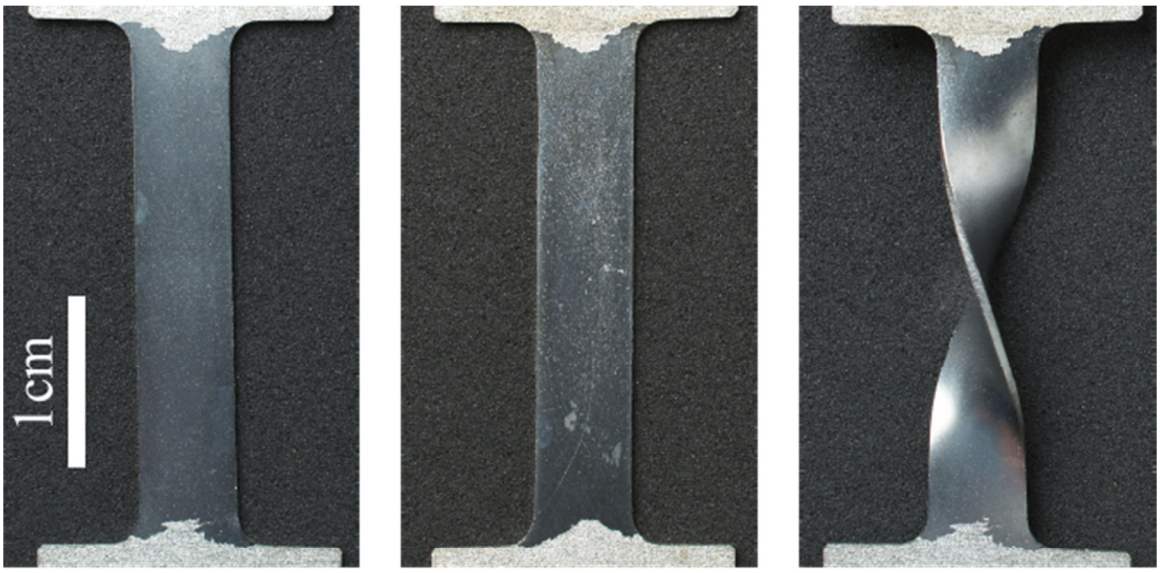

Figure 1-2: Demonstration of the room-temperature ductility of a molybdenum single crystal produced through DAGG. Pictured are (a) front face of Mo single crystal, (b) back face of Mo single crystal, and (c) Mo single crystal twisted 180°.

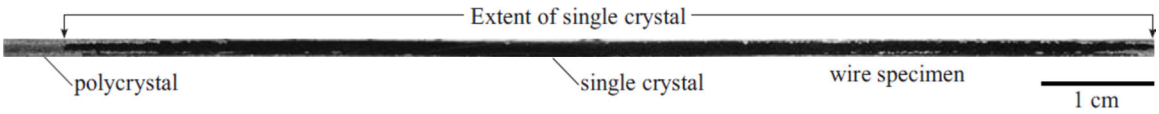

Figure 1-3: A single crystal of molybdenum wire produced through DAGG at 1740ºC and $10^{-4}s^{-1}$. The single crystal is approximately 10 cm in length.

Finally, a greater understanding of DAGG may assist in the prevention of AGG during hot deformation processing. Retention of a fine microstructure is often desirable to produce a high yield strength. The Hall-Petch equation describes this relationship between yield strength and grain size:

$$\sigma = \sigma_o + \frac{k_y}{\sqrt{d}} \quad , \tag{1-1}$$

where σ is the yield stress, σ_o is the yield stress of a single crystal, k_y is a material strengthening coefficient, and d is grain size. Abnormal grains can significantly reduce the strength of a metal or alloy by increasing d, an undesirable effect in many applications. Furthermore, abnormal grains are a potential source of fatigue failure in some applications, such as superalloy components in jet engines.

1.2 Goals of this Dissertation

The research for this dissertation was undertaken to resolve the following questions:

(1) What role does plastic strain play in the initiation of abnormal grains during DAGG? Separately, what role does plastic strain play in the propagation of the abnormal grain boundary during growth?

(2) Does selection of a particular grain to become an abnormal grain in DAGG depend upon a preferred crystallographic orientation or other properties?

(3) How does DAGG in molybdenum compare to SAGG in molybdenum? What is the boundary migration rate of DAGG relative to SAGG?

(4) What is the mechanism behind DAGG? Is the enhanced boundary migration associated with DAGG due to a difference in driving force or mobility?

2 REVIEW OF ANNEALING PHENOMENA

Static and dynamic restoration processes are reviewed in this chapter. The purpose of this review is to provide context for discussion of dynamic abnormal grain growth (DAGG). More detailed reviews of recrystallization and annealing phenomena can be found in the literature [1, 15].

Metals are plastically deformed during mechanical operations such as rolling, extrusion, and forging. Strain hardening occurs during deformation at cold ($T/T_M < 0.3$, where T_M is melting or solidus temperature) and warm ($0.3 < T/T_M < 0.5$) temperatures because of an increase in dislocation density with increased plastic strain accumulation. Hardening is less rapid with straining at warm temperatures, as elevated temperature allows some recovery (decrease in dislocation density, such as through annealing) during processing. As metals harden, they become less workable and more susceptible to fracture. In order to relieve the stored strain energy in a deformed microstructure, metals are either (1) cold-worked and subsequently annealed or (2) warm- or hot-worked. It is important to distinguish between static annealing phenomena in a previously deformed microstructure and dynamic restoration in a microstructure during hot deformation. Although similar processes are involved, the latter represents a more complex, dynamic microstructural evolution in which hardening and softening mechanisms occur concurrently.

2.1 Nomenclature

Within the last 20 years, terminology has been introduced which distinguishes uniform growth processes (*continuous*) from non-uniform processes (*discontinuous*), such as those involving nucleation and growth, during annealing [1, p.3, 15]. Recovery and normal grain growth are continuous processes; that is, these processes are largely

homogenous throughout the microstructure and occur "continuously." Abnormal grain growth is inherently a discontinuous process; that is, this process is governed by rapid growth of only a few grains, and growth of these few abnormal grains initiates inhomogenously within the microstructure. Meanwhile, recrystallization processes can be either continuous, such as in geometric-dynamic recrystallization [1, p.461-465], or discontinuous, such as in particle-stimulated nucleation of recrystallization [1, p.293-304]. Some refer to abnormal grain growth as secondary recrystallization because abnormal grain growth typically occurs after *primary* recrystallization of a microstructure. Thus, abnormal grain growth can be thought of as a type of discontinuous recrystallization. It is important to note that recrystallization and abnormal grain growth do not involve embryonic nucleation phenomena, at least with respect to a thermal fluctuation model. Nuclei are not clusters which form "atom-by-atom"; rather, they are existing crystallites in the material. Therefore, *initiation* may be a more accurate term than *nucleation* when discussing recrystallization and abnormal grain growth, although both terms are still widely used in the literature.

Processes that occur during plastic deformation, such as during hot working or creep deformation, are termed *dynamic*. Such is the case with dynamic recovery (DRV), dynamic recrystallization (DRX), dynamic (normal) grain growth (DGG), and dynamic abnormal grain growth (DAGG), the latter being the subject of this dissertation. Conversely, processes that are not concurrent with plastic deformation are termed *static*. Static annealing processes may be identified with the *static* prefix: static recovery (SRV), static recrystallization (SRX), static (normal) grain growth (SGG), and static abnormal grain growth (SAGG). This expanded nomenclature was proposed in a previous article [5] which first reported the DAGG phenomenon. DAGG is distinct from previously observed SAGG phenomena because plastic strain is required for both initiation and

propagation of DAGG. Moreover, DAGG is a phenomenon distinct from DRX for several reasons: (1) DAGG grains, i.e. abnormal grains which initiate *via* DAGG, are much larger than the largest observed grains produced through DRX [16, 17] (several centimeters vs. hundreds of millimeters), (2) DAGG occurs over a small true strain (stress drop occurs over ~0.01 strain), while DRX occurs over much larger true strains (0.1 – 0.5), and (3) further straining after DAGG results in plastic deformation of the newly formed abnormal grains but not in additional recrystallization, unlike in DRX.

2.2 Static Annealing

Plastic deformation usually increases the dislocation density in a metal, particularly at a low homologous temperature (i.e. $T/ T_M < 0.3$). Dislocations produce plastic strain and increase yield strength, i.e., dislocations cause hardening. Dislocations and other defects raise the Gibbs free energy of a crystalline solid because atoms deviate from their ideal lattice positions, and there is an increase in the number of broken atomic bonds. Although dislocations are thermodynamically unstable, they are retained at low temperatures after deformation. Elimination of dislocations decreases yield strength, i.e., causes softening. Mechanisms for the removal or reconfiguration of dislocations are often dependent upon atomic mobility and related thermally-activated processes. Although dislocation annihilation processes can occur without diffusion, the rate of softening from these is far outpaced by the effects of diffusive processes at elevated temperature. Thus, deformed metal is typically annealed at high temperatures to reduce dislocation density, reducing yield strength, through diffusion-assisted recovery processes.

Heat accounts for most of the work expended during plastic deformation, and only a small amount (~1%) is retained in the microstructure as stored strain energy [1,

p.13]. However, the defects introduced into a metal during plastic deformation significantly affect mechanical properties. A heavily cold-worked metal may have a dislocation density as high as 10^{16} m^{-2}, while a fully annealed metal may have a dislocation density as low as 10^{10} m^{-2}. The yield strength of a deformed metal may be several times higher than that of an annealed metal due to this difference in dislocation density [18, p.384]. The somewhat related effect of strengthening through grain size reduction is described by the Hall-Petch relationship (Equation 1-1), as grain boundaries can be modeled as arrays of dislocations. Softening of a deformed metal can occur through three static annealing processes: static recovery, static recrystallization, and static grain growth. Grain growth may be normal or abnormal, depending on the uniformity of the coarsening. These processes are traditionally described as follows.

2.2.1 RECOVERY

Recovery is annealing that retains the same grain microstructure while reducing dislocation density. Atomic mobility during recovery is sufficient to remove point defects and reduce the dislocation density. Diffusion allows dislocation climb, for example, which permits dislocations to move toward annihilation with other dislocations or at boundaries. High angle grain boundaries do not migrate, but low-angle subgrain boundaries may form or disappear within the interiors of grains.

2.2.2 RECRYSTALLIZATION

A dramatic microstructural change occurs during recrystallization. Strain-free grains initiate from nearly strain-free crystallites (i.e. nuclei) in the deformed microstructure. These grains consume the deformed microstructure and grow to produce a new, strain-free microstructure. Stored deformation energy in the strained metal provides the driving force for growth of the new microstructure. Recrystallization does

not occur below a critical plastic strain because there is insufficient stored deformation energy to drive it. The critical plastic strain for recrystallization ranges from 1 to 10% for most metals and is temperature dependent [2, p. 229]. Furthermore, recrystallization does not occur below a minimum temperature because atomic mobility is not sufficient for grain boundary migration. The recrystallization temperature is generally 0.3 to 0.5 T_M.

Recrystallization of a cold-deformed microstructure occurs most commonly as a discontinuous nucleation-and-growth process. Recrystallization of a cold-deformed microstructure during annealing at elevated temperature is sometimes called primary recrystallization, which distinguishes it from secondary recrystallization (i.e. static abnormal grain growth). Nuclei for new grains are thought to be crystallites (small regions of nearly strain-free crystal) which possess a size advantage and large misorientation with respect to the surrounding microstructure.

2.2.3 GRAIN GROWTH

After recrystallization, the microstructure is relatively stable compared to the previous deformed state. However, a large number of grain boundaries may remain. As with all defect structures, grain boundaries are thermodynamically unstable. This provides a boundary curvature driving force for boundary elimination by grain growth. Grain growth thus reduces the overall fraction of grain boundaries in the metal. Grains typically grow until they become pinned, such as by impurity particles that impede their boundary motion.

2.2.4 ABNORMAL GRAIN GROWTH

Abnormal grain growth refers to the selective growth of a few large grains in a matrix of much smaller grains. These large grains are termed *abnormal*, and they consume the finer grain microstructure that surrounds them. Abnormal grain growth is

typically thought to occur when normal grain growth is inhibited. The inhibition of normal grain growth results from a number of material conditions [5], which include:

(1) presence of pinning particles [1, p.293-304, 14];

(2) a strong crystallographic texture [19];

(3) a grain size on the order of sheet or film thickness;

(4) a decrease in grain boundary mobility from solute drag.

In these instances, the average grain boundary migration rate is reduced. However, a few anomalous grains, which possess a larger size or greater degree of misorientation with respect to their surrounding neighbors, may exist in the microstructure. These anomalous characteristics contribute to a high interfacial energy, which results in a relatively high boundary mobility and/or driving force for these grains. Abnormal growth occurs when a small number of grains retain such mobile boundaries.

2.3 Hot Deformation

Hot-working or creep describes deformation at elevated temperature. Creep describes time-dependent deformation which occurs at slow strain-rates ($\dot{\varepsilon} = 10^{-8}$-$10^{-1}$ s^{-1}), as compared to the fast strain-rates of hot working ($\dot{\varepsilon} = 10^{-1}$-$10^{2}$ s^{-1}). Dynamic restoration processes which have been observed during hot-working and creep are described as follows.

2.3.1 CREEP

Creep is time-dependent deformation which occurs at elevated temperature. Elevated temperature affects the dynamic microstructure in two ways: (1) deformation mechanisms which require thermally-activated processes may be active and (2) dynamic recovery takes place such that dislocations annihilate and move into lower energy configurations.

A standard strain-time creep curve for a constant-stress test of a typical pure metal, or Class II (Class M) alloy, is schematically represented in Figure 2-1. This figure demonstrates the three different stages of creep: transient creep (Stage I), steady-state creep (Stage II), and tertiary creep (Stage III). During transient creep, strain rate decreases, which corresponds to the development of deformation substructure. Dislocation density increases and subgrains form within the interior of grains. Steady-state creep occurs when the strain rate becomes constant. During steady state creep, hardening and softening mechanisms balance such that a dynamic equilibrium is achieved in the microstructure. Finally, during tertiary creep, strain rate increases until rupture. The increase in strain rate can be attributed to the formation of microstructural damage, such as separation at grain boundaries and ductile void formation, prior to fracture [20, p.296]. A constant-(true)-strain-rate test may also be used to investigate creep through a testing frame with displacement control, as schematically represented in the stress-time curve of Figure 2-2. In this experiment, steady-state creep is reached once a constant flow stress is obtained. Tertiary creep is not shown in this figure.

Steady-state creep behavior can be described by the following phenomenological equation for a large number of metals and alloys [21]:

$$Z = \dot{\varepsilon}_{ss} exp\left(\frac{Q}{RT}\right) = A\left(\frac{\sigma}{E}\right)^{n} \tag{2-1}$$

where Z is the Zener-Holloman parameter, $\dot{\varepsilon}_{ss}$ is the steady-state creep rate, Q is the activation energy of the creep mechanism, R is the universal gas constant, T is the absolute temperature, A is a material constant, σ is the flow stress, E is the dynamic unrelaxed Young's modulus, and n is the stress exponent. Specific creep mechanisms may sometimes be identified by characteristic Q and n values. For instance, five-power creep is controlled by a dislocation-climb mechanism in pure metals and certain alloys. In this case, Q is the activation enthalpy (commonly known as activation energy) of self-diffusion and n is 5.

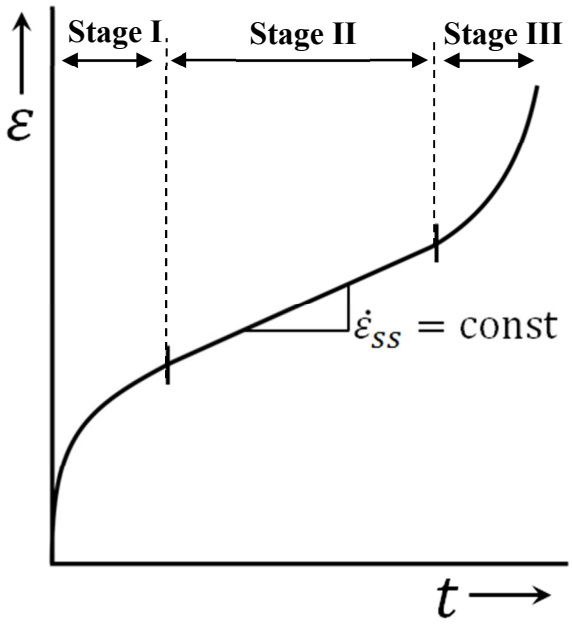

Figure 2-1: A schematic true-strain vs. time curve for a constant-stress creep experiment which represents the three stages of creep at a constant temperature.

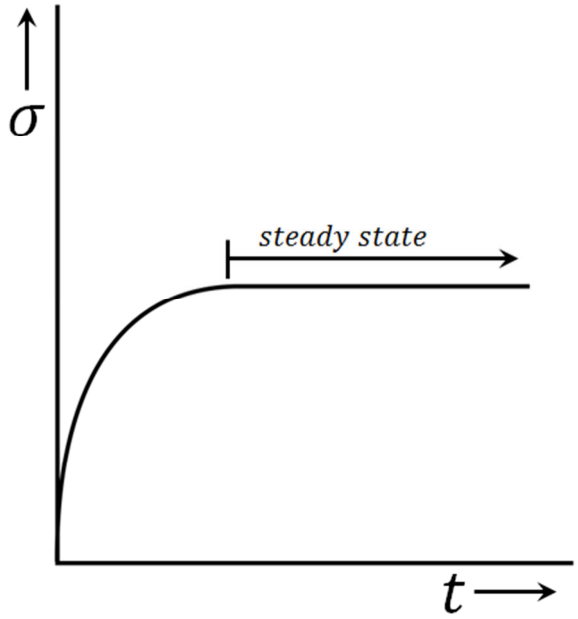

Figure 2-2: A schematic true-stress vs. time curve for a constant strain-rate creep experiment at a constant temperature. The tertiary stage of creep is not shown.

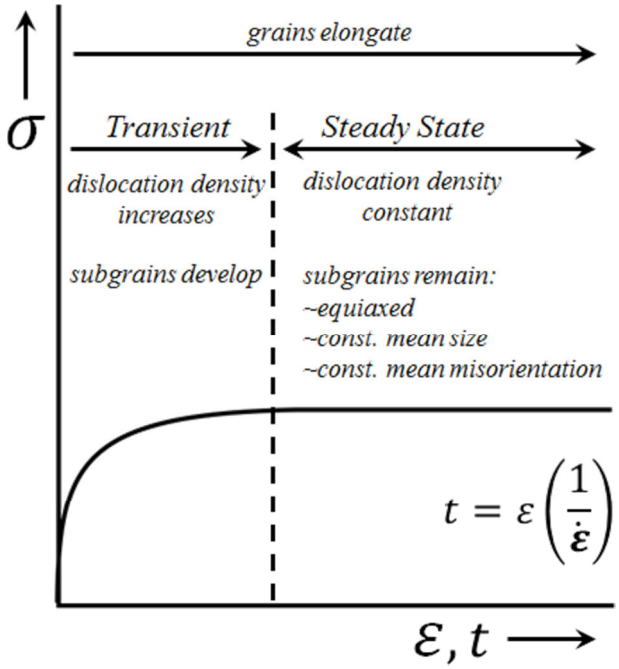

Figure 2-3: A schematic true-stress vs. true-strain curve for a constant strain-rate creep experiment at a constant temperature, which describes substructure development. Figure after *Humphreys and Hatherly* [1, p.418].

2.3.2 DYNAMIC RECOVERY

Dynamic recovery (DRV) is the elimination of dislocations during plastic deformation. When a steady-state is achieved during DRV, which can occur during steady-state creep, new high-angle boundaries do not develop and existing high-angle grain boundaries do not substantially migrate. During DRV, dislocations are annihilated and rearranged in the grain interiors. DRV is why the hot-working flow stress is lower than the cold-working flow stress.

During initial creep deformation of most metals and alloys, the dislocation density increases and subgrains develop through dislocation climb, cross-slip, and glide. As the dislocation density increases, the driving force for recovery increases. Steady-state creep occurs when a dynamic equilibrium between these hardening and recovery processes is obtained, whereby the formation rate and elimination rate of deformation substructure is approximately equal. Although the substructure is transient, microstructural parameters such as the average dislocation density, average subgrain size, and average subgrain misorientation remain nearly constant. These parameters are largely independent of strain during steady-state creep. For instance, there is an inverse relationship between steady-state flow stress and subgrain size [22]:

$$\sigma_{ss} \propto \left(\frac{1}{\lambda}\right) \tag{2-2}$$

where σ_{SS} is steady-state flow stress and λ is subgrain size. On the other hand, a microstructural feature that continues to evolve is the grain shape, which elongates with increasing strain. Figure 2-3 illustrates these concepts schematically in a stress-strain curve for a constant-(true)-strain-rate test.

Dynamic recovery is faster in materials with high stacking fault energies, high-γ_{SFE}. In low-γ_{SFE} metals, dislocations dissociate into partials, making dislocation climb

and cross-slip difficult. This is evidenced in slow steady-state creep rates for low-γ_{SFE} metals [23, 24]. Molybdenum and other body-centered-cubic metals have high stacking fault energies. Therefore, these metals, generally, deform exclusively through slip (i.e. no twinning) and exhibit rapid dynamic recovery.

2.3.3 DYNAMIC RECRYSTALLIZATION

Dynamic recrystallization (DRX) refers to the creation of a new grain microstructure during hot deformation. As mentioned previously, several different types of dynamic recrystallization have been observed. These include both discontinuous dynamic recrystallization (DDRX) and continuous dynamic recrystallization (CDRX) processes.

DDRX occurs in low-γ_{SFE} and medium-γ_{SFE} metals, in which dynamic recovery is slow. After a critical strain, recrystallized grains nucleate at the old grain boundaries. As the dislocation density of these new grains increases, the driving force for their growth by boundary migration decreases. Therefore, the recrystallized grains exhibit limited growth. Stress-strain curves representative of DDRX for different Zener-Hollman, *Z*, parameters are shown schematically in Figure 2-4. These curves illustrate important features of DDRX: (1) the critical strain for DDRX decreases with decreasing *Z*, (2) the flow stress peaks are characteristic of DDRX; whereas flow stress increases monotonically during DRV as in Figure 2-3, (3) multiple flow stress peaks may occur at low *Z*, and (4) a steady-state flow stress is eventually obtained. Furthermore, the flow stress and recrystallized grain size are largely independent of initial grain size.

Several mechanisms have been proposed for CDRX processes. Of these, geometric dynamic recrystallization (GDRX) has been verified experimentally in Al-Mg alloys [1, p.461-465]. During GDRX, grains develop serrations on their high angle

boundaries which correspond to the underlying subgrain size. Grains thin as they elongate during straining. At large strains, the thickness of grains approaches the size of boundary serrations. Thus, subgrains may "pinch-off" and form a new grain with high angle boundaries. Another experimentally-verified mechanism for CDRX is termed rotation recrystallization [25]. This mechanism involves subgrain rotation during straining. Subgrains may rotate to such a degree that they form high angle boundaries and become new grains. This phenomenon occurs in subgrains which are adjacent to existing high angle boundaries, along which recrystallized grains commonly form in "necklaces".

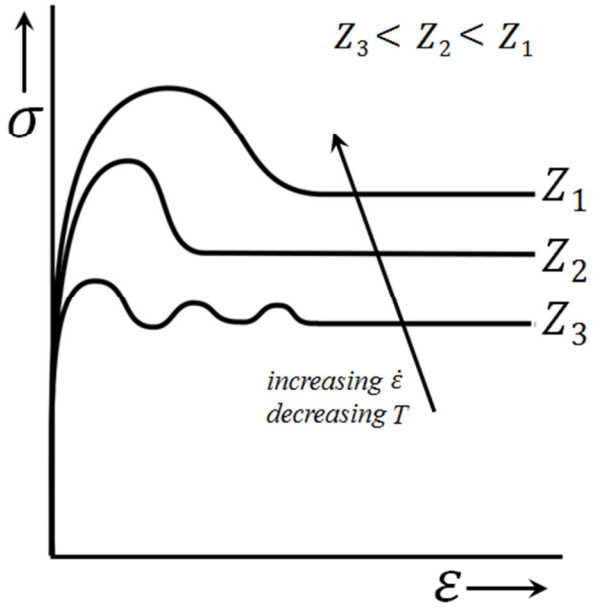

Figure 2-4: A schematic true-stress vs. true-strain curve during dynamic recrystallization. The three curves represent tests at different Zener Hollerman, *Z*, parameters. Figure after *Humphreys and Hatherly* [1, p.428].

2.3.4 DYNAMIC GRAIN GROWTH

Limited research has been conducted into dynamic (normal) grain growth. There has been some effort to study grain growth during hot deformation involving

superplasticity in Al alloys, where grain size affects the grain-boundary-sliding (GBS) creep mechanism [26-29]. Coarsening has not been generally reported during creep when grains elongate due to straining, but coarsening is often observed for GBS creep, which normally retains an equiaxed grain structure. During DDRX, dynamic grain growth generally does not occur, and grain size is observed to be nearly constant once a steady-state flow stress is reached.

3 BACKGROUND ON DAGG

This chapter introduces theory relevant to the discussion of potential mechanisms for DAGG (Sections 3.1, 3.2), provides an overview of molybdenum (Section 3.3) and then reviews the DAGG phenomenon (Section 3.4).

3.1 Grain Boundary Migration

Grain boundaries migrate under the influence of one or more driving forces, P, which reduce the Gibbs free energy of the microstructure. These driving forces have units of pressure and depend upon the free energy as follows:

$$P = \frac{\Delta G}{V_M}, \tag{3-1}$$

where V_M is the molar volume and ΔG is the difference between the Gibbs free energy of the final and initial states, $\Delta G = G_{final} - G_{initial}$. Susceptibility of a boundary to this migration is quantified by grain boundary mobility, M, whereby a boundary of high mobility migrates more rapidly than a boundary of low mobility. The rate of boundary migration, v, is the product of mobility and driving force:

$$v = MP\ . \tag{3-2}$$

Table 3-1 reproduces a list of driving forces and their relative magnitudes, as presented by Gottstein [30, p.130]. Note that this list is not specific to molybdenum and includes estimated values for different driving forces. Stored deformation energy, grain boundary curvature, and the chemical driving force are greater by at least two orders in magnitude than the other driving forces. The chemical driving force only pertains to solid solutions. Therefore, stored deformation energy and/or grain boundary curvature are considered to be the most likely driving force(s) for DAGG in molybdenum.

Source	Equation	Approximate value of parameters	Estimated driving force in MPa
Stored deformation energy	$P = \frac{1}{2}\rho\mu b^2$	ρ=dislocation density ~10^{15}/m^2 $\frac{\mu b^2}{2}$=dislocation energy ~10^{-8} J/m^2	10
Grain boundary curvature	$P = \frac{2\Delta\sigma_b}{R}$	σ_b=grain boundary energy ~0.5 J/m^2 R=grain boundary radius of curvature ~10^{-4} m	10^{-2}
Surface energy	$P = \frac{2\Delta\sigma_s}{d}$	d=sample thickness ~10^{-3} m σ_s=surface energy difference of two neighboring grains ~0.1 J/m^2	$2\cdot10^{-4}$
Chemical driving force	$P = R(T_1 - T_0)c_0 lnc_0$	c_0=concentration=max. solubility at T_0 T_1(<T_0) annealing temperature (5% Ag in Cu at 300°C)	$6\cdot10^{2}$
Magnetic field	$P = \frac{\mu_0 H^2 \Delta\chi}{2}(cos^2\theta_1 - cos^2\theta_2)$	Material: bismuth H=magnetic field strength (10^7 A/m) $\Delta\chi$=difference of magnetic susceptibilities ~1.8·10-^{7}(250°C) Θ angle between c-axis and field direction (Θ_1=0°; Θ_2=90°)	$3.5\cdot10^{-4}$
Elastic energy	$P = \frac{\tau^2}{2}\left(\frac{1}{E_1} - \frac{1}{E_2}\right)$	τ=elastic stress ~10MPa E_1,E_2=elastic moduli of neighboring grains~10^5 MPa	$2.5\cdot10^{-4}$
Temperature gradient	$P = \frac{\Delta S \cdot 2\lambda\Delta T}{V_m}$	ΔS=entropy difference between grain boundary and crystal (approx.. equivalent to melting entropy) ~$8\cdot10^3$ J/K·mol ΔT=temperature gradient ~10^4 K/m 2λ=grain boundary thickness ~$5\cdot10^{-10}$m V_m=Molar volume ~10cm^3/mol	$4.5\cdot10^{-5}$

Table 3-1: Driving Forces and estimated magnitudes. Reproduced from Gottstein [30].

Growth Mechanism	Molybdenum Parameters	Driving Pressure Equation	Driving Pressure, P (MPa)	Free Energy, ΔG (J/mol)
Boundary Curvature	d=20x10^{-6}m γ=2 J/m^2	$P \sim 3\gamma/d$	0.3	2.8
Stored Dislocations	$\rho_\perp$=10^{13}-10^{15}m^{-2} μ=125.6 GPa |b|=0.27 nm	$P \sim 0.5\rho_\perp\mu\|b\|^2$	0.05 - 5	0.4 – 4

Table 3-2: Estimated magnitudes for boundary curvature and stored dislocations driving forces with molybdenum parameters [31, p. 8-2, 15-3, 32]. V_m = 9.41 m^3/mol

Accordingly, Table 3-2 lists estimates for the magnitude of stored deformation energy and boundary curvature specifically for molybdenum, based on properties reported in the literature [31, p. 8-2, 15-3, 32]. Depending on the dislocation density, the driving pressure from stored deformation energy may be larger or smaller than boundary curvature.

Mobility generally exhibits an Arrhenius dependence on temperature. A simple model of grain-boundary migration [33, p.133-136], which does not assume a specific boundary structure, yields the following relationships:

$$M = A\frac{{V_M}^2}{T} exp\left(-\frac{\Delta G^A}{RT}\right) , \tag{3-3}$$

where A is a variable which depends upon the material and grain boundary structure, T is the temperature in K, R is the universal gas constant, and ΔG^A is the activation energy an atom needs to jump across the grain boundary.

3.2 Slip and Strain in Crystals

Initiation and growth of abnormal grains for DAGG occurs only during plastic straining at elevated temperature. Thus, plasticity is critical to the DAGG process. Plastic deformation of the large DAGG grains themselves is likely to play an important role in the DAGG process. Therefore, the theory of plastic deformation in single crystals through slip is now introduced and will be referred to in later chapters.

3.2.1 SLIP IN SINGLE CRYSTALS AND POLYCRYSTALS

Slip is dislocation motion through a crystal, and it is the primary mechanism for plastic deformation in metals. Slip is necessarily crystallographic; dislocations move in slip directions and within slip planes. A slip direction $[uvw]$ and a slip plane (hkl) constitute a slip system $(hkl)[uvw]$.

Consider a single crystal under an applied uniaxial stress σ that results from loading along a crystallographic direction $[abc]$. The Schmid factor, m, of a particular slip system $(hkl)[uvw]$ is the product of the cosines of two different angles, φ and λ:

$$m = cos(\varphi)cos(\lambda)\ , \tag{3-4}$$

where φ is the angle between $[abc]$ and $[hkl]$ and λ is the angle between $[abc]$ and $[uvw]$. Therefore, the m on a slip system depends only upon the tensile loading direction. The Schmid factor relates (1) the resolved shear stress, τ_{RSS}, on a slip system to the applied stress, σ, and (2) the axial strain, ϵ, along the loading direction to the shear strain, γ, on the slip system:

$$m = \frac{\tau_{RSS}}{\sigma} = \frac{\epsilon}{\gamma}\ . \tag{3-5}$$

The slip system with the maximum Schmid factor has the greatest τ_{RSS}. Plastic flow initiates on a slip system when the τ_{RSS} exceeds a critical value, τ_{CRSS}, for that slip system. The critical resolved shear stress, τ_{CRSS}, of a slip system depends upon deformation conditions, such as strain rate and temperature [20, p.141-142].

In bcc metals, such as molybdenum, slip almost always occurs along the $\langle 111 \rangle$ close-packed directions and preferentially within the $\{110\}$ planes, which are the closest-packed planes of the bcc structure. Slip may also occur in less closely packed planes, such as $\{112\}$ and $\{123\}$, given in order of decreasing preference and decreasing packing density. In molybdenum, slip has been generally reported on the $\{110\}$ and $\{112\}$ planes, with the former preferred at elevated temperature and the latter preferred at low temperature [31, p. 4-39]. The critical resolved shear stress, τ_{CRSS}, is different for each family of slip planes [20, p.142]. There are twelve physically distinct slip systems in $\{110\}\langle 1\bar{1}1 \rangle$, twelve in $\{112\}\langle 11\bar{1} \rangle$, and twenty-four in $\{123\}\langle 11\bar{1} \rangle$.

3.2.2 THREE-DIMENSIONAL STRAIN AND INDEPENDENT SLIP SYSTEMS

A strain state is completely defined by five independent strain components, if volume is conserved [34, p.308]. Strain ε_{ij} is the symmetrical part of the variation in displacement u_i with position x_i. The following equation defines nine tensor components for a three dimensional body:

$$\varepsilon_{ij} = \frac{1}{2}\left(\frac{\partial u_i}{\partial x_j} + \frac{\partial u_j}{\partial x_i}\right). \tag{3-6}$$

Conversely, rotation ω_{ij} is the antisymmetrical part of the variation in displacement with position:

$$\omega_{ij} = \frac{1}{2}\left(\frac{\partial u_i}{\partial x_j} - \frac{\partial u_j}{\partial x_i}\right). \tag{3-7}$$

A strain state necessarily has six independent components because the strain tensor is symmetric ($\varepsilon_{ij} = \varepsilon_{ji}$). If volume is conserved (i.e. density does not change), as is typical for the plastic deformation of metals, then the dilation is zero ($\varepsilon_{11} + \varepsilon_{22} + \varepsilon_{33} = 0$) and the strain state is completely defined by five independent strain components:

$$\varepsilon_{ij} = \begin{bmatrix} \varepsilon_{11} & \varepsilon_{12} & \varepsilon_{13} \\ \varepsilon_{12} & \varepsilon_{22} & \varepsilon_{23} \\ \varepsilon_{13} & \varepsilon_{23} & -\varepsilon_{11}-\varepsilon_{22} \end{bmatrix}. \tag{3-8}$$

Therefore, five independent slip systems are necessary to produce an arbitrary strain state. It was shown by Von Mises [35] that, in the continuum approximation, only five independent slip systems can exist and that this is the number generally necessary for ductility in polycrystalline materials.

The strain $\gamma^{(s)}$ on physically distinct slip system s with slip direction $[uvw]$ and slip plane (hkl) makes the following contribution ${\varepsilon_{ij}}^{(s)}$ to the strain tensor [36, p. 191]:

$${\varepsilon_{ij}}^{(s)} = \frac{\gamma^{(s)}}{2}\left(b_i n_j + b_j n_i\right), \tag{3-9}$$

where b_i is the unit slip direction and n_j is the unit normal of the slip plane such that:

$$\varepsilon_{ij}{}^{(s)} = \gamma^{(s)} \begin{bmatrix} uh & (vh+uk)/2 & (ul+wh)/2 \\ (vh+uk)/2 & vk & (wk+vl)/2 \\ (ul+wh)/2 & (wk+vl)/2 & wl \end{bmatrix}. \quad (3\text{-}10)$$

The total strain tensor ε_{ij} is a summation of the contributions from N active slip systems:

$$\varepsilon_{ij} = \sum_{s=1}^{N} \varepsilon_{ij}{}^{(s)} \ . \quad (3\text{-}11)$$

A slip system is independent if it produces a vector of strain components $e^{(s)} = \left[\varepsilon_{11}{}^{(s)},\ \varepsilon_{22}{}^{(s)},\ \varepsilon_{23}{}^{(s)},\ \varepsilon_{13}{}^{(s)},\ \varepsilon_{12}{}^{(s)}\right]$ that is linearly independent from those of other slip systems. That is, no constants $C_1, C_2, \cdots, C_n$ exist such that,

$$C_1 e^{(1)} + C_2 e^{(2)} + \cdots + C_n e^{(n)} = 0\ , \quad (3\text{-}12)$$

except for $C_1 = C_2 = \cdots = C_n = 0$. Note that vector $e^{(s)}$ contains the five independent strain components (see Equation 3-8), where

$$\varepsilon_{11}{}^{(s)} = uh,$$
$$\varepsilon_{22}{}^{(s)} = vk,$$
$$\varepsilon_{23}{}^{(s)} = (wk+vl)/2,$$
$$\varepsilon_{13}{}^{(s)} = (ul+wh)/2, \text{ and}$$
$$\varepsilon_{12}{}^{(s)} = (vh+uk)/2,$$

for slip system s.

3.3 Overview of Molybdenum

Molybdenum is a body-centered cubic refractory metal ($Z = 42$). Refractory metals are primarily used for their strength and creep resistance at high temperatures. Such applications include electrical filaments, electrical contacts, heat shielding,

aerospace components [7], and nuclear reactors [37]. The advantages of molybdenum over other refractory metals include availability, specific strength at high temperature, and low-temperature oxidation resistance [7]. Other desirable properties include a superior corrosion resistance, a low thermal expansion coefficient, and good thermal conductivity. The two oxides MoO_2 and MoO_3 readily form at high temperatures [38]. The oxide MoO_2 decomposes to Mo and MoO_3 [39]. The oxide MoO_3 has a lower melting temperature (795°C) than that of the metal (2610°C). Therefore, molybdenum components are usually limited to high-temperature service in inert or vacuum environments. Furthermore, oxidation contributes to recrystallization embrittlement, as previously discussed in Section 1.1.

3.4 Abnormal Grain Growth in Molybdenum

Dynamic abnormal grain growth is a phenomenon which has, thus far, only been observed in molybdenum. DAGG is abnormal growth which only occurs during concurrent plastic straining. Although SAGG has been observed in sintered molybdenum at 2000ºC, SAGG does not occur at the shorter annealing times and lower temperatures associated with DAGG. This section reports on previous studies of SAGG in molybdenum and reviews existing knowledge of DAGG.

3.4.1 Static Abnormal Grain Growth in Molybdenum and Tungsten

Static abnormal grain growth (SAGG) has been utilized to create single crystals in molybdenum sheet [40-42]. In those studies, small amounts of CaO and MgO were added to molybdenum powder prior to sintering. The presence of the associated second-phase particles inhibits normal grain growth and promotes AGG [1, p.293-304, 14]. After sintering, these doped Mo materials were rolled at 1000ºC and annealed for 1 hour at

temperatures above 2000 ºC to produce SAGG, which occurred in the final annealing step.

SAGG has also been observed following high-temperature annealing of tungsten, another body-centered-cubic refractory metal. Examples from tungsten materials include drawn sintered wire [11-13] and rolled sintered ingots [43, 44]. The microstructures of these tungsten products were doped with potassium, which is mixed with the metal powder prior to sintering. The potassium volatizes into gas bubbles either during sintering or subsequent annealing. These bubbles act as second-phase particles, promoting SAGG [1, p.293-304]. Abnormal growth was observed in tungsten materials only at temperatures above 1400ºC.

3.4.2 DYNAMIC ABNORMAL GRAIN GROWTH IN MOLYBDENUM

Dynamic abnormal grain growth is AGG that requires plastic straining for initiation and propagation. DAGG has been observed during creep tests of molybdenum sheet at strain-rates of 10^{-6} s^{-1} to 10^{-4} s^{-1} and temperatures above 1540ºC [3-5]. DAGG was observed in two commercial purity (~99.95%) material grades: arc-melted (AM) and power-metallurgy (PM). Fundamental aspects of the DAGG phenomenon are best demonstrated through a representative example of a creep test which produces DAGG.

Figure 3-1 depicts the stress-strain behavior for such a constant true strain-rate test at 10^{-4} s^{-1} and 1540ºC. Flow stress increases and approaches a steady-state value as the material is loaded. However, an abrupt drop in the flow stress occurs at a strain of 0.18. This corresponds to the initiation and propagation of an abnormal grain(s) throughout the specimen gage length. Specimens shown in Figure 3-1 are from different tests, and the arrows in the stress-strain curve show the approximate strains at which testing was halted for each specimen shown. Therefore, the drop in flow stress is a

reflection of the higher strength of a polycrystalline microstructure than that of the single crystal(s) produced by DAGG. This microstructural change has been confirmed in macroetched specimens, which were produced at four different strains during the characteristic stress drop. The abnormal grains do not grow into the specimen grips, an indication that plastic strain is necessary for propagation. After the flow stress drop is complete, the entire gage length is consumed by one or more single crystals, and single crystal deformation continues until failure.

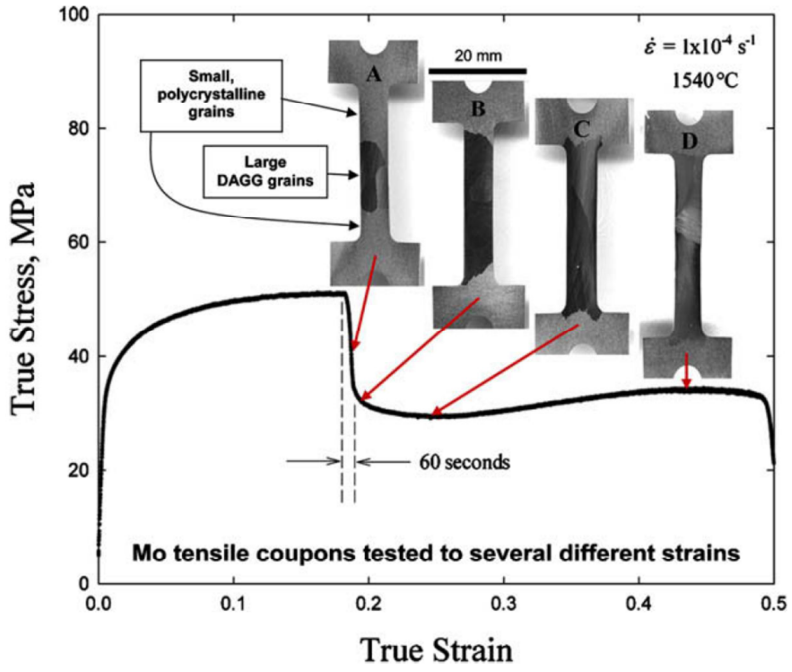

Figure 3-1: A true-stress vs. true-strain plot of a constant strain-rate creep test exhibiting dynamic abnormal grain growth. Four specimens halted at different strains are shownwith respect to the approximate strains indicated along the representative stress-strain curve. Figure reproduced from [5].

Important results from previous work on DAGG are summarized as follows:

(1) DAGG can be used to create single crystals of great size in molybdenum, as shown in Figure 1-2. The largest molybdenum single crystal produced in our laboratory

thus far is 10 cm in length, as shown in Figure 1-3. This limiting size is a direct result of size limitations for the equipment used and is not an intrinsic limitation of the DAGG process.

(2) DAGG requires a critical strain and a minimum temperature for initiation.

(3) The critical strain for DAGG decreases rapidly with increasing temperature but is insensitive to strain-rate within the range 10^{-6} s^{-1} to 10^{-4} s^{-1}. The critical strain for DAGG is lower in the AM-grade than in the PM-grade Mo material for the same temperature.

(4) DAGG completely consumes a fine, stable microstructure, such as that of the PM-grade material. However, DAGG cannot consume some of the larger grains of a coarse microstructure, such as that of the AM-grade material. Several island grains are retained within the abnormal grains in the AM-grade material. Static normal grain growth occurred in the AM-grade material during pre-heating, while the PM-grade had a stable grain size of ~18 μm.

(5) The AM-grade and PM-grade sheets exhibited different primary recrystallization textures, but both exhibit DAGG. This indicates that DAGG has no dependence, or only a weak dependence, on primary recrystallization texture.

(6) A larger number of abnormal grains nucleated in the gage length of the AM specimens than in the gage length of the PM specimens.

4 EXPERIMENTAL METHODS

Experimental methods in this study were adapted from methods in a previous study by J. Ciulik [1]. Creep specimens from both studies were stretched in uniaxial tension on the same test frame. Specimens were deformed through computer-controlled crosshead displacement. Subsequent characterization included optical microscopy (OM), electron backscatter diffraction (EBSD) and Laue X-ray back diffraction.

4.1 Materials

A commercial-purity molybdenum sheet, PM-B, of the dimensions 0.076 x 30.5 x 61.0 cm (0.030 x 12 x 24 in) was purchased from H.C. Starck, Inc. (Euclid, OH). The sheet was rolled to the as-received thickness from a bar, which itself was pressed and sintered from molybdenum powder. Prior to consolidation, the manufacturer's specification limits on powder composition are listed in Table 4-1.

Mo	Mg	Mn	Ni	Al	Cu	Pb
99.95% (min limit)	0.001%	0.001%	0.002%	0.002%	0.002%	0.002%
Ti	Ca	Si	Sn	Cr	C	Fe
0.002%	0.003%	0.003%	0.003%	0.005%	0.005%	0.005%

Table 4-1: Maximum limits for chemical compositions by weight percent.

The powder metallurgy sheet studied in this investigation is different from the powder metallurgy sheet studied in Ciulik's work [3]. Results from the present investigation will be compared to Ciulik's work in succeeding chapters. Furthermore, some original characterization of Ciulik's materials is included in this study, namely

indexing the crystallographic orientation of abnormal grains from Ciulik's specimens. Therefore, it will be necessary to discuss the two sheet materials Ciulik studied, hereafter referred to as AM (Arc-Melted) and PM-A (Powder Metallurgy A). The sheet material tested in the present investigation is referred to as PM-B (Powder Metallurgy B).

Figure 4-1 is a drawing of the "dog-bone" geometry used for all tensile specimens discussed in this dissertation. Specimens had a gage length of 2.54 cm (1.00 in), a gage width of 0.64 cm (0.25 in), and a specimen thickness of 0.076 cm (0.030 in). The tolerance of all these dimensions was ±0.008 cm (±0.003 in). Figure 4-2 depicts two different orientations of tensile specimens in the sheet: T (tensile loading direction *transverse* to the rolling direction) and L (tensile loading direction *longitudinal* along the rolling direction). The three coordinate axes correspond to 1. the sheet geometry, 2. the T specimen geometry, and 3. the L specimen geometry. The sheet axes have the standard notation of rolling direction (RD), transverse direction (TD), and normal direction (ND). The T and L axes have the standard tensile specimen notation: the tensile loading direction (TLD) is along the gage length, the long transverse direction (LTD) is along the gage width, and the short transverse direction (STD) is through the thickness of the specimen. LTD is parallel to the RD in the T orientation, while the TLD is parallel to the RD in the L orientation. The AM and PM-B specimens were machined from the sheet in the T orientation, while the PM-A specimens were machined from the sheet in the L orientation.

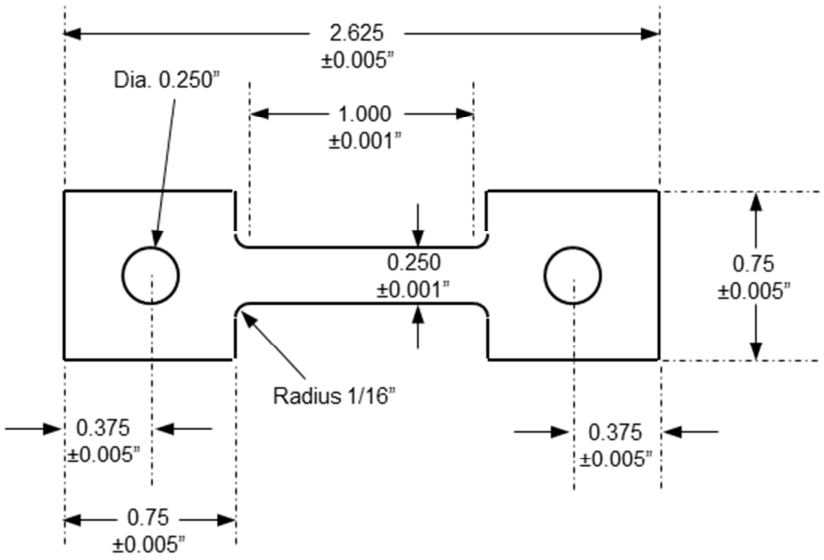

Figure 4-1: Drawing of specimens used in this study. Dimensions are in inches. Sheet thickness is as received.

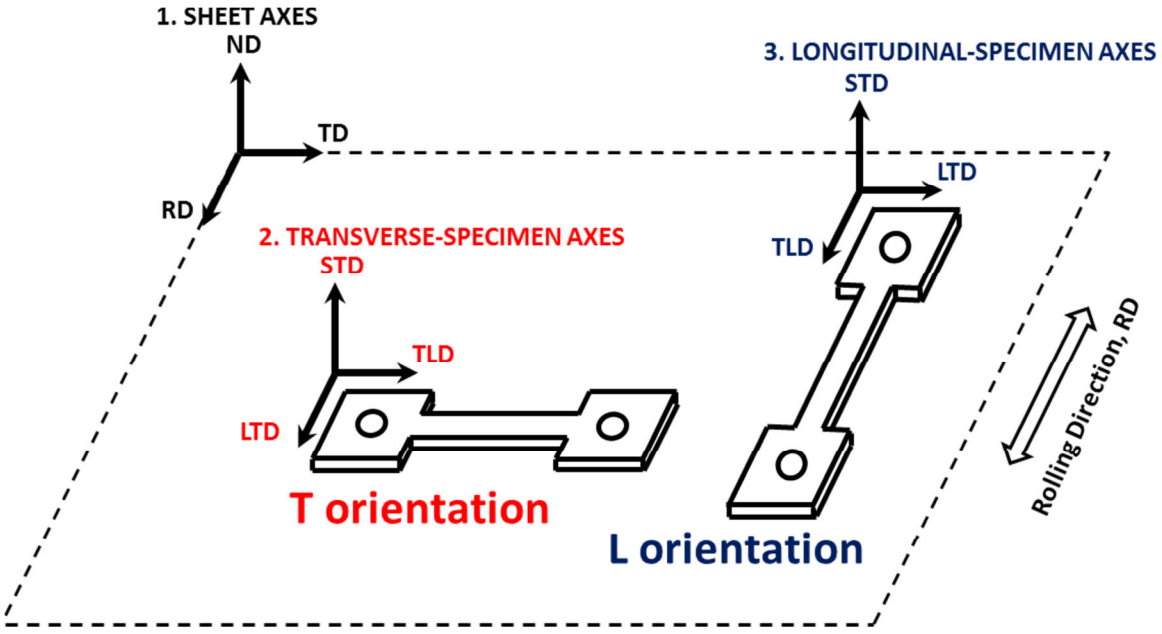

Figure 4-2 A schematic demonstrating orientation of specimen machined from the molybdenum sheet. The coordinate axes of the rolled sheet are RD (Rolling Direction), TD (Transverse Direction), and ND (sheet Normal Direction). The coordinate axes for tensile specimens are TLD (Tensile Loading Direction), STD (Short Transverse Direction), and LTD (Long Transverse Direction).

4.2 Test Frame and Furnace

Creep tests were conducted in a high-temperature vacuum furnace fitted to an electromechanical test frame. The furnace was manufactured by Thermal Technology, Inc. (Santa Rosa, CA), and the test frame was manufactured by MTS Systems (Eden Prairie, MN). The furnace is capable of temperatures up to 2000°C and operates in a vacuum range between 10^{-6} to 10^{-5} Torr. The vacuum chamber is a stainless steel box, pictured in Figure 4-3. A door on the front face provides access to the vented chamber. Vacuum is achieved with a turbo-pump backed by a mechanical pump. Water channels run through the chamber walls to provide cooling.

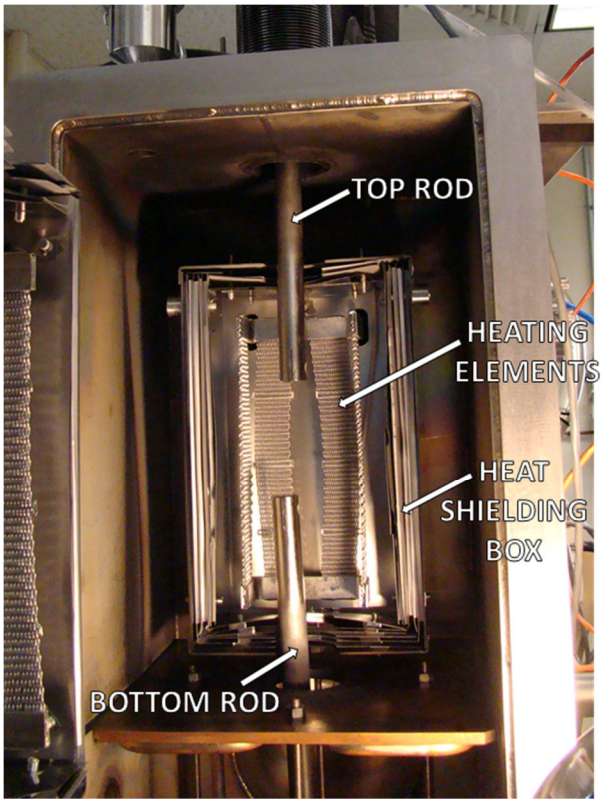

Figure 4-3: Picture of the furnace chamber identifying: (1) top and bottom tungsten pull rods, (2) heating elements, and heat shielding box.

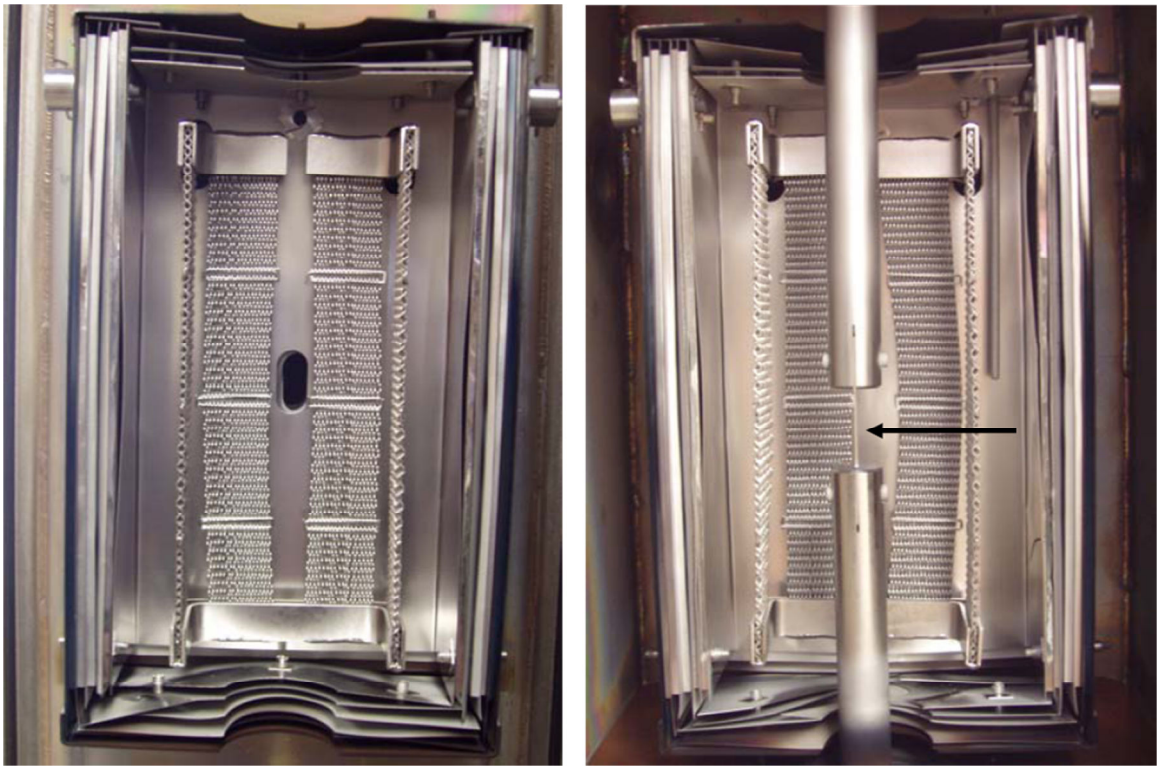

(a) **(b)**

Figure 4-4: The two halves of the heat shielding box: (a) front half attached to door and (b) back half inside the furnace. A black arrow points to an installed specimen in (b). Picture reproduced from dissertation of J. Ciulik [3].

Inside the vacuum chamber, the hot zone is contained within a heat-shielding box split into halves, as pictured in Figure 4-4. Each half contains a set of tungsten heating elements. A control thermocouple is inserted into the shielding box, where it rests behind one of the heating elements. The heat shielding surrounding the hot zone is made of five layers of molybdenum and tantalum sheet.

Tungsten pin-loaded rods grip the specimen inside the hot zone. Silicon carbide pins are loaded through the rods to hold the specimen. The bottom rod is attached to the test-frame base. The top rod is attached to the test-frame crosshead through a bellows and load-cell assembly. The bellows allows approximately three inches of travel.

4.3 Dynamic Abnormal Grain Growth Tests

Uniaxial tensile tests were performed at a constant true strain-rate of 10^{-4} s^{-1} and at temperatures from 1400°C to 1800°C. All AM and PM-A specimens discussed in this dissertation were deformed at a constant true strain-rate of 10^{-4} s^{-1} and 1540°C. Thermal profiles of the furnace hot zone were measured by moving a thermocouple along the center of the hot zone, as seen in Figure 4-5. These data were necessary to obtain the offset between the hot-zone temperature and the temperature of the control thermocouple. The thermal profiles measured are different from those recorded five years earlier by Ciulik [1]; temperature is greater by 1 to 6ºC in the newer data. This small shift in temperature is most likely because of a slightly different position of the control thermocouple, which tends to deform in service during prolonged exposure to high temperature. A constant true strain-rate was achieved through computer control of crosshead displacement. The minimum measurable crosshead displacement is 0.0005 mm (~0.00002 in), as limited by the position sensor. A program was created in MTS TestWorks®4 software to calculate and impose a new crosshead velocity every one second to maintain a nearly constant true strain-rate. New velocities were calculated from the instantaneous gage length as:

$$v = \dot{\varepsilon}(l_o + x) \,, \tag{4-1}$$

where v is the velocity, $\dot{\varepsilon}$ is the desired true strain-rate, l_o is the initial gage length, and x is the crosshead extension. This calculation requires the assumption of uniform deformation and constant volume within the specimen gage length. Measurements following testing indicate that these assumptions were quite accurate for strains up to nearly rupture.

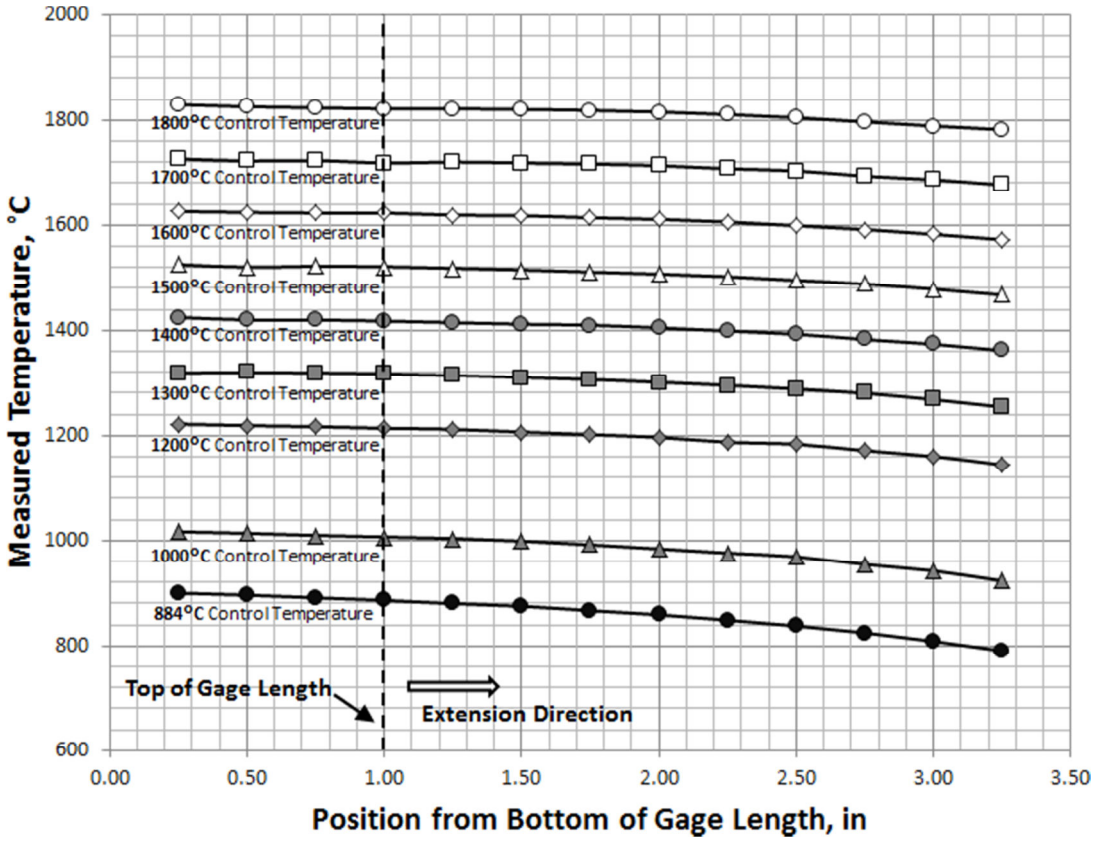

Figure 4-5: Temperature profiles, temperature as a function of vertical position within the hot zone, of the furnace hot zone at several different control temperatures.

Specimens were installed with a preload of 10 lbf (σ = 9.2 MPa). During heating to the test temperature, computer control was used to maintain this preload. Preloading ensured that the specimen and the load train were held taught during thermal expansion of the load assembly. Specimen temperature was ramped to the desired test temperature at a rate of 3600°C/hr, and each specimen was then preheated at this temperature for 135 minutes prior to the initiation of straining. The purpose of this long heating time was to develop thermal equilibrium in the hot zone, such that thermal expansion of the specimen and load train was negligible and heat flow was constant. Some slight creep occurred in

the preloaded specimen during this preheating, and this deformation is difficult to separate from the rate of thermal expansion. However, the preload stress was chosen to keep this creep strain as small as possible during preheating. After preheating, the specimen was fully recrystallized, as the test temperatures are well above the recrystallization temperature of molybdenum (approximately 900 to 1200°C) [45]. The bellows and vacuum contributions to the load are subtracted during data analysis. True stress and true strain are calculated using constant volume relationships:

$$\sigma = s(1 + e) \tag{4-2}$$

$$\varepsilon = \ln(1 + e)\ , \tag{4-3}$$

where σ is the true stress, ε is the true strain, s is the engineering stress, and e is the engineering strain.

Some tensile tests were conducted to failure, but the majority of the tests were halted earlier to characterize the early stages of DAGG. The following stop condition was programmed into the MTS software routine that controls the test: Unload the specimen when the load drops to 95% of its maximum value during the test. Automated detection of the load drop ensured that each test would be halted shortly after DAGG grain initiation. Once unloaded, the furnace was turned off to cool the specimen. Because it was not possible to quench the specimen in the vacuum furnace, some recovery of the deformation substructure may have occurred during the furnace cooling. Figure 4-6 is a cooling curve from a test at 1650ºC. The cooling rate is initially 420ºC/min and drops to 11ºC/min over 30 minutes.

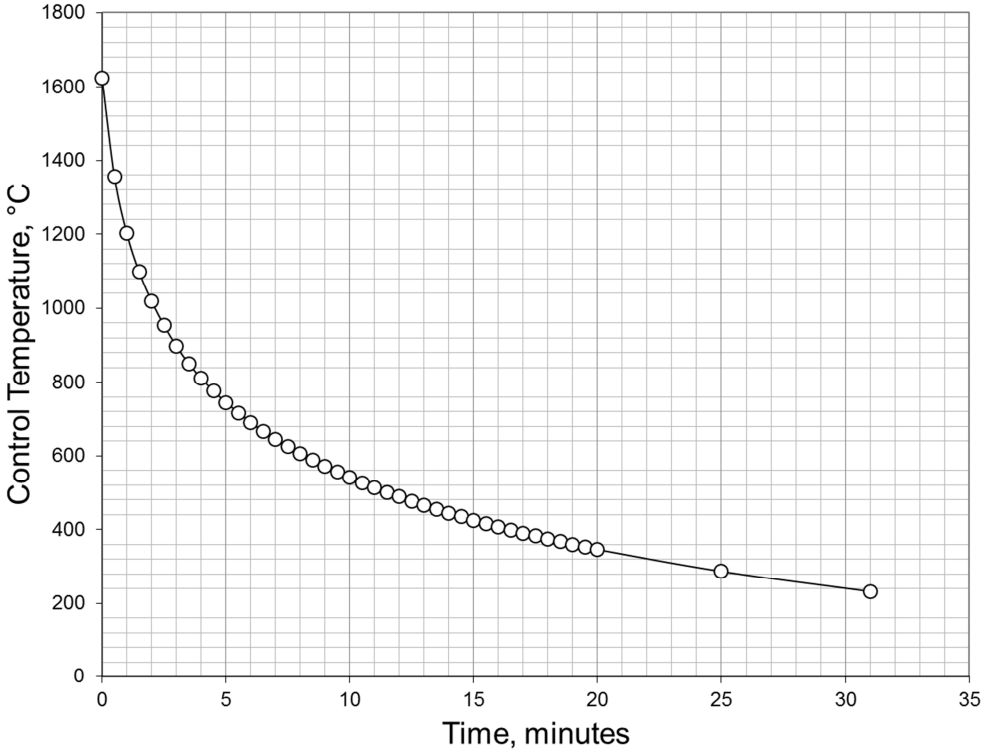

Figure 4-6: Cooling curve, temperature of the control thermocouple as a function of time after power is withdrawn, of the furnace from a temperature of 1650ºC.

4.4 Characterization

The chemical compositions of the materials were determined through X-ray Fluorescence (XRF) and Instrumental Gas Analysis (IGA). XRF relies on characteristic secondary X-rays, produced from interactions with a high-energy incident X-ray beam. Only elements heavier than Na can be detected with XRF. In IGA, the specimen is volatized in a high-temperature induction furnace. The gases produced are analyzed with an infrared sensor to detect C, O, and S, or a thermal-conductivity sensor to detect N. It should be noted that XRF probes the surface composition, and IGA probes the bulk composition. IGA was performed on the PM-B material by EAG Labs (Syracuse, NY).

Microstructures were primarily characterized with optical microscopy (OM). Metallographic preparation was identical to that suggested by Ciulik; however, one part (by volume) 30% hydrogen peroxide was added to ninety-nine parts colloidal silica to create the final polishing solution. This solution yielded better results by enhancing chemical polishing. Table 4-2 lists the amended polishing schedule. When particle embedding and pull-out occurred, Buehler Microcloth™ was used instead of Struers MD-Dur, and a higher force was applied. Grain boundaries were etched with a solution of one part nitric acid to one part sulfuric acid to one part water mixture. Cotton swabs were used to apply the etchant to the specimen, instead of Ciulik's method of submerging the specimens in the etchant. The etchant was mixed with a higher concentration than that suggested by Ciulik because a higher concentration worked better for cotton swabbing. Grain size was measured by the lineal intercept method [46].

Polishing Surface	Lubricant / Polishing Media	RPM	Force	Time
MD-Piano 220	Water	300	35N	Until Planar.
MD-Piano 600	Water	300	35N	3 min.
MD-Piano 1200	Water	300	35N	3 min.
MD-Allegro	9μm DiaoDuo	150	35N	3 min.
MD-Largo	9μm DiaoDuo	150	30N	3min
MD-Dur	3μm DiaoDuo	150	25N	3min
MD-Chem	1 part (by volume) 30% H2O2 99 parts 0.05μm colloidal silica	150	25N	3min

Table 4-2: Metallographic Preparation (using Struers consumables). Grinding and polishing was performed on an automated polisher Struers Rotopol-15™.

Electron Backscatter Diffraction (EBSD) provided primary recrystallization textures and grain size of the microstructure. In preparation for EBSD examination, a surface was electropolished with a solution of 10 parts (by volume) methanol, 6 parts ethylene glycol monobutyl ether, and 1 part perchloric acid (60%). As a note to the reader, all perchloric acid work should be performed under a perchloric-specific "wash-down" fume hood. Electropolishing steps are provided in Table 4-3. Two 1 mm × 1 mm scans were conducted on the grip region of one specimen, and two 1mmx1mm scans were conducted on the gage region of one specimen. A silicon single crystal of known orientation was mounted on the specimen holder to determine the precise rotation matrix between crystal and specimen reference frames. Orientation distribution functions (ODF) were fitted to the texture of each region with a spherical harmonic basis and 5º bins.

Grinding	Lubricant / Polishing Media	RPM	Force	Time
MD-Piano 220	Water	300	35N	Until Planar.
MD-Piano 600	Water	300	35N	3 min.
MD-Piano 1200	Water	300	35N	3 min.
Electropolishing	**Current Density**	**Voltage**	**Temperature**	**Time**
Electropolish	1.8mA/cm^2	29V	20ºC	20 sec

Table 4-3: Electropolishing (using Struers consumables). Grinding was performed on an automated polisher Struers Rotopol-15™; electropolishing was performed with a Struers LectroPol-5™.

The Laue X-ray back diffraction technique was used to determine the orientations of abnormal grains. An image of each etched specimen containing a DAGG grain was

optically scanned into a computer at a resolution of 600 dpi, and the specimen was subsequently mounted in a bidirectional positioning stage. Coordinates, *x*-*z*, of the abnormal grains, in reference to the stage, were determined from the scanned image. This method allowed reliable positioning of the X-ray beam on the abnormal grains. A photosensitive image plate was used to collect the X-ray diffraction patterns. The distance of the specimen to the film was 2.6 cm; the exposure time was 1 minute; the current was 20 mA; and the accelerating voltage was 35 kV for these experiments.

5 MATERIAL CHARACTERIZATION

The chemical composition and microstructure of the PM-B material were characterized prior to tensile testing. The recrystallization and grain growth behaviors of the sheet were also studied through a series of static anneals. The static grain growth behavior was determined to compare with DAGG behavior. The PM-B material is compared to the molybdenum sheets previously studied by Ciulik, the AM and PM-A materials [3].

5.1 Chemical Composition

The chemical composition of the as-received PM-B sheet was at least 99.9 at.% molybdenum according to XRF. However, the dispersoid particles that are most likely to pin grain boundaries, carbides, nitrides or oxides, contain light elements that XRF cannot detect. Therefore, the amounts C, N, O, and S were determined for PM-B through IGA. A comparison of the chemical compositions between the different material sheets is displayed in Table 5-1. Both PM materials have a significant concentration of oxygen, while the AM material has a significant concentration of nitrogen. All these materials contained less than 10 ppm of C, by weight.

Material	**Composition of Select Impurities:**			
	C	**O**	**N**	**S**
AM	<10	<10	33	-
PM-A	<10	34	<10	-
PM-B	<10	40	<10	<10

Table 5-1: A comparison of the impurity content for C, O, N, and S in ppm.

5.2 Static Recrystallization Texture

Texture refers to the orientation distribution of grains within a microstructure. In a sheet material, texture components are commonly described through the following notation: $\{ND\}\langle RD\rangle$, where $\{ND\}$ is the crystallographic plane perpendicular to the normal direction and $\langle RD\rangle$ is the crystallographic direction along the rolling direction. Body-centered-cubic metals form a $\langle 110\rangle$ fiber texture during tensile deformation, and they form mixed $\langle 100\rangle$ and $\langle 111\rangle$ fibers during compression deformation. [36, p. 192]. In rolling, the $\langle RD\rangle$ is an extension direction and the $\langle ND\rangle$ is a compression direction. Accordingly, bcc rolling textures have prominent α- and γ-fibers [36, p. 195]. The α-fiber texture includes orientations rotated about a $\langle 110\rangle \parallel \langle RD\rangle$ axis. The primary deformation texture components in the α-fiber are $\{001\}\langle 110\rangle$, $\{112\}\langle 1\bar{1}0\rangle$, and $\{111\}\langle 1\bar{1}0\rangle$ [1, p.74-76]. These texture components and their corresponding pole figures are pictured schematically in Figure 5-1. The γ-fiber texture includes orientations rotated about a $\langle 111\rangle \parallel \langle ND\rangle$ axis. The primary deformation texture components in the γ-fiber are $\{111\}\langle 1\bar{1}0\rangle$ to $\{111\}\langle 112\rangle$ [1, p.74-76]. Rolled molybdenum has been observed to possess a $\{001\}\langle 110\rangle$ rotated cube texture, a component of the α-fiber [47, p.560].

The primary recrystallization textures of molybdenum sheet typically retain the primary components of the deformation texture; however, these texture components may sharpen or fade. The recrystallization texture of PM-B was measured in two 1×1 mm EBSD scans on material statically annealed for 130 min at 1650 ºC. Crystal direction maps of these scans are shown in Figure 5-2.

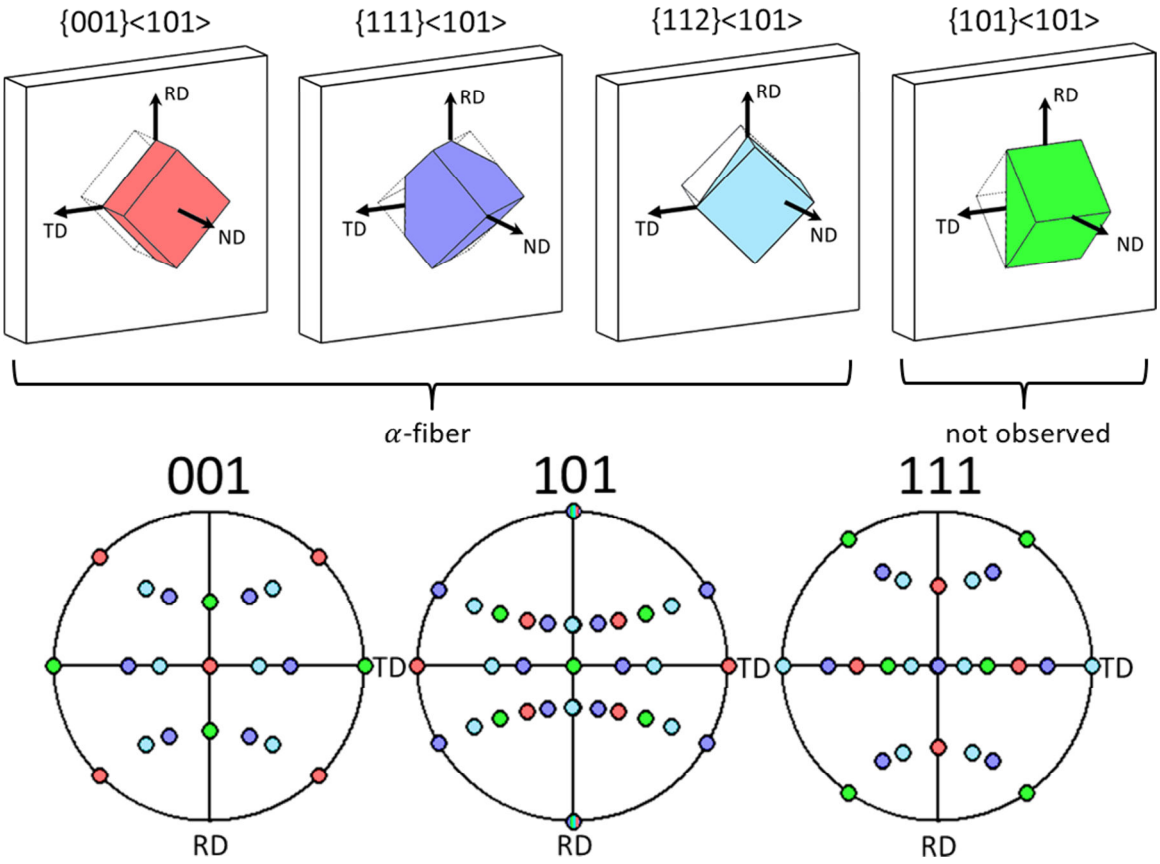

Figure 5-1: Schematic drawings and 001, 101, and 111 pole figures for three texture components {**001**}⟨**101**⟩, {**112**}⟨**101**⟩, and {**111**}⟨**101**⟩ from an α-fiber texture. A {**101**}⟨**101**⟩ texture component is not generally observed in an α-fiber texture, but it is plotted for reference. RD, TD, and ND are the rolling sheet coordinate axes as defined in Figure 4-2.

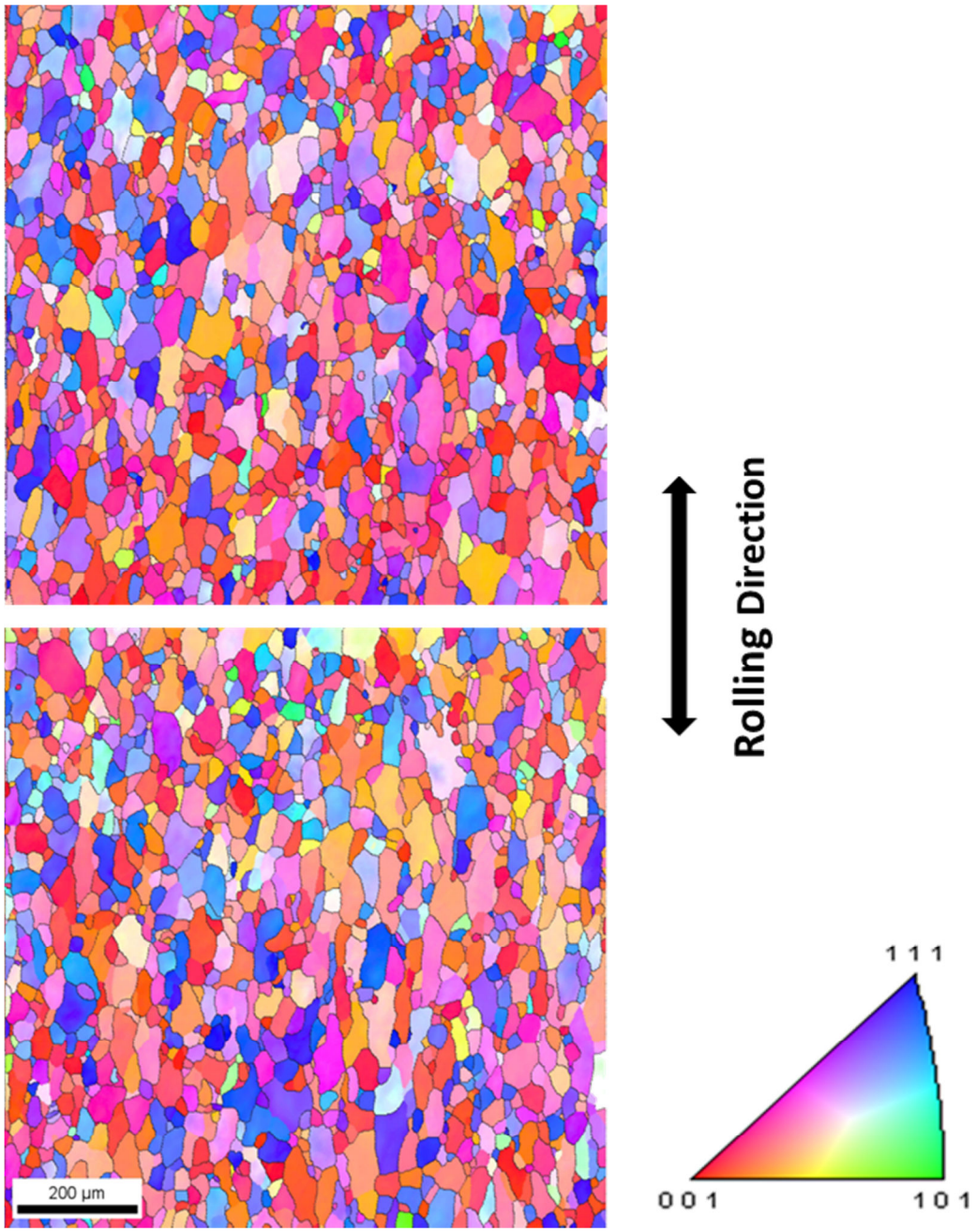

Figure 5-2: Two 1mmx1mm inverse pole figure (IPF) maps from EBSD on PM-B material statically annealed at 1650°C for 130 min. The color corresponds to the crystallographic orientation of the sheet normal (ND).

Pole figures and inverse pole figures of the AM, PM-A, and PM-B primary recrystallization textures are pictured in Figures 5-3 and 5-4, respectively. The recrystallization textures of the AM and PM-A materials are reproduced from Ciulik [3] and were measured with EBSD. In Figure 5-4, note that only the normal direction (ND) inverse-pole-figure was available for the AM and PM-A materials. The texture of the AM material is a $\{001\}\langle 110\rangle$ rotated cube texture. The $\{001\}\langle 110\rangle$ texture has been rotated approximately 20° clockwise about the ND axis. This rotation is consistent with the cross rolling that was used for processing this material. The textures of the PM materials have both α- and γ-fibers. The texture of the PM-A material has a strong γ-fiber texture and very weak α-fiber. Meanwhile, the PM-B material has an α-fiber texture and a weak γ-fiber texture. These results are summarized in Table 5-2.

Mo Sheet Material	Recrystallization Texture	Grain Shape	Static Normal Grain Growth (SGG)	Static Abnormal Grain Growth (SAGG)
AM	$\{001\}\langle 101\rangle$	Equiaxed	Yes	None
PM-A	"γ-fiber" $\{111\} \parallel ND$	Equiaxed	No	None
PM-B	Strong $\{001\}\langle 101\rangle$ Weak $\{111\}\langle 101\rangle$	Elongated	No	Some

Table 5-2: A comparison of the static recrystallization and grain growth behavior between the AM, PM-A, and PM-B materials.

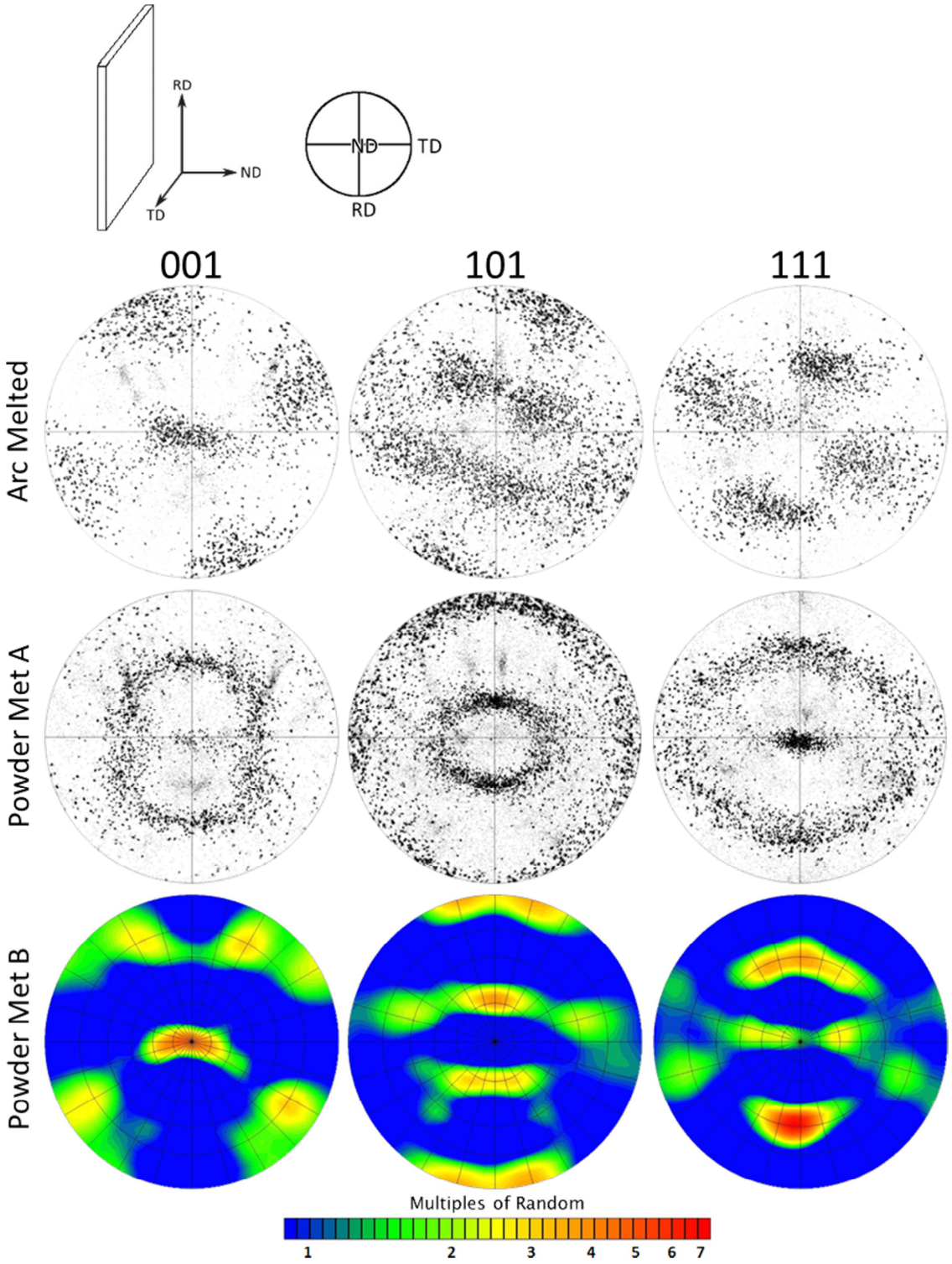

Figure 5-3: The 001, 101, and 111 pole figures for recrystallization textures of the AM, PM-A, and PM-B materials. AM and PM-A pole figures are reproduced from Ciulik [3].

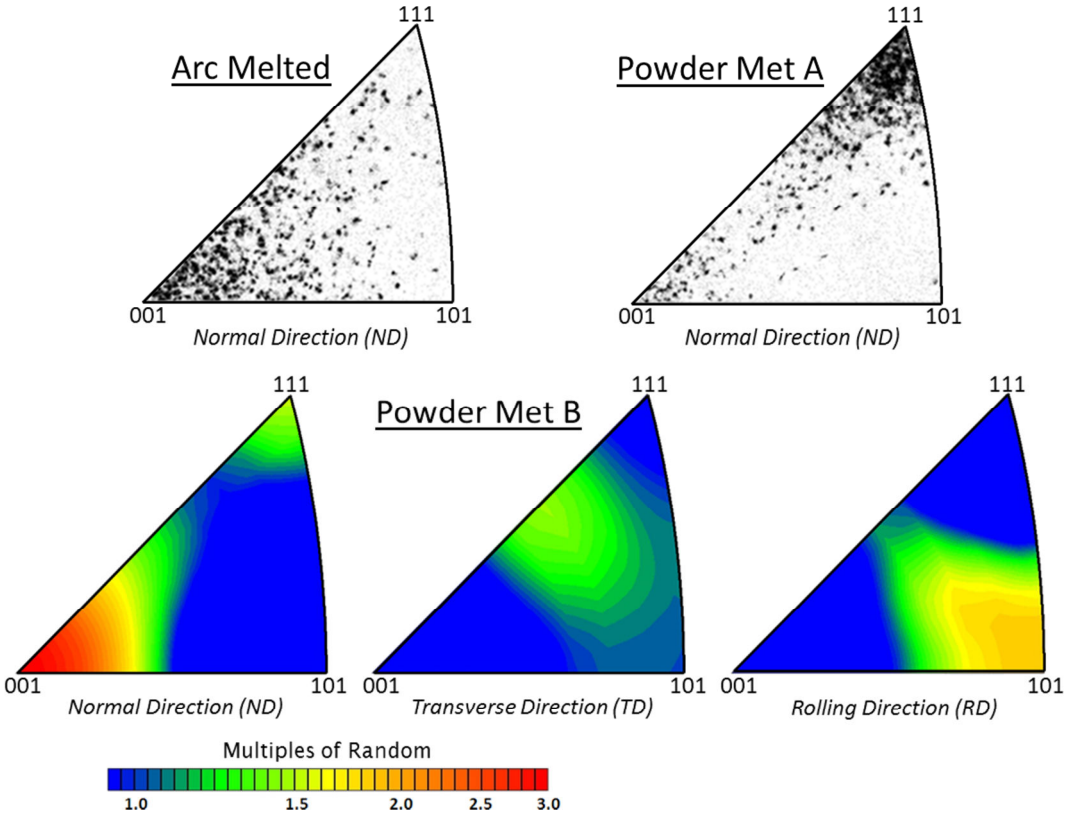

Figure 5-4: The 001, 101, and 111 inverse pole figures for the recrystallization textures of the AM, PM-A, and PM-B materials. AM and PM-A inverse pole figures are reproduced from Ciulik [3].

5.3 Static Grain Growth

The static recrystallization and static grain growth behaviors of the PM-B material were studied. The sheet was received in a deformed state. Metallography of the initial material revealed deformation in the rolling direction, as is shown in Figure 5-5.

5.3.1 Static Normal And Abnormal Grain Growth

The PM-B sheet was statically annealed at 1650°C for 10, 130, and 570 min and statically annealed at 1800°C for 130 and 570 min. Photomicrographs of these annealed microstructures are displayed in Figures 5-6 through 5-8 for 1650°C and Figures 5-9 through 5-12 for 1800°C. Grains are elongated along the rolling direction.

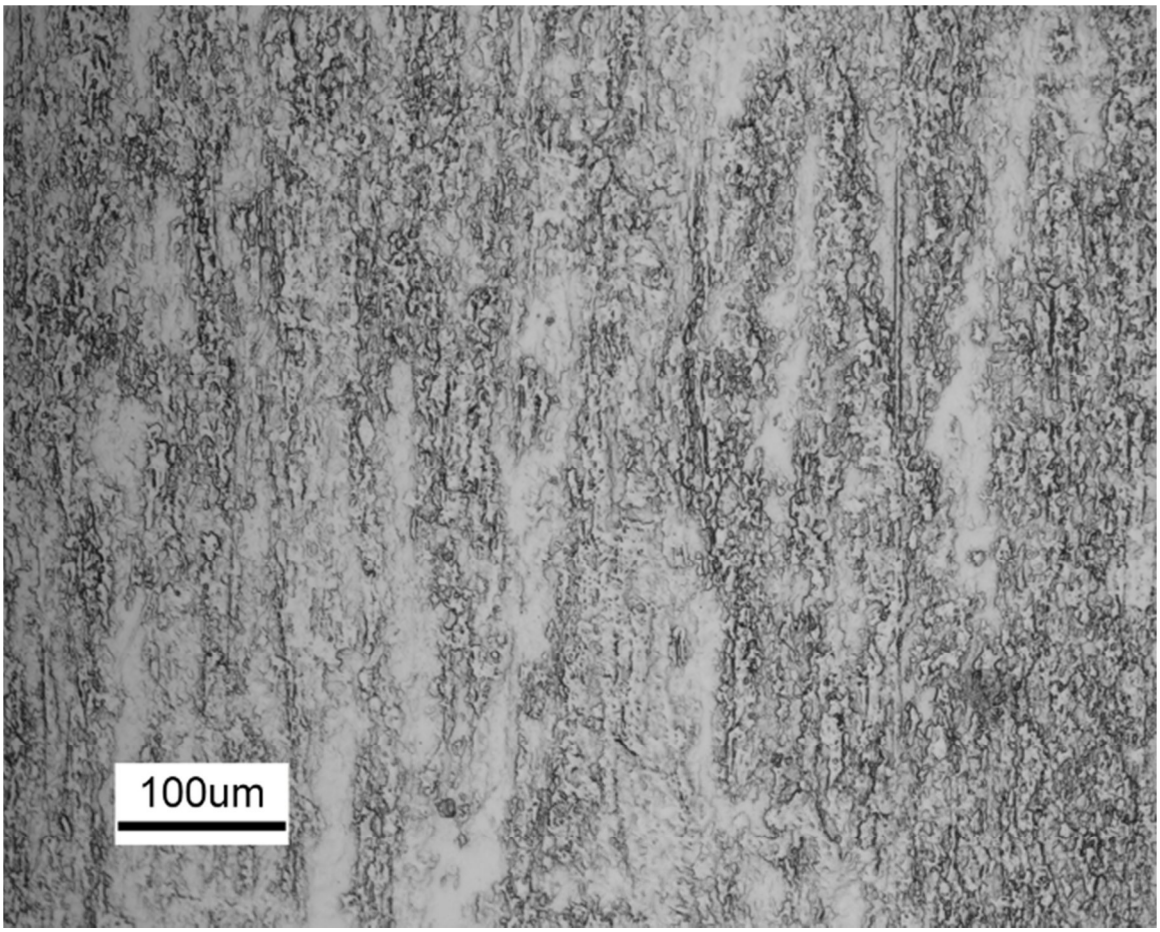

Figure 5-5: Optical photomicrograph of the as-received PM-B material. The rolling direction (RD) is vertical and the transverse direction (TD) is horizontal.

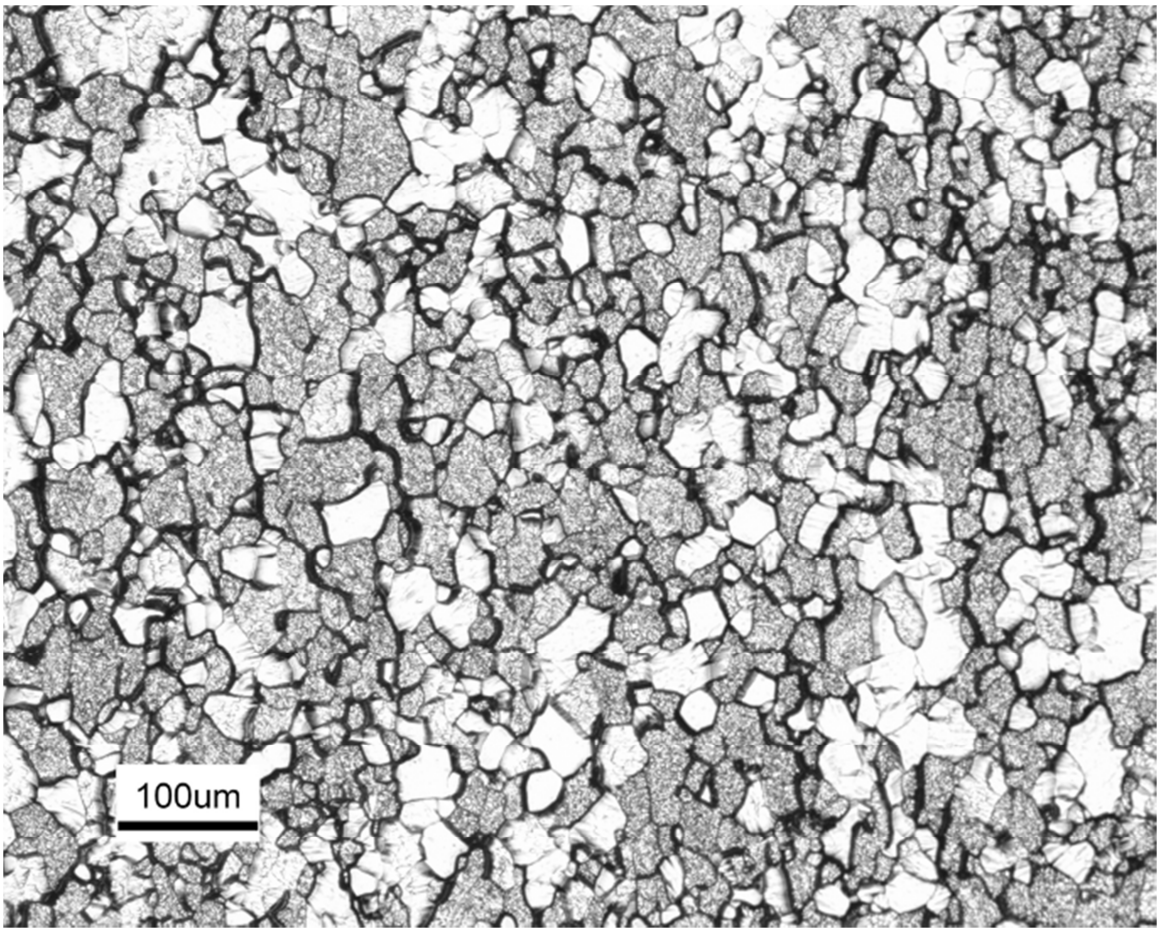

Figure 5-6: Microstructure after static annealing the PM-B material at 1650°C for 10 min. The rolling direction (RD) is vertical and the transverse direction (TD) is horizontal.

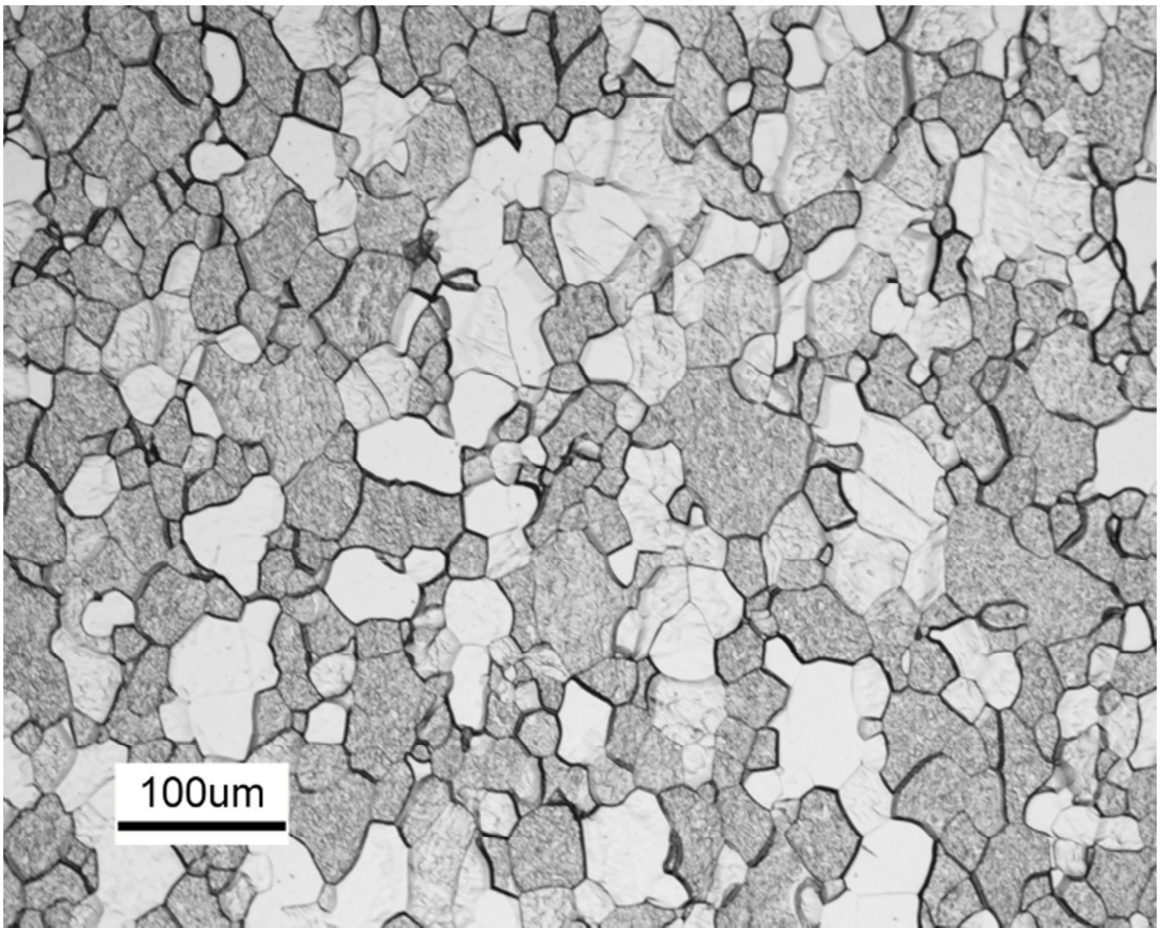

Figure 5-7: Microstructure after static annealing the PM-B material at 1650°C for 130 min. The rolling direction (RD) is vertical and the transverse direction (TD) is horizontal.

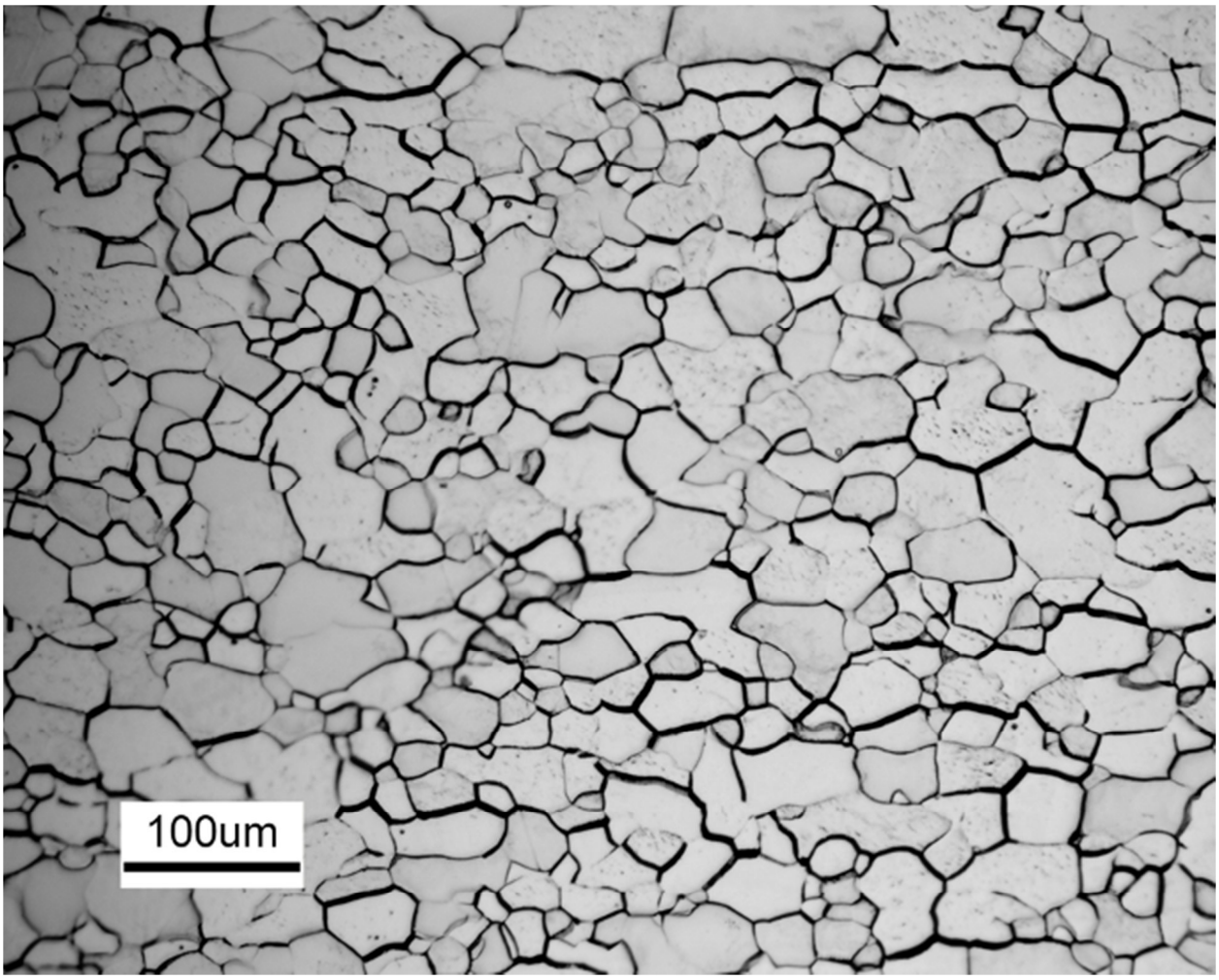

Figure 5-8: Microstructure after static annealing the PM-B material at 1650°C for 570 min. The rolling direction (RD) is vertical and the transverse direction (TD) is horizontal.

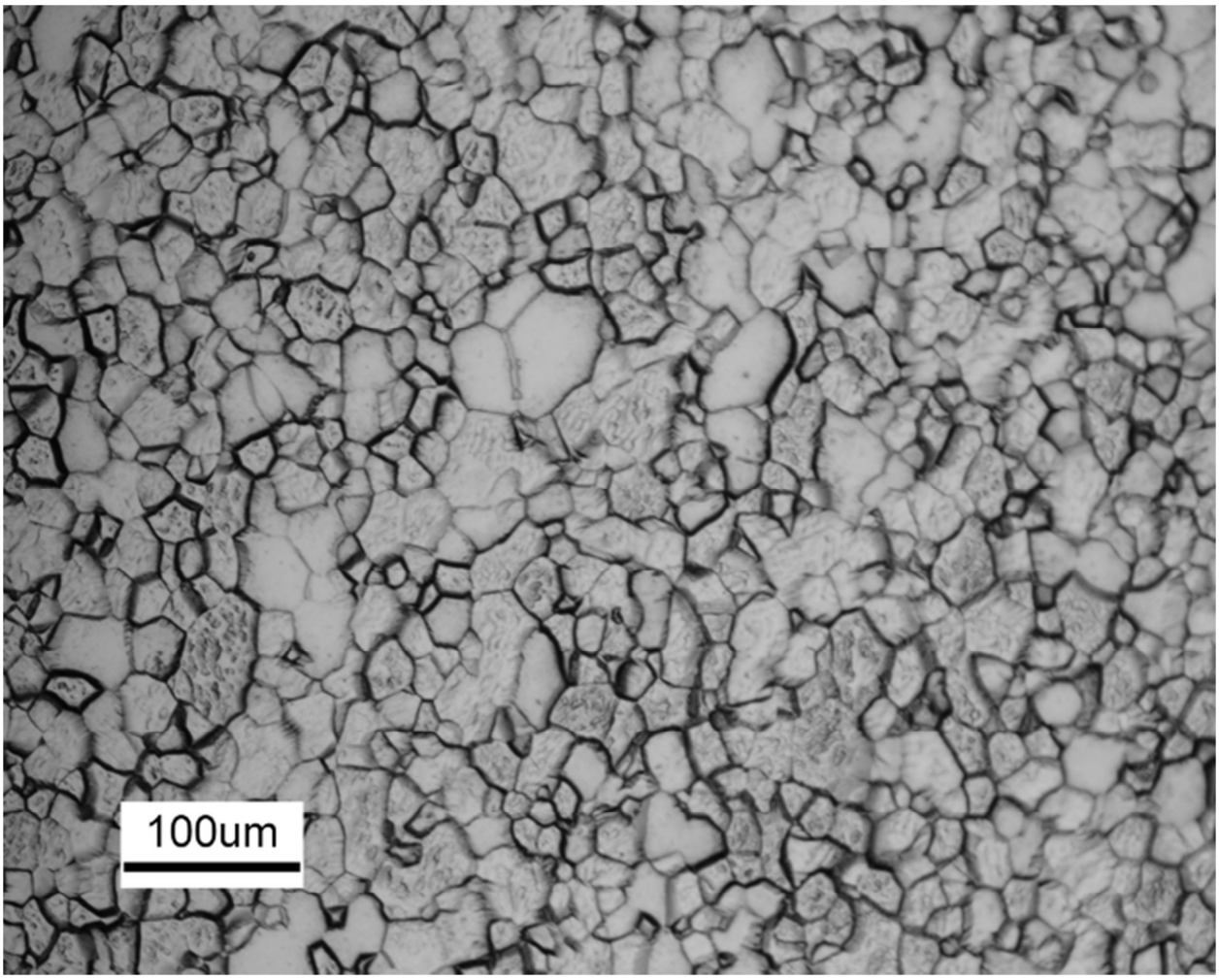

Figure 5-9: Microstructure after static annealing the PM-B material at 1800°C for 120 min. The rolling direction (RD) is vertical and the transverse direction (TD) is horizontal.

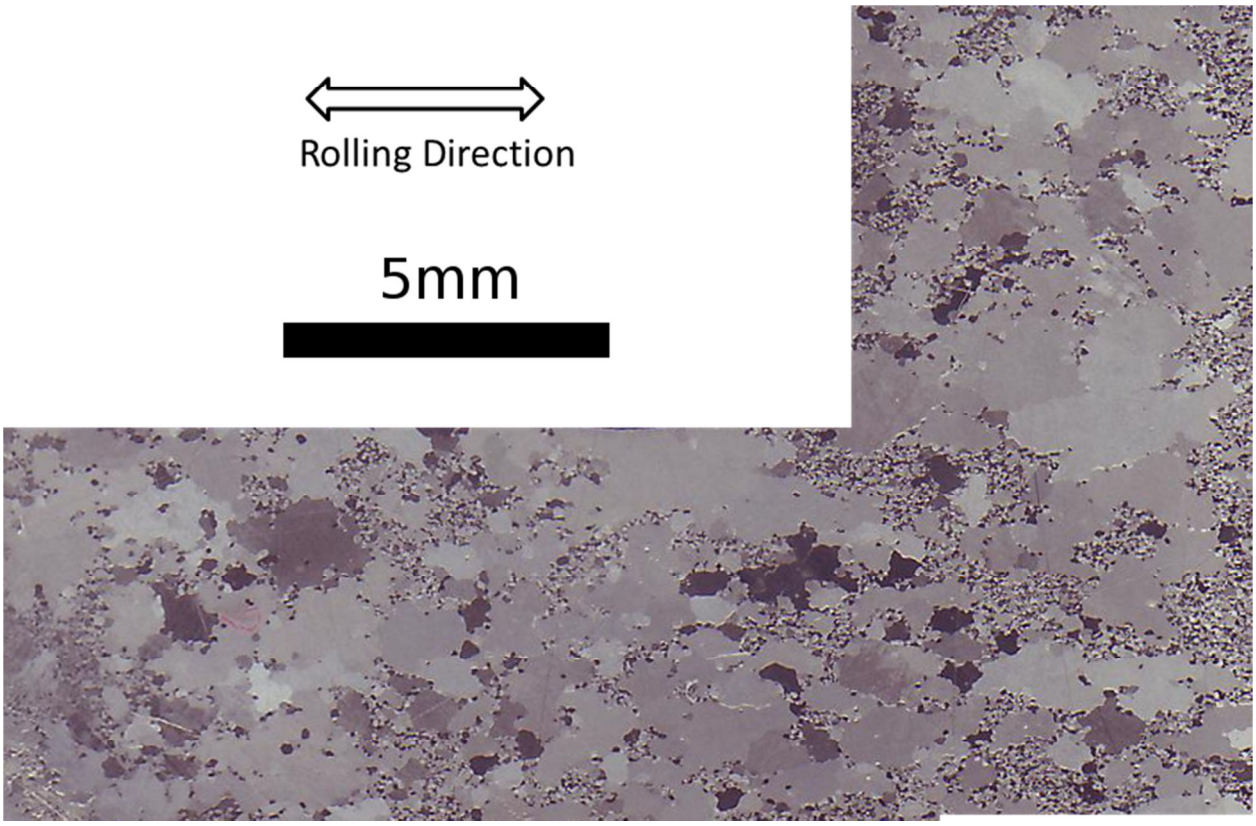

Figure 5-10: Macroetch of PM-B specimen after static annealing at 1800°C for 570 min. The rolling direction (RD) is horizontal and the transverse direction (TD) is vertical.

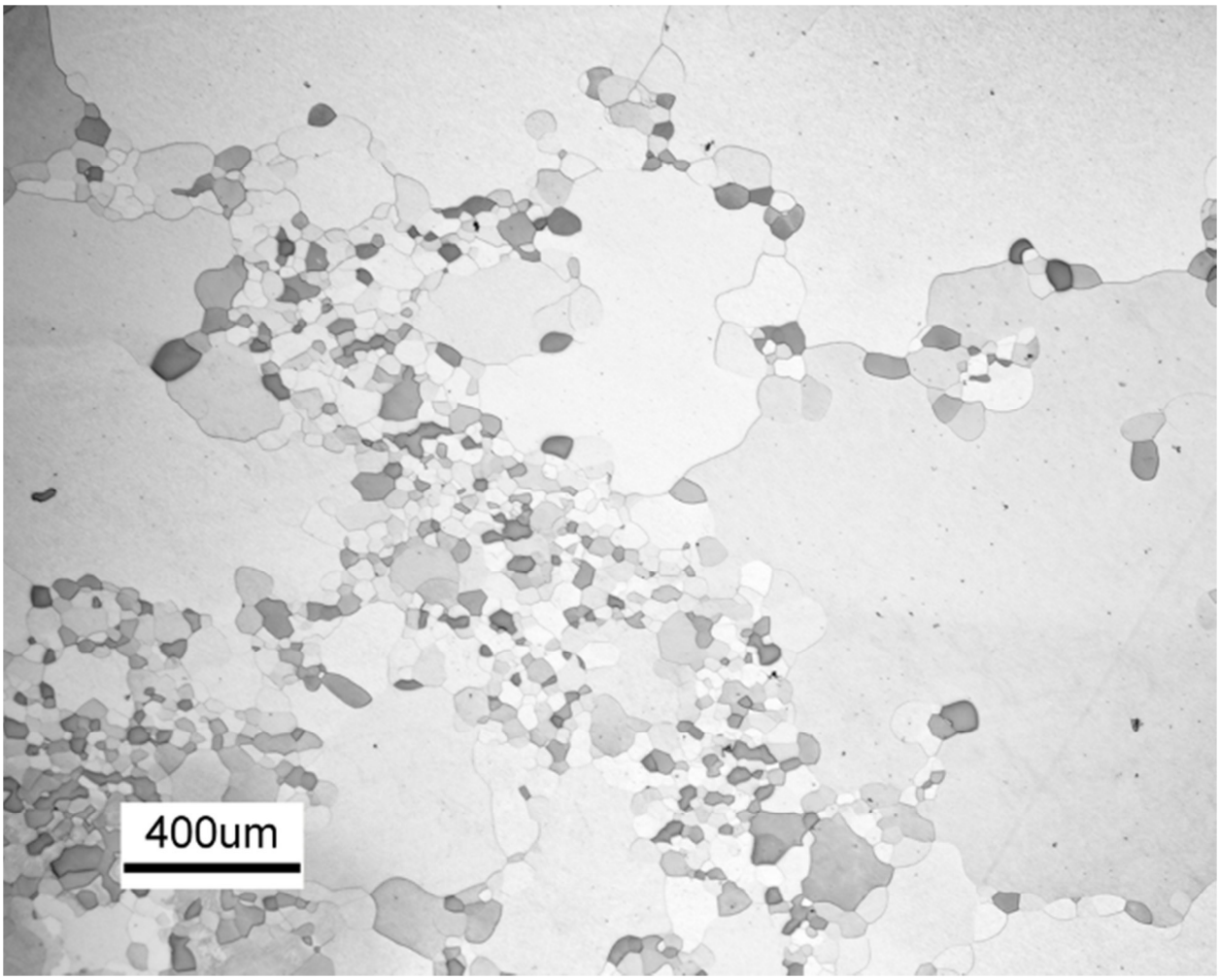

Figure 5-11: Microstructure after static annealing the PM-B material at 1800°C for 570 min and 50x. The rolling direction (RD) is vertical and the transverse direction (TD) is horizontal.

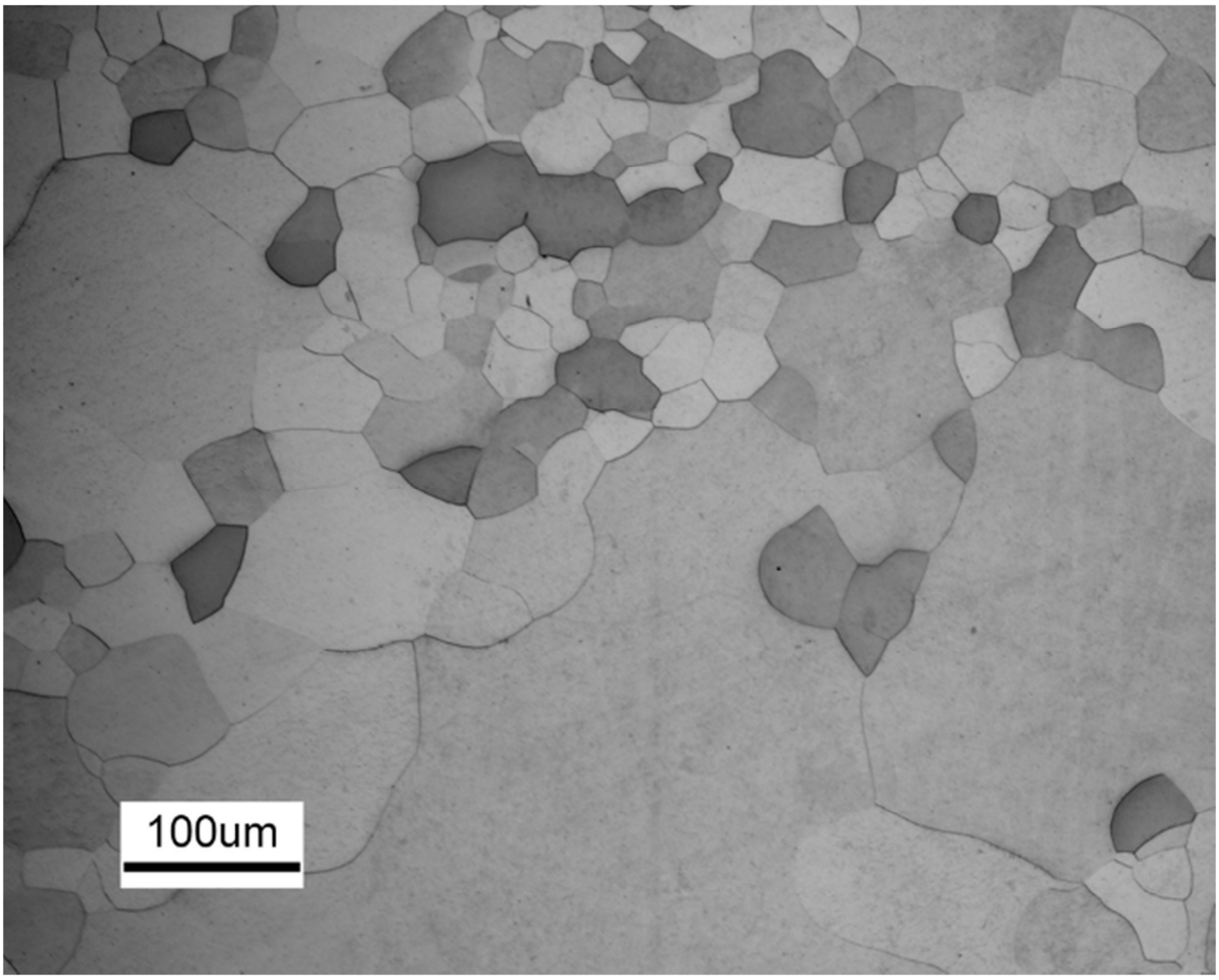

Figure 5-12: Microstructure after static annealing the PM-B material at 1800°C for 570 min and 200x. The rolling direction (RD) is vertical and the transverse direction (TD) is horizontal.

The grain size in the rolling direction, d_{RD}, and the grain size in the transverse direction, d_{TD}, are reported in Table 5-3 for each annealing time at 1650ºC. Grain sizes were measured from optical photomicrographs by the lineal intercept method. Grains initially grew during annealing at 1650ºC from 10 to 130 min; d_{RD} increased from 21 to 28 μm and d_{TD} increased from 17 to 21 μm. However, growth did not occur, to within measurement uncertainty, between 130 and 570 min. The aspect ratio of grains, d_{RD} / d_{TD} = 1.2 to 1.3, remained approximately the same during all annealing times. The lineal intercept grain size was also measured from an EBSD photomicrograph for the 130-min anneal. The EBSD grain sizes (d_{RD} = 30 and d_{TD} = 20 μm) are in good agreement with those grain sizes measured from optical photomicrographs (d_{RD} = 28 and d_{TD} = 21 μm). Grain size histograms from the EBSD dataset are pictured in Figure 5-13. Neither the d_{RD} nor the d_{TD} distributions are symmetric; there is a greater population of grains above the average grain size.

The grain sizes from 1800ºC anneals were more equiaxed than those from 1650ºC anneals, as is shown in Figure 5-9: d_{RD} = 21 and d_{TD} = 20 μm at 120 min. After 570 min at 1800ºC, static abnormal grain growth occurred in the material, and grains as large as several millimeters in diameter were observed, as is shown in Figure 5-10. Abnormal grains did not consume all normal grains. The unconsumed normal grains exhibited a grain size of ~20 μm. These results are reported in Table 5-4.

The static grain growth behavior of PM-B is different from that of AM, but similar to PM-A. Table 5-2 compares the static recrystallization and grain growth behaviors of these three different molybdenum materials. Grain size data for the AM and PM-A materials are provided in Table 5-5. Recrystallized grains are equiaxed in AM and PM-A, but grains are elongated in PM-B. Recrystallized grain size is smallest in the PM-A material, slightly larger in the PM-B material, and largest in the AM material. Static

normal grain growth (SGG) occurs in the AM material, while no SGG was observed in the PM-A or PM-B materials once a stable grain size was reached.

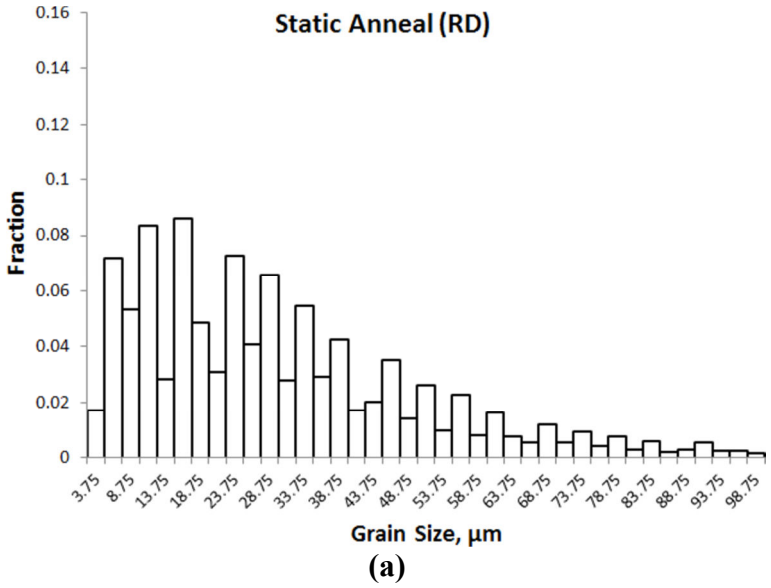

(a)

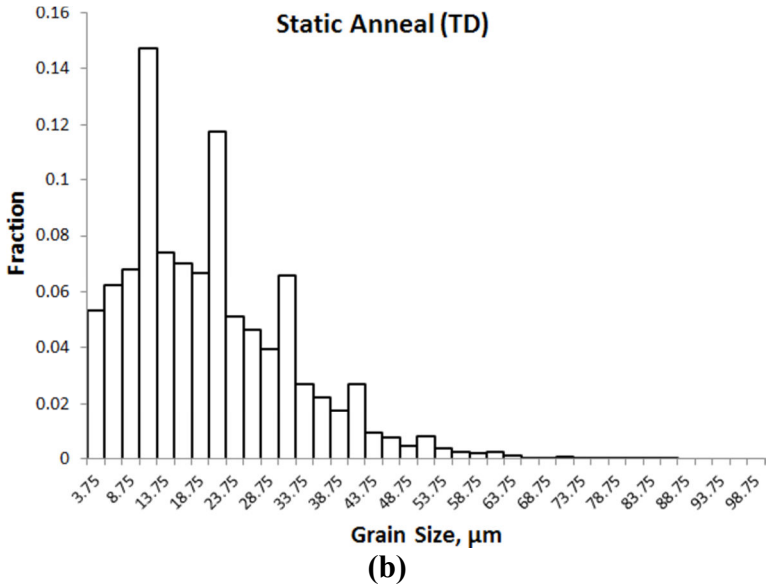

(b)

Figure 5-13: Grain size distribution in (a) the rolling direction, d_{RD}, and (b) the transverse direction, d_{TD}, from EBSD of PM-B after recrystallization at 1650°C for 130 min.

Annealing Time (min)	Characterization Technique	RD Grain Size, d_{RD}† (μm)	TD Grain Size, d_{TD}† (μm)	Grain Size Aspect Ratio, d_{RD} / d_{TD}
10	Metallography	21 ± 3	17 ± 3	1.2
130	Metallography	28 ± 9	21 ± 5	1.3
	EBSD	30 ± 20	20 ± 12	1.5
570	Metallography	27 ± 5	22 ± 3	1.2

Table 5-3: Grain sizes for static anneals at T = 1650 °C in the PM-B material.

Annealing Time (min)	Characterization Technique	RD Grain Size, d_{RD}† (μm)	TD Grain Size, d_{TD}† (μm)	Grain Size Aspect Ratio, d_{RD} / d_{TD}
120	Metallography	21 ± 3	20 ± 3	1.1
570	Metallography	Bimodal microstructure due to Static Abnormal Grain Growth. Remaining fine grains are equiaxed and d~20 μm. Largest abnormal grains are 100s of mm in size.		

Table 5-4: Grain sizes for static anneals at T = 1800 °C in the PM-B material.

†Both metallography and EBSD grain sizes were measured with the lineal intercept method. The uncertainty values for metallography grain sizes are between the average grain size from lines each containing approximately 30 to 100 grains, while the uncertainty values for EBSD grain sizes are between individual grains.

Annealing Time (min)	Grain Size† (μm)	
	AM	PM-A
180	98 ± 8	19 ± 1
504	165 ± 20	18 ± 1

Table 5-5: Grain sizes for static anneals at T = 1640 °C in the AM and PM-A materials. These data are from Ciulik [3].

†Both metallography and EBSD grain sizes were measured with the lineal intercept method. The uncertainty values for metallography grain sizes are between the average grain size from lines each containing approximately 30 to 100 grains, while the uncertainty values for EBSD grain sizes are between individual grains.

No static abnormal grain growth (SAGG) was observed in the PM-B sheet at 1650ºC, even after 570 min. However, SAGG was observed in PM-B after 570 min at 1800ºC, as is shown in Figures 5-10 to 5-12. These abnormal grains, whose largest size was 5 mm, are much smaller than those observed during DAGG. No SAGG was observed during the static anneals of the AM or PM-A materials.

5.3.2 PINNING PARTICLES

Second-phase particles were not characterized in the molybdenum materials. However, their presence is expected because of the observed grain growth behaviors. Fine particles can pin grain boundaries and prevent grain growth. Likely candidates for dispersed particles are oxides, sulfides, nitrides, and carbides [48]. Since the concentration of oxygen is larger in both the PM-A and PM-B materials than that of the AM material, the pinning particles may be MoO_2. Molybdenum dioxide is known to coat grain boundaries in molybdenum [7], while molybdenum trioxide volatilizes well below the test temperature (600°C [49, p.156]),

The absence of static normal grain growth (SGG) in the powder metallurgy materials, PM-A and PM-B, is not surprising. Sintered materials are prone to contamination because powder has a large ratio of surface area to volume. This behavior and processing route implies the existence of particles that pin grain boundaries against growth. The presence of significant SGG in the AM material at a similar temperature (1640°C) and similar annealing times (180 min and 500 min) indicates any particles present in the AM material were not very effective at pinning grain boundaries.

5.4 Chapter Summary

(1) The primary recrystallization textures of the materials were:

AM	$\{001\}\langle 101\rangle$ rotated 20º clockwise
PM-A	strong γ-fiber and very weak α-fiber
PM-B	strong α-fiber and weak γ-fiber

(2) During static annealing, the PM material microstructures reached stable grain sizes through static normal grain growth (SGG):

PM-A	d = 19 μm	at 1540 ºC
PM-B	d_{RD} = 28 μm; d_{TD} = 21 μm	at 1640 ºC

The AM material did not reach a stable grain size, and grains grew as large as 165 μm in diameter through SGG. This difference in growth behavior is attributed to a larger concentration of (oxide) particles, which may pin grain boundaries, in PM-A and PM-B (34 and 40 ppm O, respectively), than in AM (<10 ppm O).

(3) Static abnormal grain growth (SAGG) initiated between 120 and 570 min in PM-B at 1800ºC. The largest SAGG grains produced were approximately 5mm in diameter.

6 DYNAMIC ABNORMAL GRAIN INITIATION

The initiation of DAGG grains was investigated in the PM-B material through a series of high-temperature tensile tests. As previously described in Chapter 4, some tests were conducted to specimen rupture, while other tests were halted after DAGG initiation.

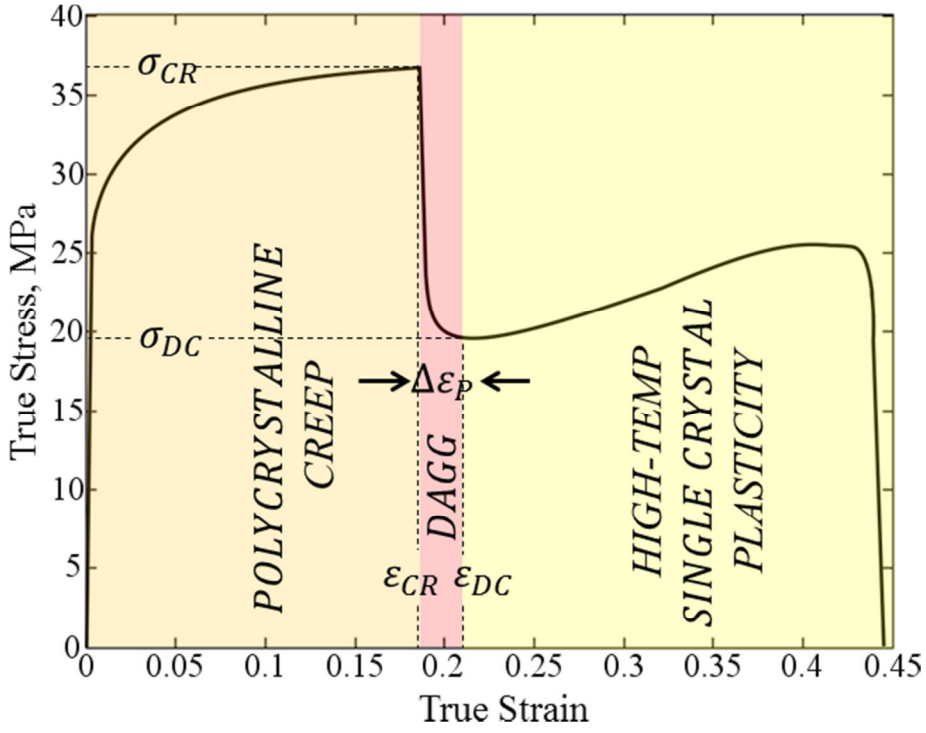

Figure 6-1: Stress-strain curve for PM-B material at $\dot{\boldsymbol{\varepsilon}}=10^{-4}$ s^{-1} and T=1650°C. Specimen strained to failure.

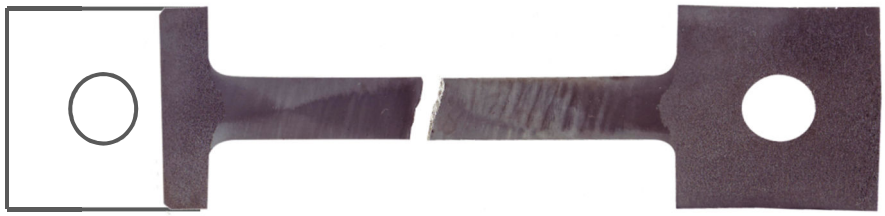

Figure 6-2: Macroetched PM-B specimen after fracture of test in Figure 6-1. One single crystal, the DAGG grain, spans the gauge length. Polycrystalline microstructure is retained in grip region. Contrast difference along the DAGG grain are from slip bands and from artifacts of metallographic preparation, primarily issues with faceting.

The stress-strain curve of a specimen strained to failure at $\dot{\varepsilon}$=10^{-4} s^{-1} and T=1650°C is shown in Figure 6-1. This stress-strain curve is representative of many important features of DAGG. Polycrystalline creep (see Figure 2-2) occurs until the initiation of a DAGG grain. Initiation corresponds to an abrupt drop in flow stress which occurs at a critical strain, ε_{CR}. This drop reflects a microstructural transition in the gauge length from polycrystalline to single-crystal forms; i.e. consumption of the hot-deformed polycrystal by a DAGG grain. The DAGG completion strain, ε_{DC}, occurs when a DAGG grain(s) has grown throughout the entire gauge length of the specimen. Subsequent straining results in single-crystal plasticity of the DAGG grain(s). The amount of accumulated plastic strain across the flow stress drop is $\Delta\varepsilon_P = \varepsilon_{DC} - \varepsilon_{CR}$. The critical flow stress for DAGG, $\sigma_{CR} = \sigma(\varepsilon_{CR})$, and DAGG completion flow stress, $\sigma_{DC} = \sigma(\varepsilon_{DC})$, are the flow stresses which correspond to the critical strain and completion strain, respectively.

The fractured specimen from the test in Figure 6-1 was macroetched and is pictured in Figure 6-2. The gauge length consists of a large single crystal, and the grip regions retain a polycrystalline microstructure. The majority of tests were halted at a strain between ε_{CR} and ε_{DC}, such that a DAGG grain initiated but did not grow throughout the entire gauge length of the specimen. The stress-strain curve of a halt test at $\dot{\varepsilon}$=10^{-4} s^{-1} and T=1650°C is shown in Figure 6-3. In specimens subjected to such halt tests, there are three distinct microstructural regions: (1) the DAGG grain(s), (2) the hot-deformed polycrystal, and (3) the statically annealed polycrystal (grip region). These regions are represented schematically in Figure 6-4. DAGG grains and the hot-deformed material are characterized in this chapter to investigate DAGG initiation. The static primary recrystallization behavior was presented in Chapter 5.

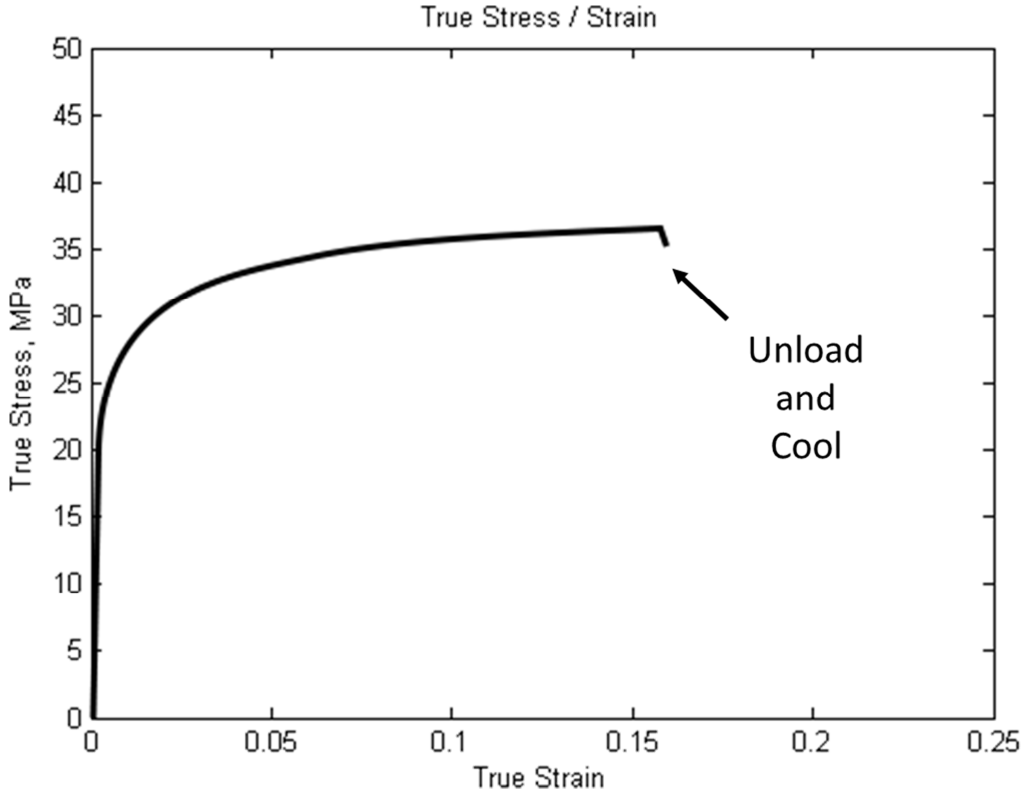

Figure 6-3: Stress-strain curve of PM-B material at $\dot{\varepsilon}=10^{-4}$ s^{-1} and T=1650°C. Specimen halted after DAGG initiation.

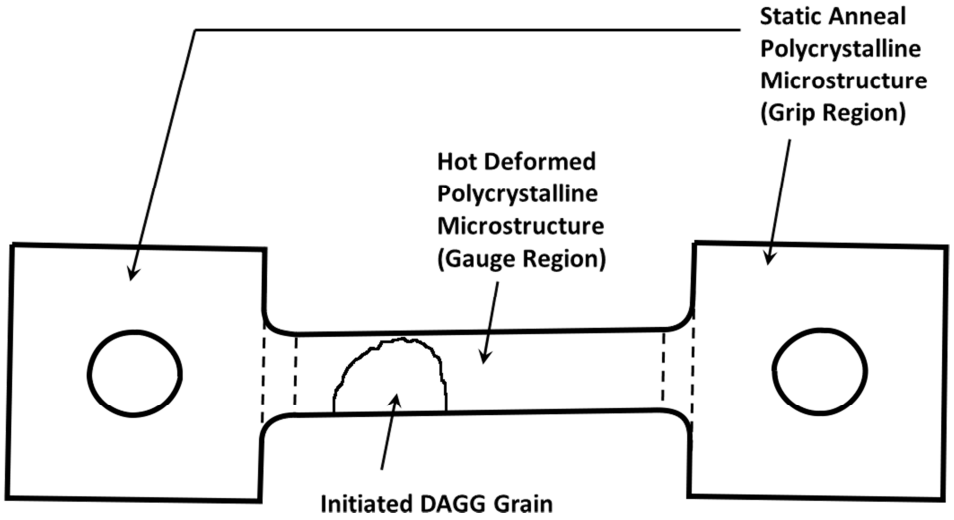

Figure 6-4: Schematic of different regions in a PM-B specimen strained at $\dot{\varepsilon}=10^{-4}$ s^{-1} and T=1650°C. Specimen halted after initiation of DAGG grain.

6.1 Effect of Temperature

Stress-strain curves of tests of PM-B material at $\dot{\varepsilon}=10^{-4}$ s^{-1} and four different temperatures (1450, 1550, 1650, and 1800°C) are plotted in Figure 6-5. Table 6-1 provides a summary of results from these data. The 1450°C test was strained to failure, while tests at the other temperatures were halted after DAGG initiation. DAGG occurred in every specimen except the 1450°C specimen, as evidenced by the flow stress drops at 1550°C, 1650°C, and 1800°C. Post-test characterization of the specimens, as shown in Figure 6-6, confirmed the absence of DAGG grains in the 1450°C specimen and the existence of DAGG grains in the 1550°C, 1650°C, and 1800°C specimens. Therefore, a minimum temperature exists for DAGG between 1450 and 1550°C in the PM-B material. This is similar to the PM-A material, for which a minimum temperature of between 1440 and 1540°C was observed for DAGG [3]. The critical strain for DAGG initiation, ε_{CR}, decreases with increasing temperature, as shown in Table 6-1 and Figure 6-5.

The effect of temperature on critical strain likely results from the temperature dependence of grain boundary mobility. A simple grain boundary migration model predicts an Arrhenius dependence of mobility on temperature (Equation 3-3). Grain boundaries are increasingly mobile with increasing temperature. Therefore, the boundaries of grains selected for abnormal growth may propagate more readily and may not require as much plastic strain accumulation to initiate the boundary motion required for DAGG. Furthermore, the minimum temperature required for DAGG may be the result of a minimum required mobility of grain boundaries.

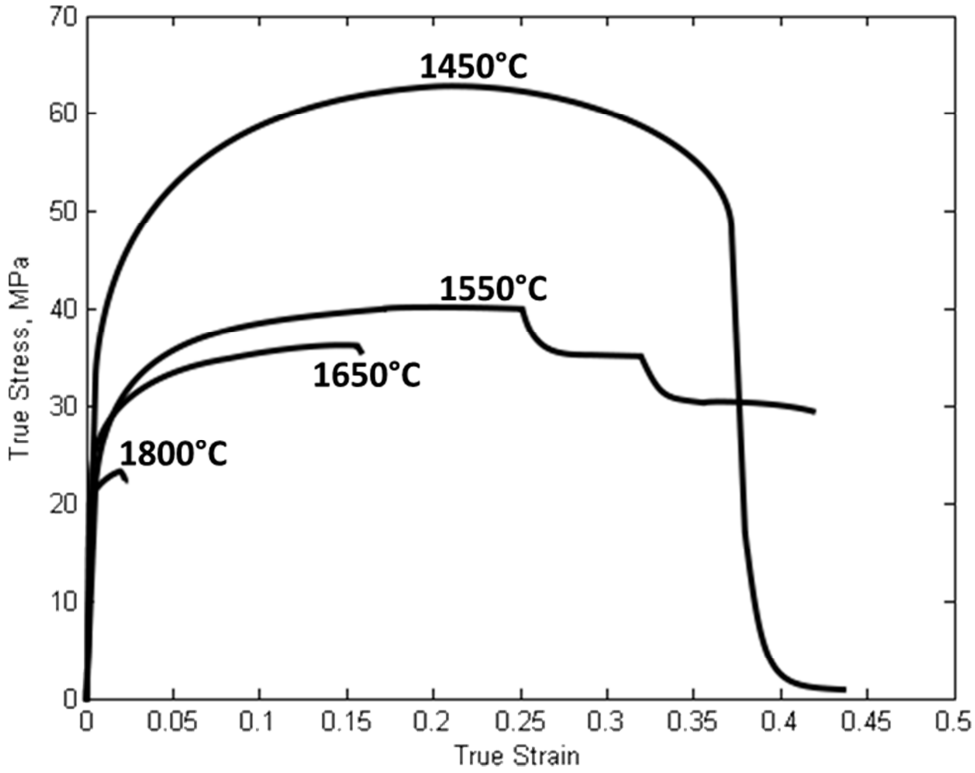

Figure 6-5: Stress-strain data for PM-B material at $\dot{\varepsilon} = 10^{-4}$ s^{-1} and T = 1450°C, 1550°C, 1650°C, and 1800°C. Note that true stress and strain after UTS (ultimate tensile strength) in the 1450°C are not accurate because of neck development and are shown only for qualitative comparison.

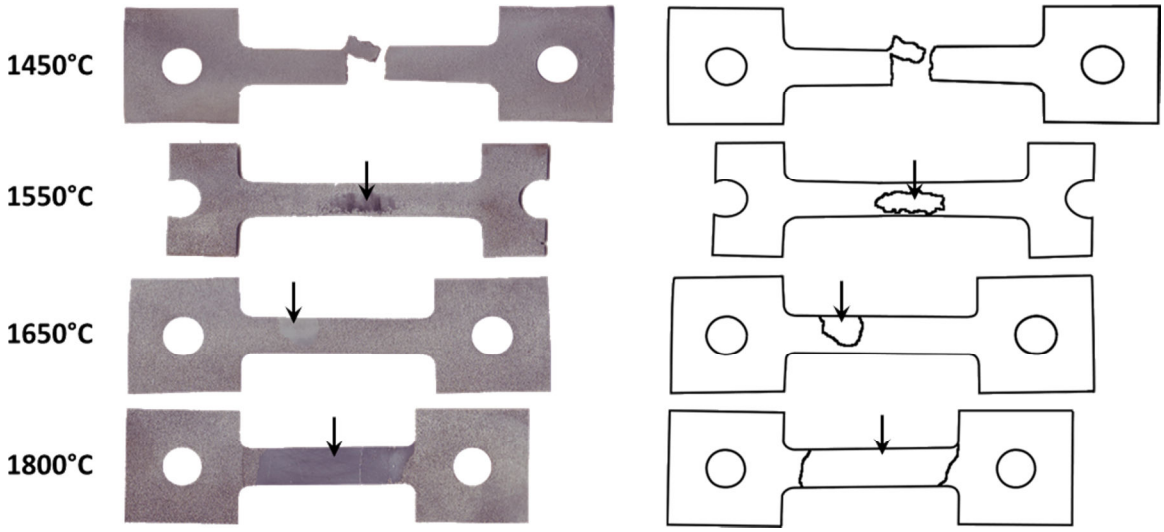

Figure 6-6: Macroetched PM-B specimens strained at $\dot{\varepsilon}=10^{-4}$ s^{-1} and T = 1450°C, 1550°C, 1650°C, and 1800°C. DAGG grains denoted by black arrows.

Temperature (°C)	Test Type	Steady State Creep Achieved?	Dynamic Abnormal Grain Growth (DAGG)	Critical Strain, ε_{CR}	Critical Flow Stress, σ_{CR} (MPa)
1450	Strain to Failure	No	No	-	-
1550	Halt	Yes	Yes	0.25	40.3
1650	Halt	No	Yes	0.16	36.4
1800	Halt	No	Yes	0.02	23.5

Table 6-1: Summary of the four tests at different temperatures from Figure 6-5 for PM-B material.

Temperature (°C)	Critical Strain, ε_{CR}	Critical Flow Stress, σ_{CR} (MPa)
1650	0.152 ± 0.0549 (± 36.2%)	35.9 ± 1.38 (± 3.86%)
1800	0.0234 ± 0.00969 (± 41.4%)	23.3 ± 0.966 (± 4.15%)

Table 6-2: Averaged critical values for DAGG initiation in the PM-B Material at 1650°C (22 tests) and 1800°C (7 tests).

Halt Strain, ε_H	Pre-Heat Time (min)	Test Time (min)	Characterization Technique	TLD Grain Size, d_{TLD}† (µm)	LTD Grain Size, d_{LTD}† (µm)	STD Grain Size, d_{STD}† (µm)	Grain Size Aspect Ratio, d_{TLD} / d_{LTD}
0.15	100	25	EBSD	27 ± 18	22 ± 13	-	1.2
0.16	100	27	Metallography	22 ± 6	22 ± 9	-	1.0
0.12	100	20	Metallography	24 ± 5	22 ± 4	18 ± 5	1.1

Table 6-3: Grain sizes for hot deformed microstructures at T = 1650 °C in the PM-B material for three tests halted upon DAGG initiation.

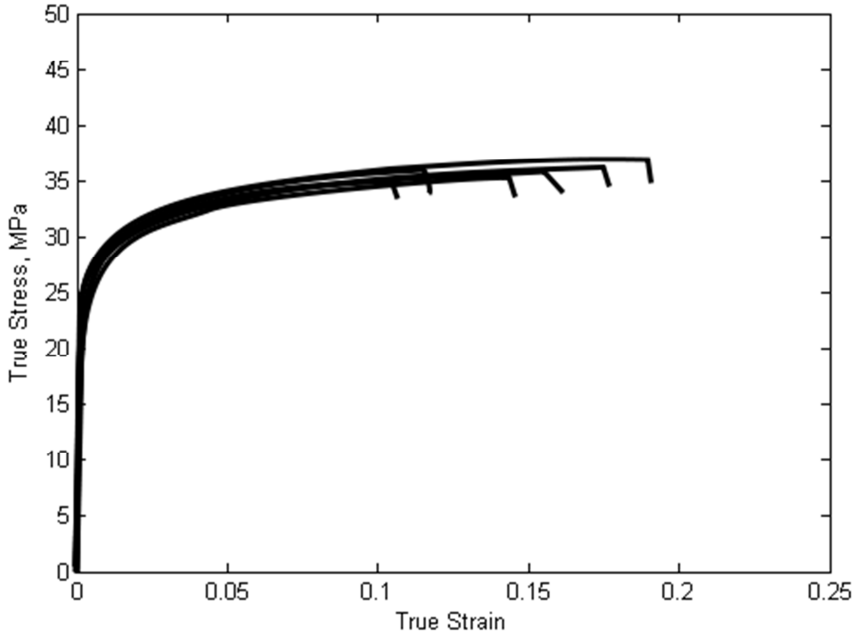

Figure 6-7: Stress-strain curves strained at $\dot{\varepsilon}=10^{-4}$ s^{-1} and T=1650°C for different tests in PM-B material. Specimens halted after initiation of DAGG grain.

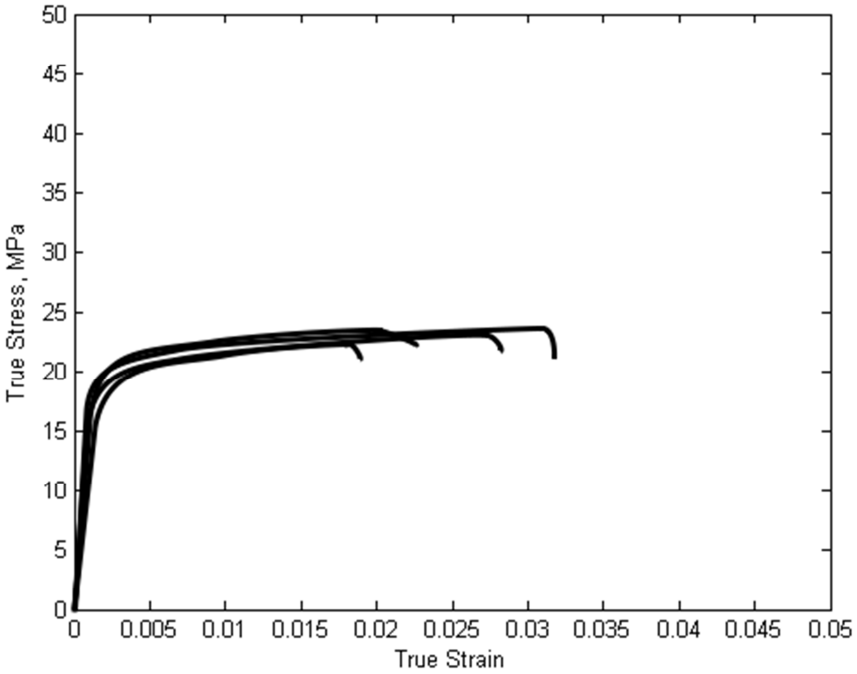

Figure 6-8: Stress-strain curves strained at $\dot{\varepsilon}=10^{-4}$ s^{-1} and T=1800°C for different tests in PM-B material. Specimens halted after initiation of DAGG grain.

There is a significant variation in critical strain between multiple tests at the same strain-rate and temperature. Twenty-two specimens were tested at $\dot{\varepsilon}$=10^{-4} s^{-1} and T=1650°C, and seven specimens were tested at $\dot{\varepsilon}$=10^{-4} s^{-1} and T=1800°C. Several of the stress-strain curves from these tests are plotted in Figures 6-7 and 6-8. Table 6-2 presents averaged data from these tests and indicates that ε_{CR} varies by approximately ±40% (95% confidence interval, CI_{95}) at both 1650°C and 1800°C. On the other hand, σ_{CR} varies by approximately ±4% CI_{95} at both 1650°C and 1800°C. The incubation period for DAGG initiation, t_I, is necessarily correlated with critical strain in constant true strain-rate tests, where $t_I = \varepsilon_{CR}/\dot{\varepsilon}$. As a result, t_I varies ±40% CI_{95} because ε_{CR} varies ±40%. The large variation of ε_{CR} relative to σ_{CR} is primarily due to the approach of a steady-state flow stress, σ_{SS}, by gradual hardening prior to DAGG initiation. It should also be noted that the dependence of ε_{CR} on temperature is very strong, much larger than the ±40% variation in ε_{CR} observed from tests at constant strain rate and temperature.

6.2 Creep Behavior Prior to DAGG Initiation

As expected for creep, the flow stress decreases with increasing temperature. The flow stress approached a steady-state value in each test; however, steady-state creep was only achieved in the 1550°C test. DAGG initiation occurred before steady-state creep was reached in the 1650°C and 1800°C tests, while brittle fracture began before steady-state creep in the 1450°C test. The steady-state flow stresses at 1450°C and 1650°C for $10^{-4}s^{-1}$ were estimated by fitting to the (true) stress-strain data an exponential curve of the form,

$$y = a - \exp(-bx)$$

such that the root-mean-squared error was minimized. The value of a in this equation is the asymptote of the curve which represents steady state. These steady-state flow stress values were then utilized to calculate the activation energy for creep. The phenomenological equation for creep (Equation 2-1) was rearranged as follows:

$$Z = \dot{\varepsilon}_{ss} exp\left(\frac{Q}{RT}\right) = A\left(\frac{\sigma}{E}\right)^{n} \tag{6-1}$$

$$n\, ln\left(\frac{\sigma}{E}\right) = ln\left(\frac{\dot{\varepsilon}_{ss}}{A}\right) + \left(\frac{Q}{RT}\right)$$

$$\underbrace{ln\left(\frac{\sigma}{E}\right)}_{y} = \underbrace{ln\left(\frac{\dot{\varepsilon}_{ss}}{A}\right)/n}_{b} + \underbrace{\left(\frac{Q}{nR}\right)}_{m}\underbrace{\left(\frac{1}{T}\right)}_{x} \tag{6-2}$$

where σ is the flow stress, E is the temperature-dependent dynamic unrelaxed Young's modulus for molybdenum, $\dot{\varepsilon}_{ss} = 10^{-4}s^{-1}$ is the constant strain rate, A is a material constant, n is the stress exponent, Q is the activation energy for creep, R is the universal gas constant, and T is the absolute temperature. The temperature-dependent dynamic unrelaxed modulus was calculated from data of Armstrong and Brown [50]. Molybdenum exhibits five-power steady-state creep behavior [4], and $n = 5$ was used in the activation enthalpy calculation.

The activation energy was calculated to be Q = 360 kJ/mol, as seen in Figure 6-9. The activation energy value of 360 kJ/mol is larger than that of 240 kJ/mol calculated by Ciulik for the PM-A material [4] and is closer to the activation energy of 386-405 kJ/mol for self-diffusivity in molybdenum [51]. However, this creep activation energy value has significant uncertainty due to the small number of data points and the approximation of steady-state flow stress values.

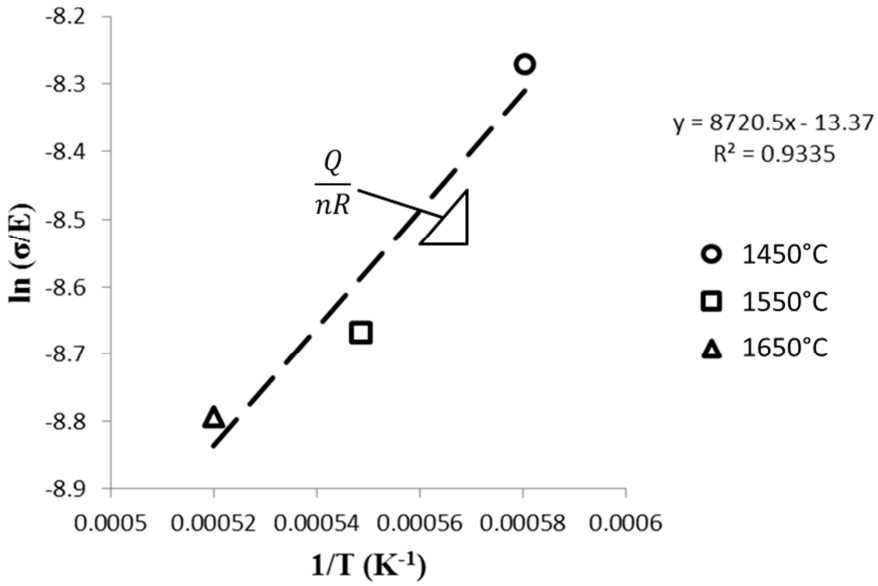

Figure 6-9: Plot showing how activation enthalpy for creep in PM-B material was calculated from test data in Figure 6-5.

6.3 Hot Deformed Material

Specimens were halted after DAGG grains initiated but before DAGG grains grew throughout the entire gauge length, as shown schematically in Figure 6-4. The unconsumed region of the gauge length was hot deformed polycrystal. This hot deformed polycrystal represents the microstructural state at DAGG initiation. DAGG grains initiate from this microstructure, and DAGG grains consume this microstructure if the specimen is strained further.

6.3.1 Grain Size

Table 6-3 reports the lineal intercept grain size of the hot deformed microstructure in three PM-B specimens tested at $\dot{\varepsilon}=10^{-4}$ s^{-1} and T=1650°C. Grain sizes for the hot deformed microstructure were obtained from optical micrographs such as Figure 6-10 or the EBSD inverse-pole-figure map in Figure 6-11. The hot deformed microstructures were equiaxed or slightly elongated with d_{LTD} / d_{TLD} grain size aspect ratios of 1.0, 1.1,

and 1.2. The LTD grain size obtained from EBSD, d_{LTD} = 27 μm, was larger than the LTD grain sizes obtained from optical photomicrographs, d_{LTD} = 22 and 24 μm. The smaller optical grain sizes could result from etching of subgrain boundaries. In EBSD, subgrain boundaries can be distinguished from high angle grain boundaries, and subgrain boundaries are not counted in grain size measurements. Material differences in the sheet could also account for the grain size variation. On the other hand, the LTD grain sizes were the same for both EBSD and optical photomicrographs, where d_{LTD} = 22 μm for all hot deformed microstructures studied. Grain size histograms from the hot deformed EBSD dataset are shown in Figure 6-12. Neither d_{TLD} nor d_{LTD} distributions are symmetric; there is a higher population of grains below the average grain size. Grain boundaries migrate until they impinge on another grain or they become pinned by a particle. Therefore, most grains will be limited in size while a few will be able to become unpinned and grow larger as the material is annealed for long periods of time.

The PM-B specimens were machined in the T orientation, as shown in Figure 4-2. The tensile loading direction (TLD) of the specimens is along the transverse direction (TD) of the sheet, and the long transverse direction (LTD) of the specimens is along the rolling direction (RD) of the sheet. Therefore, a comparison between (1) the hot deformed grain sizes, d_{TLD} and d_{LTD}, and (2) their respective statically annealed grain sizes, d_{TD} and d_{RD}, illustrates difference between the dynamic and static growth conditions. The statically annealed grain sizes for 1650°C were previously reported in Table 5-2. The static annealing time of 130 min is comparable to the total time the hot deformed specimens were at temperature during testing.

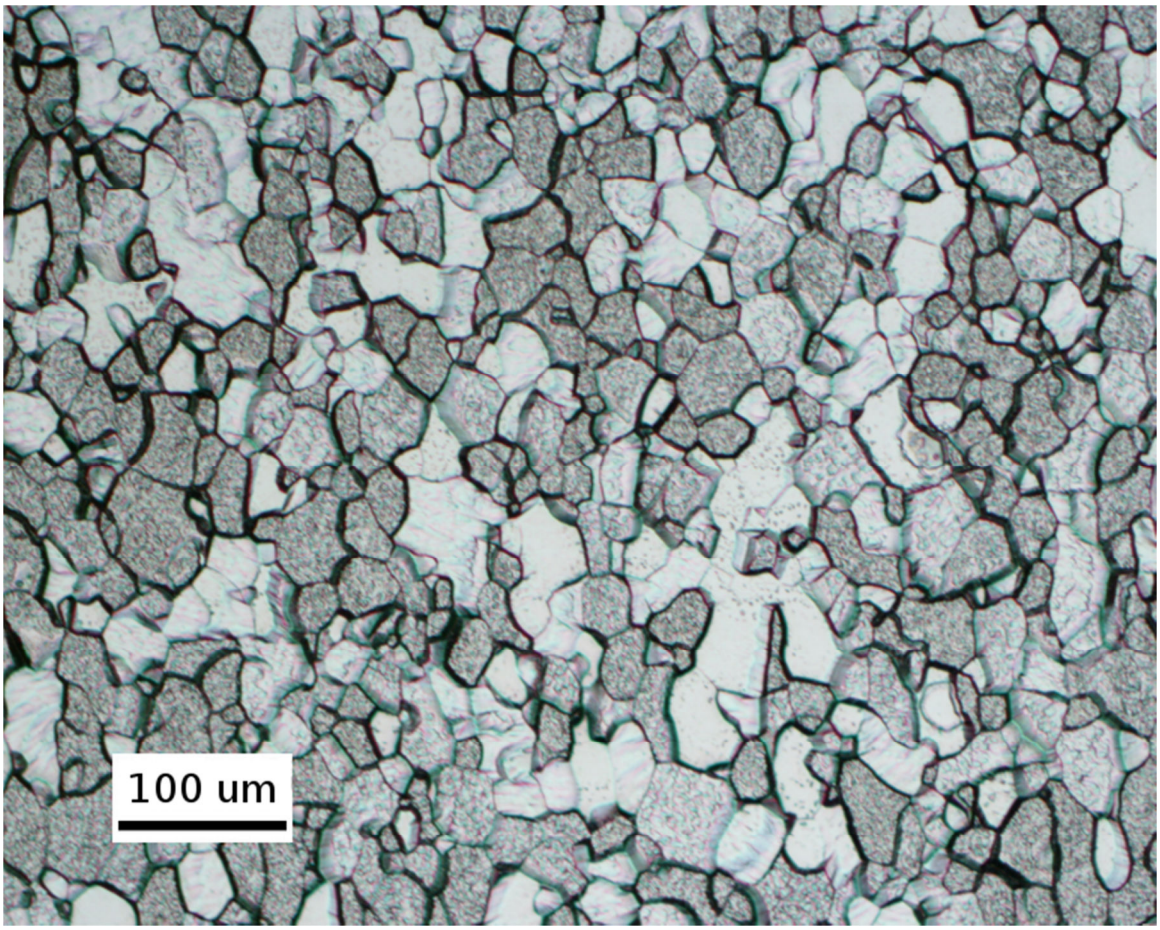

Figure 6-10: Optical photomicrograph of hot deformed PM-B polycrystal, deformed at $\dot{\boldsymbol{\varepsilon}}$=$10^{-4}$ s^{-1} and T=1650°C, to $\boldsymbol{\varepsilon} = 0.15$.

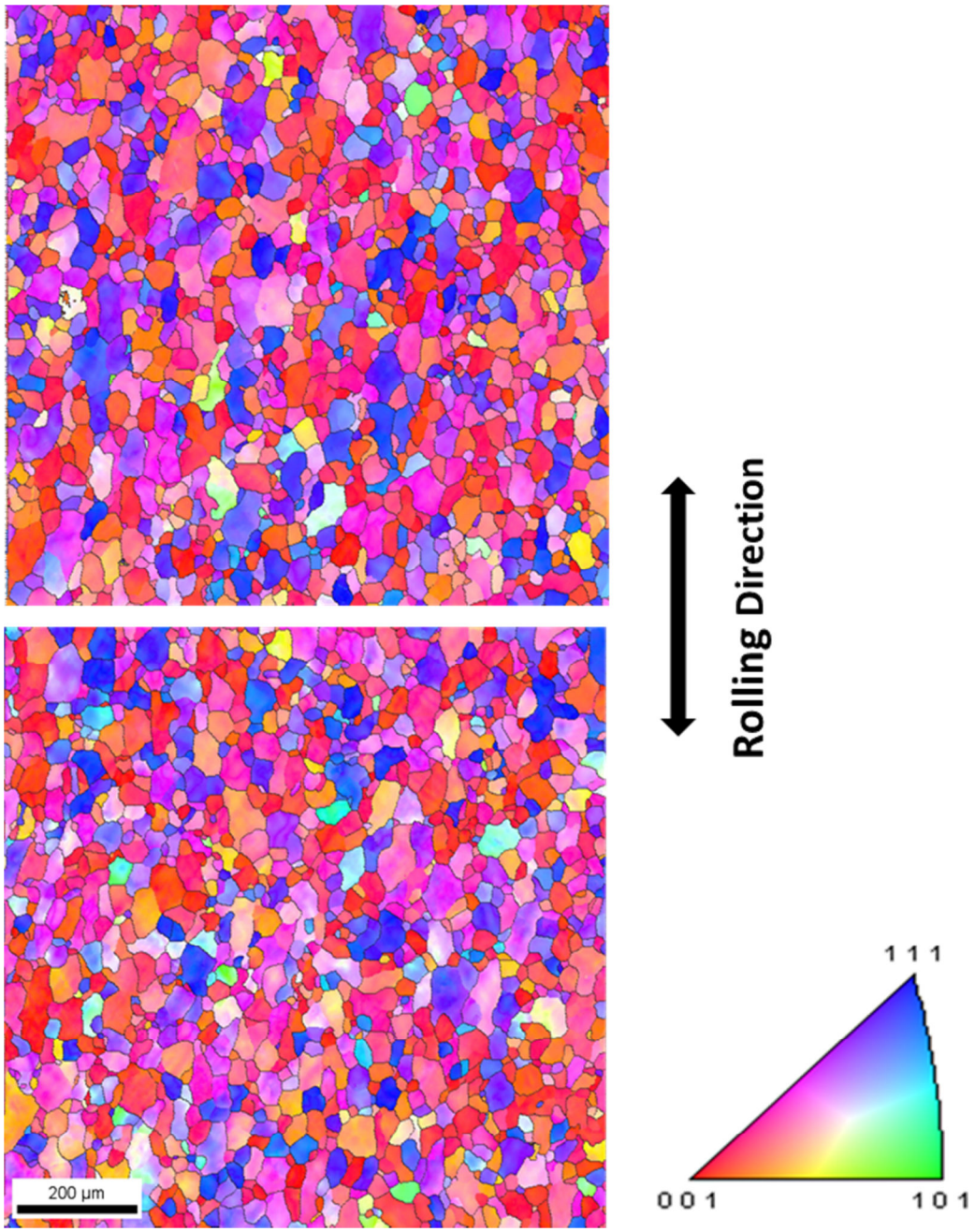

Figure 6-11: Electron Backscatter Diffraction of deformed polycrystal, deformed at $\dot{\varepsilon}=10^{-4}$ s^{-1} and T=1650°C, to $\varepsilon = 0.15$.

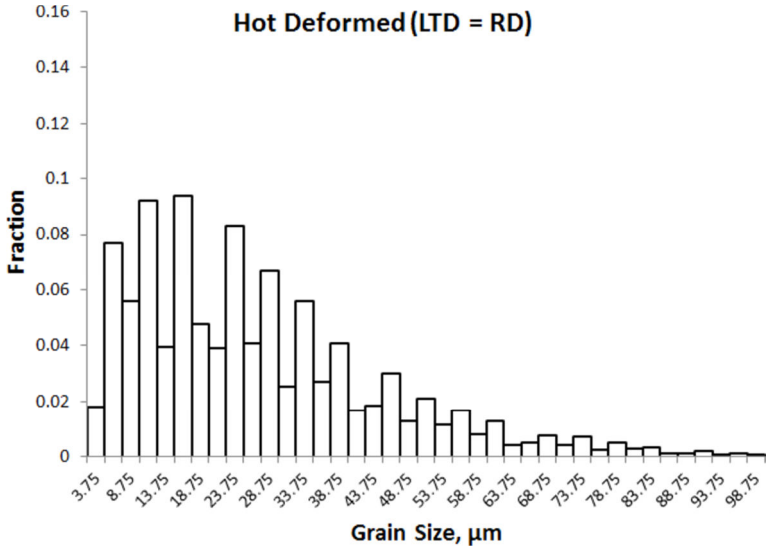

(a)

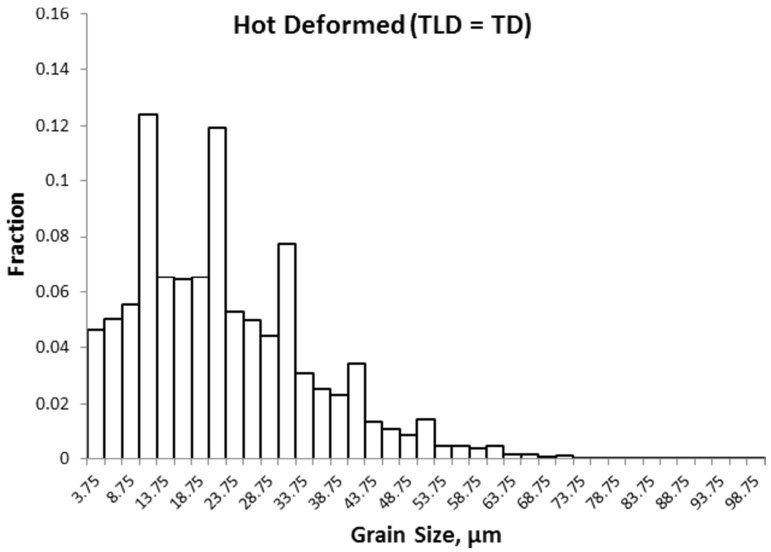

(b)

Figure 6-12: Grain size distribution in (a) long tranverse direction (LTD || RD) and (b) tensile loading direction (TLD || TD) from EBSD in the hot deformed polycrystal of PM-B at $\dot{\boldsymbol{\varepsilon}}=10^{-4}$ s^{-1} and T=1650°C, to $\boldsymbol{\varepsilon} = 0.15$.

The hot deformed grains were more equiaxed than the statically annealed grains. Among the grain sizes obtained from optical photomicrographs, the hot deformed TLD grain sizes, d_{TLD} = 24 µm and d_{TLD} = 22 µm, were slightly larger than the static annealed

TD grain size, d_{TD} = 21 μm. Meanwhile, the hot deformed LTD grain sizes, both d_{TLD} = 22 μm, were smaller than the static annealed RD grain size, d_{RD} = 28 μm. The same trend held for the grain sizes obtained from EBSD, although it was not as pronounced, where d_{TLD} = 22 μm was greater than d_{TD} = 20 μm and d_{LTD} = 27 μm was less than d_{RD} = 30 μm. Grains were originally elongated in the LTD. As straining occurred in the TLD, the grain shape became more equiaxed simply because of the geometry of deformation.

6.3.2 SUBSTRUCTURE

Substructure developed during creep of the polycrystalline material. Figure 6-13 compares EBSD inverse pole figure maps from the statically-recrystallized and hot-deformed microstructures. Orientation gradients within the grain interiors of the hot deformed EBSD photomicrograph indicate substructure development.

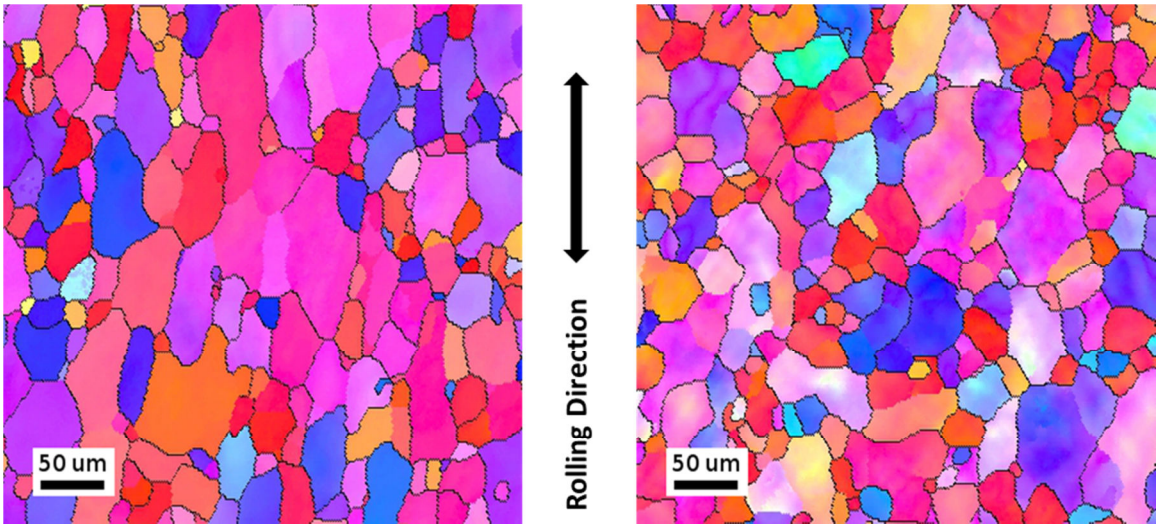

Figure 6-13: Comparison between EBSD of statically annealed (left) and hot deformed (right) PM-B microstructures. The hot deformed microstructure has evidence of substructure formation. Polycrystal hotdeformed at $\dot{\boldsymbol{\varepsilon}}$=$10^{-4}$ s^{-1} and T=1650°C, to $\boldsymbol{\varepsilon}$ = 0.15.

6.3.3 TEXTURE

Uniaxial tensile deformation of bcc metals typically leads to a $\langle 110 \rangle \parallel \langle TLD \rangle$ fiber texture [36, p.192]. The Taylor model [34] predicts rotation toward $\langle 110 \rangle$ for any initial tensile loading direction [52, p.40-43, 53, p.408]. Pole figures and inverse pole figures of the hot deformed and primary recrystallization microstructures of PM-B are provided in Figures 6-14 and 6-15, respectively. The hot deformation texture was obtained from the gauge microstructure of a tensile specimen through EBSD. The test was conducted at 1650ºC and 10^{-4} s^{-1} and halted at ε_{CR} = 0.15 after a DAGG grain had initiated elsewhere in the microstructure.

The hot deformation texture did not evolve significantly from the primary recrystallization texture. As shown in Figure 6-14, the dominant texture components remained, although slightly weakened. However, evolution of texture along the TLD is noted in the inverse pole figures of Figure 6-15 by some rotation of the $\langle 101 \rangle$ toward the tensile direction. In the short transverse direction, there was rotation rotation away from $\langle 001 \rangle$ and $\langle 111 \rangle$. In the long transverse direction, there was some grain rotation toward directions between $\langle 001 \rangle$ and $\langle 101 \rangle$.

The minimal texture evolution during hot deformation is not surprising. This is because the test was halted at a small strain of ε_{CR} = 0.15. DAGG initiation occurs at even smaller critical strains at higher temperatures (ε_{CR} = 0.02 at 1800ºC, see Table 6-2). Initiation at such a small strain of 0.02 allows almost no texture evolution during deformation. Thus, DAGG initiation cannot be initiated by evolution of a particular texture component during deformation. A mechanism similar to rotation recrystallization (see Section 2.3.3) is unlikely to be the source of DAGG initiation.

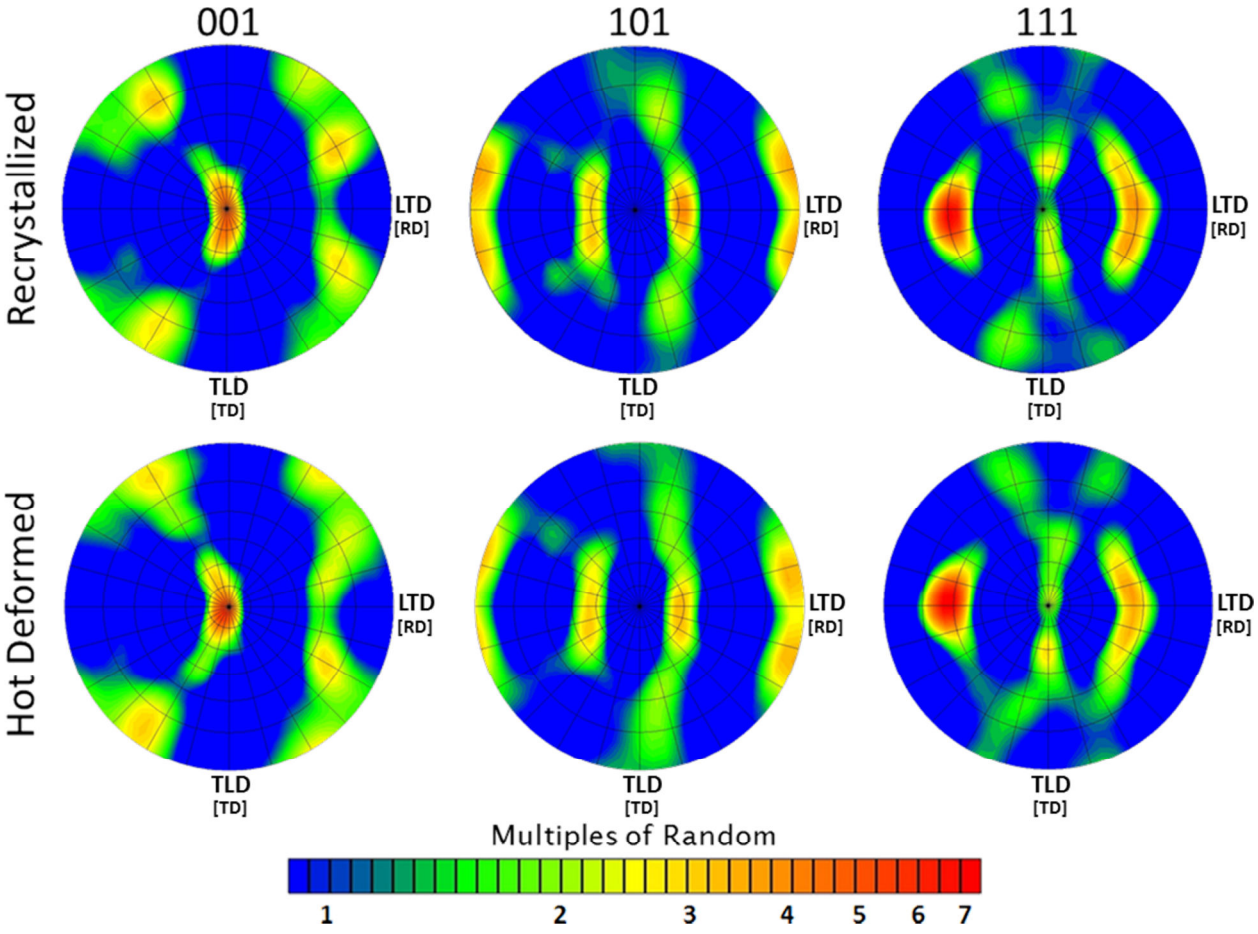

Figure 6-14: Comparison between pole figures from the PM-B recrystallization texture and hot-deformed texture ($10^{-4}s^{-1}$ and $\varepsilon = 0.15$) for a test at 1650°C from EBSD datasets. Figures are plotted with respect to the specimen axes. Note that the recrystallized pole figures presented above are rotated 90º from the same pole figures presented in Figure 5-3. This is because the PM-B specimens are in the T orientation (See Figure 4-2), that is, the tensile loading direction (TLD) of the specimen is rotated 90º from the rolling direction (RD) of the sheet.

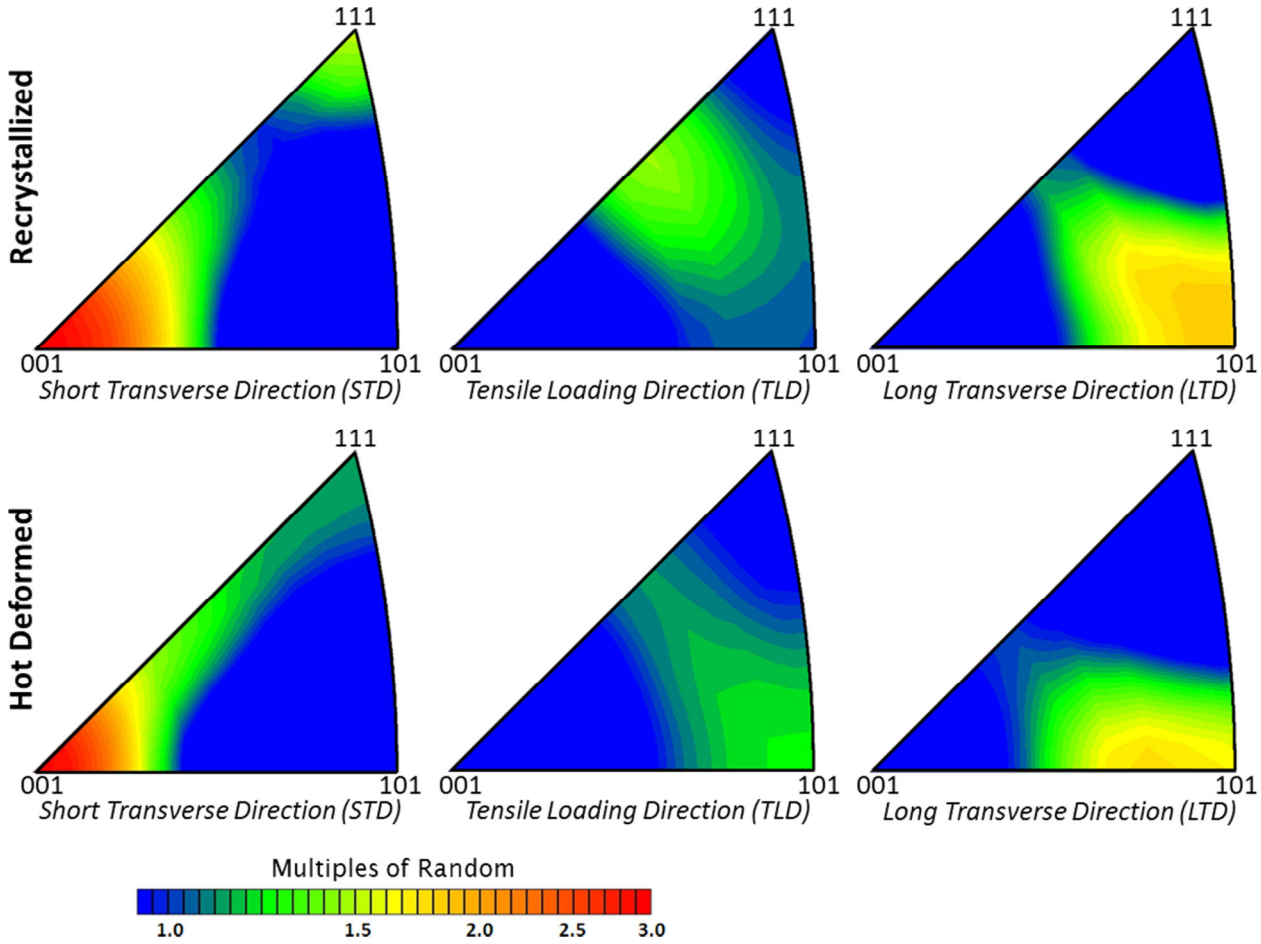

Figure 6-15: Comparison between inverse pole figures from the recrystallization texture and hot-deformed ($10^{-4}s^{-1}$ and $\varepsilon = 0.15$) texture for 1650°C. Figures from EBSD datasets.

6.4 DAGG Orientations

DAGG grains have a preferred crystallographic orientation with respect to the specimen axes. Cubic crystal structures are in the $m\bar{3}m$ (O_h) point group, with 24 symmetry elements. The tensile specimen geometry (Figure 4-1) has a geometric symmetry that can be classified in the orthorhombic mmm (D_{2h}) point group, with 4 symmetry elements. These symmetry classifications dictate how crystal directions are represented on specimen axes (i.e. a pole figure) or specimen directions are represented on crystal axes (i.e. an inverse pole figure) to describe the orientation of a DAGG grain. The orientations of numerous DAGG grains were indexed with Laue X-ray back diffraction. These include 8 DAGG grains in the AM material, 11 DAGG grains in the PM-A material, and 23 DAGG grains in the PM-B material. These orientations are represented on the pole figures in Figure 6-16 and the inverse pole figures in Figure 6-17. In Figure 6-16, the full pole figures were reduced to quarter pole figures by using the mmm specimen geometric symmetry. In Figure 6-17, the full inverse pole figures were reduced to standard triangles by using the $m\bar{3}m$ cubic crystal symmetry.

In the AM and PM-B materials, the TLD of the specimen is along the TD of the sheet. In the PM-A material, the TLD of the specimen is along the RD of the sheet. Therefore, a new notation is introduced $\{STD\}\langle\langle TLD\rangle\rangle$ to describe crystallographic orientations in the specimen reference frame. Recall that planes and directions $\{ND\}\langle RD\rangle$ usually describe texture components in a rolled sheet (see Section 5.2). The orientation preference in all materials studied can be generally described as derivative from a $\langle 110\rangle$ fiber texture with components that span $\{001\}\langle\langle 110\rangle\rangle$ to $\{111\}\langle\langle 1\bar{1}0\rangle\rangle$. Note that this partial fiber texture is analogous to an α-fiber rolling texture; refer to Figure 5-1 for

representations of the different texture components in a ⟨110⟩ fiber on a full pole figure. Within the ⟨110⟩ fiber, each material exhibits a preference for a different orientation:

(1) The AM grains are clustered around the $\{111\}\langle\langle 1\bar{1}0\rangle\rangle$ orientation.

(2) The PM-A grains are clustered around the $\{112\}\langle\langle 1\bar{1}0\rangle\rangle$ orientation.

(3) The PM-B grains are clustered around the $\{001\}\langle\langle 110\rangle\rangle$ orientation.

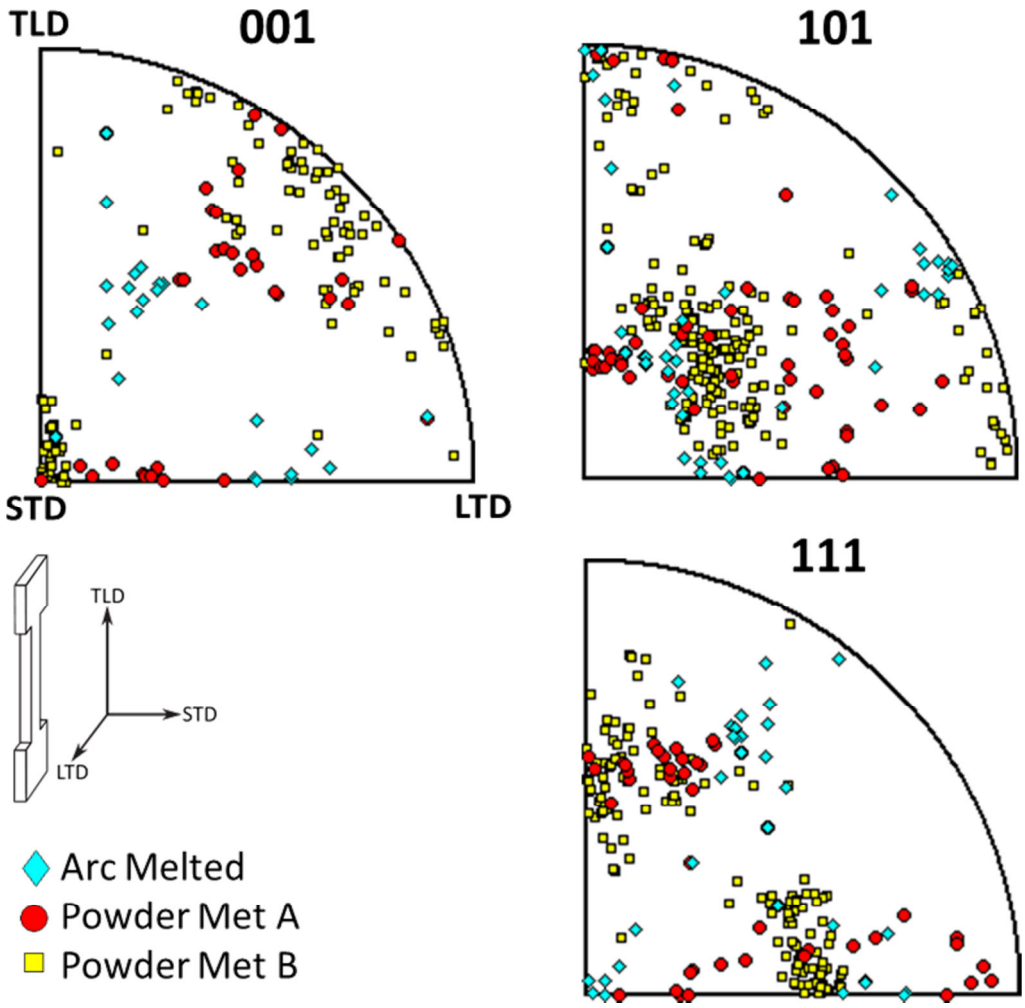

Figure 6-16: Pole orientations of individual DAGG grains from multiple specimens, represented on pole figures. Note that these are equivalent to full pole figures because of the orthorhombic symmetry of the tensile specimen (mmm).

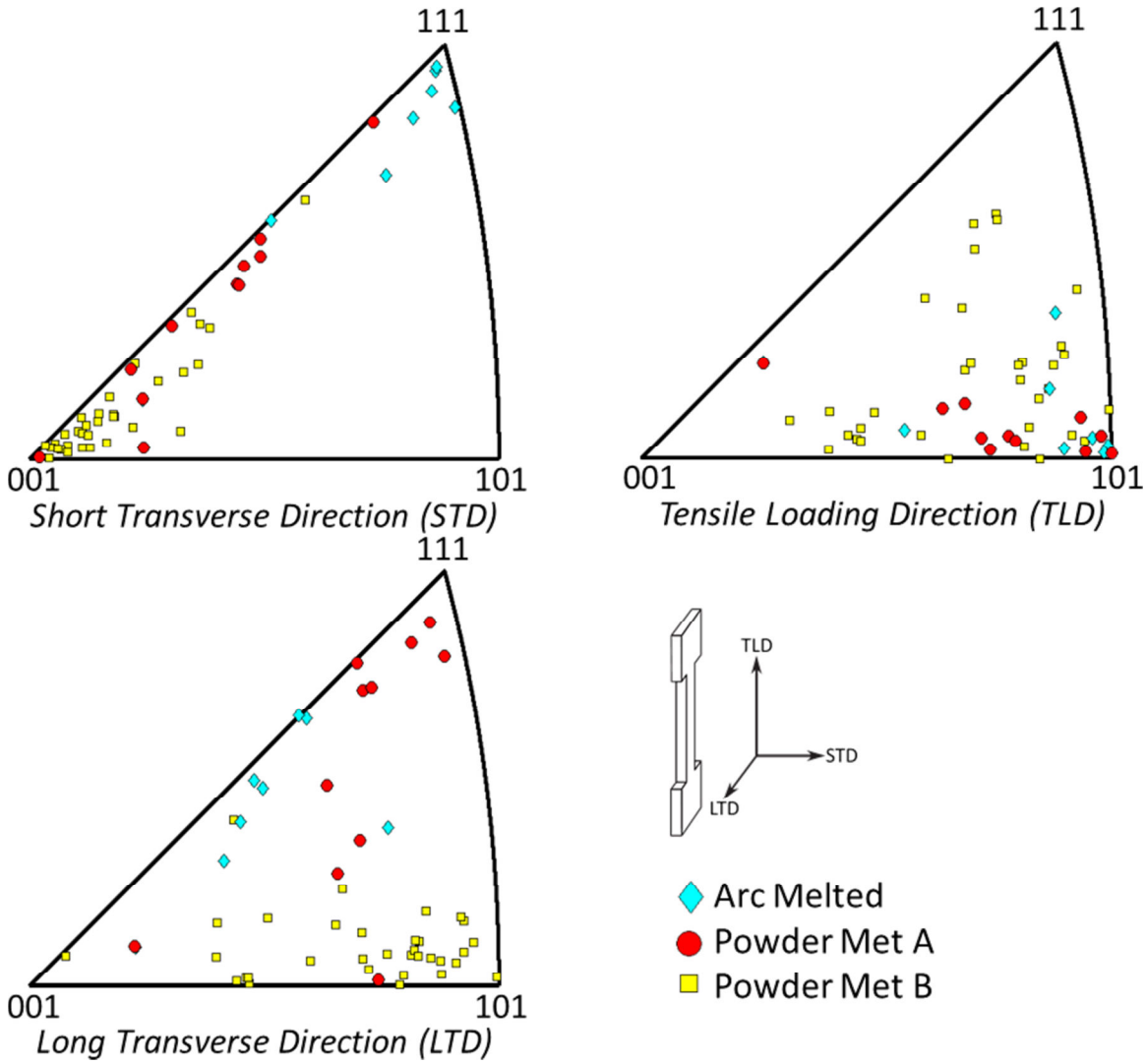

Figure 6-17: Orientations of individual DAGG grains from multiple specimens, represented on inverse pole figures.

These crystal orientations are represented in Figure 6-18. Refer to the inverse pole figures of Figure 6-17 for the following discussion. Although the TLDs of specimens from all the materials show strong preference for alignment with ⟨101⟩ orientations, this clustering is weak in the PM-B material and allows for significant deviation (~25º) from ⟨101⟩. DAGG grain orientations from ⟨001⟩ to ⟨111⟩ align with the STD: ⟨112⟩ to ⟨111⟩ in the AM material, ⟨001⟩ to ⟨112⟩ in the PM-A material, and ⟨001⟩ to ⟨113⟩ in the PM-

B material. Although it shows the greatest scatter in orientations, the LTD is somewhat clustered around different directions for each material: ⟨112⟩ in the AM material, ⟨111⟩ in the PM-A material, and ⟨101⟩ in the PM-B material.

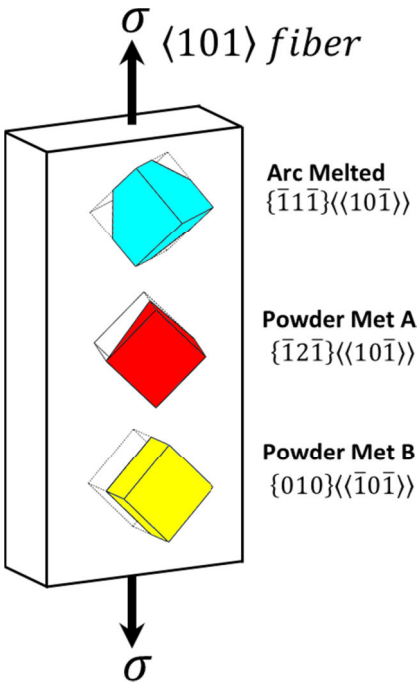

Figure 6-18: Schematic of the average crystallographic orientation for AM, PM-A, and PM-B materials.

Potential causes of DAGG grain orientation preferences include: (1) DAGG grain adoption of orientations from the hot deformed texture, or simply the primary recrystallization texture, (2) DAGG grain orientation selected from among energy difference between distinct (hkl) cyrstallographic free surfaces in molybdenum, and (3) the crystallographic nature of slip influencing the choice of DAGG grain orientation. The following sections discuss each of these potential causes of the preferred DAGG grain orientations.

6.4.1 TEXTURE

In Section 6.3.3, it was observed that significant texture evolution does not occur prior to DAGG initiation in the PM-B material. Therefore, the primary recrystallization

textures for AM and PM-A are used to approximate their hot deformation textures. Inverse pole figures of the AM and PM-A primary recrystallization textures and the PM-B hot deformation texture are shown in Figure 6-19. Individual DAGG grain orientations are superimposed on top of these textures for comparison. Inverse pole figures of recrystallization texture are not available for the tensile loading direction (TLD) and long transverse direction (LTD) of the AM and PM-A materials.

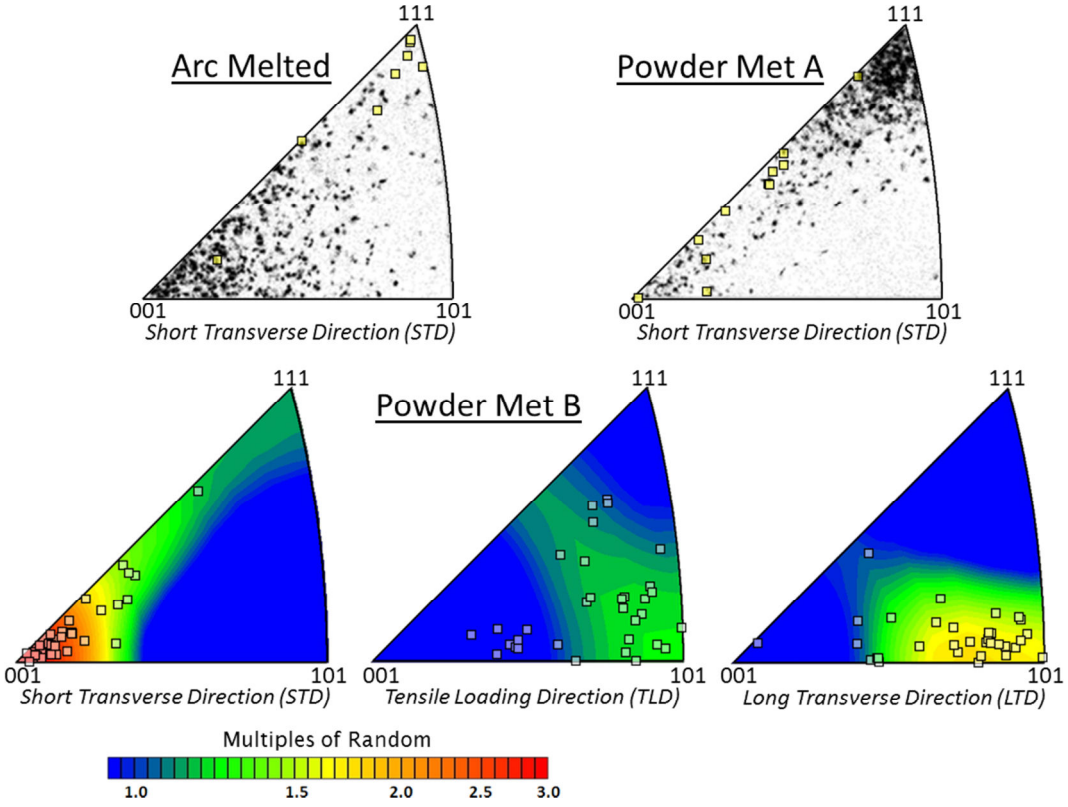

Figure 6-19: The 001, 101, and 111 inverse pole figures for the recrystallization textures of the AM, PM-A, and PM-B materials. AM and PM-A inverse pole figures reproduced from Ciulik [3].

DAGG grains are not randomly selected from the hot deformed microstructure. DAGG grains prefer a ⟨101⟩ || TLD in all the materials studied, but grains with a ⟨101⟩ ||

TLD are not generally the most prevalent in the hot deformed polycrystal. In the PM-B material, DAGG grains have a strong orientation preference for a ⟨101⟩ || TLD orientation, even though these grains are selected from a relatively random TLD orientation distribution. In Figure 6-19, the PM-B hot deformation texture in the TLD is at most 1.2 multiples above random. However, DAGG grains exhibited a strong preference for orientations with a TLD near ⟨101⟩. The complete absence of DAGG orientations with a TLD between ⟨001⟩ and ⟨111⟩ clearly indicates the strength of preference for a ⟨101⟩ || TLD. Inverse pole figures are not available for the AM and PM-A textures in the TLD. However, texture information can still be obtained from the full pole figures of Figure 6-20. The AM texture has components with ⟨001⟩ and ⟨101⟩ in the TLD, although they appear relatively faint. The PM-A texture has a strong component with ⟨101⟩ in the TLD. Accordingly, DAGG grains with a ⟨101⟩ || TLD are produced regardless of strong or weak texture components with a ⟨101⟩ || TLD. Therefore, the strong preference for DAGG grains with a ⟨101⟩ || TLD is independent of the hot deformation texture.

DAGG grains prefer different STD orientations in each of the materials studied. In the PM-B material, grains with an STD corresponding to a *majority* texture component are selected for DAGG, as shown in Figure 6-19. Both the PM-B DAGG orientations and PM-B dominant texture components have an STD near ⟨001⟩. On the other hand, in the AM material and PM-A materials, grains with an STD corresponding to a *minority* texture component are selected for DAGG. The AM DAGG orientations have an STD between ⟨112⟩ and ⟨111⟩, whereas the dominant AM texture components have an STD near ⟨001⟩. The PM-A DAGG orientations have an STD between ⟨001⟩ and ⟨113⟩, whereas the dominant PM-A texture components have an STD near ⟨111⟩.

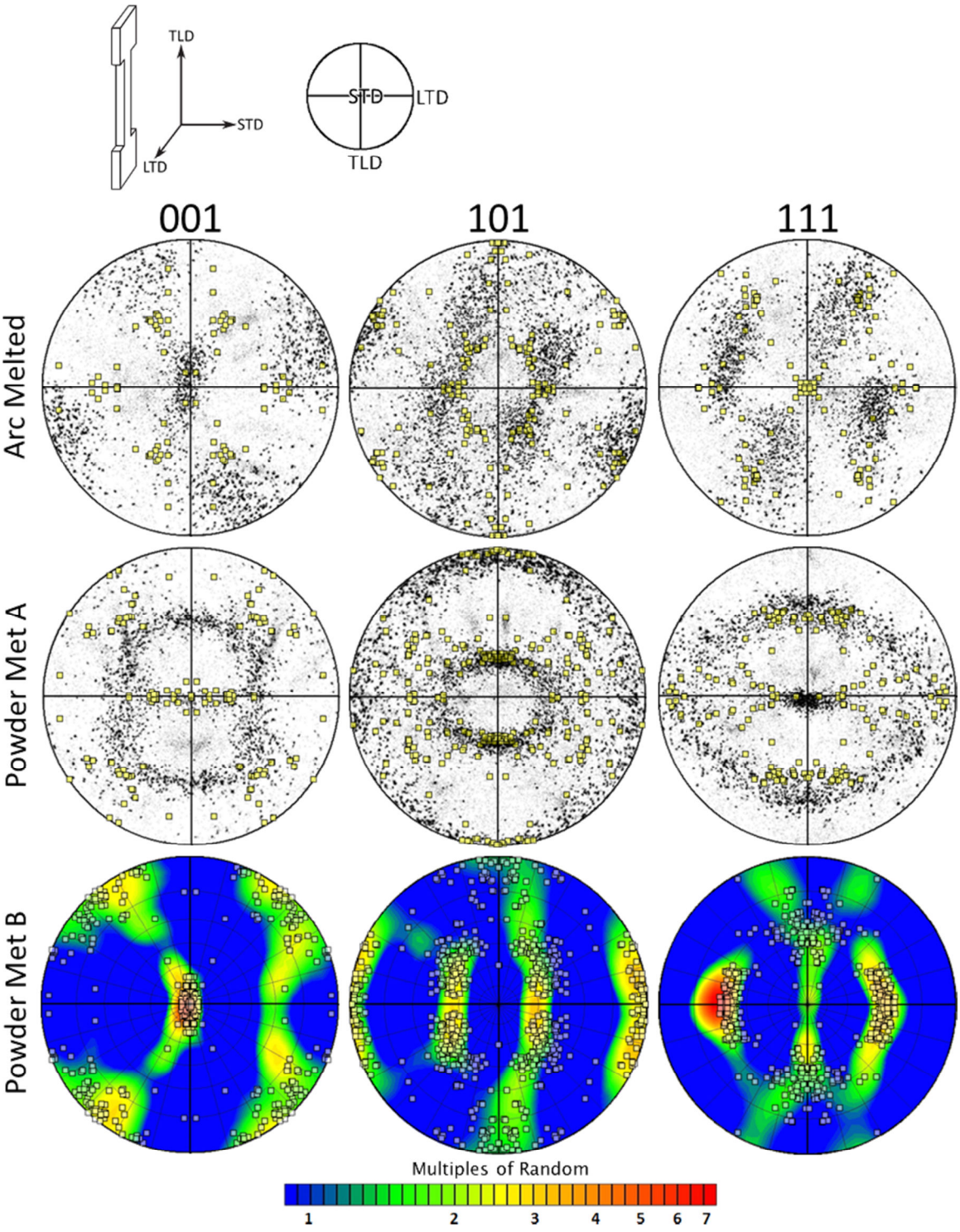

Figure 6-20: Individual DAGG grain orientations overlain on 001, 101, and 111 pole figures for the recrystallization textures of AM, PM-A, and PM-B from Figure 5-3.

DAGG grains also prefer different LTD orientations in the each of the materials studied. In the PM-B material, grains with an LTD corresponding to a *majority* texture component are selected for DAGG, as shown in Figure 6-19. Both the PM-B DAGG orientations and PM-B dominant texture components have an LTD near directions between ⟨101⟩ and ⟨102⟩. Inverse pole figures are not available for the AM and PM-A textures in the LTD. Therefore, as with the TLD, the full pole figures of Figure 6-20 are again referenced for LTD texture information. The AM texture has components with ⟨001⟩ and ⟨101⟩ in the LTD. AM DAGG grains have a preference for orientations with a ⟨112⟩ LTD. Because a 112 pole figure is not available for the AM material, it cannot be determined if AM DAGG grains are selected from a strong texture component. The PM-A texture has components with ⟨101⟩ and ⟨111⟩ in the LTD. PM-A DAGG grains have a preference for orientations with a ⟨111⟩ LTD, and therefore PM-A DAGG grains are selected from texture component which is, at least, moderately intense.

The orientation preference for DAGG grains from a ⟨101⟩ fiber is independent of material texture. Within the ⟨101⟩ fiber, different DAGG grains were selected in each material. In the PM-B material, DAGG grains were selected from majority texture components. In the AM and PM-A material, DAGG grains were selected from minority texture components. Therefore, the hot deformation texture was not observed to have a consistent effect on the orientations of DAGG grains.

6.4.2 SURFACE ENERGY

If DAGG initiates from grains on the free surface of the specimen, then the relative free surface energies of different crystallographic planes could play an important role in the DAGG phenomenon. The face of the tensile specimens contains the largest surface area, and the short transverse direction (STD) is along that face normal. The

crystallographic directions of DAGG grains are tightly clustered between ⟨001⟩ and ⟨111⟩ in the STD inverse pole figure (Figure 6-17). If the free surface energies of (001) and (111) planes, γ_{001} and γ_{111}, are substantially smaller than the free surface energy of (101) planes, γ_{101}, then interfacial free energy differences could explain the preferred DAGG grain orientations in the STD. However, the values for these surface energies calculated by density functional theory are similar: γ_{001} = 3.84 J/m^2, γ_{111} = 3.74 J/m^2, and γ_{101} = 3.45 J/m^2 [54]. Therefore, the free surface energy is unlikely to have a significant effect on DAGG grain orientation.

6.4.3 PLASTIC STRAIN: SINGLE SLIP

A DAGG grain must have the ability to easily accumulate plastic strain. The stress drop associated with DAGG clearly indicates that resistance to flow decreases upon transition from polycrystalline to monocrystalline forms. It is logical to expect that any grain selected to be abnormal and grow through the DAGG process be one favorably oriented for slip. For a review of strain and slip, see Section 3.2.

Consider slip in a single crystal. Crystals loaded along a ⟨111⟩ tensile axis are resistant to plastic straining, while the ⟨100⟩ and ⟨110⟩ axes are softer orientations in a bcc metal. This is readily apparent from the Schmid factors of these orientations: 0.272 for ⟨111⟩ and 0.408 for both ⟨100⟩ and ⟨110⟩. Figure 6-21 plots lines of constant Schmid factor over tensile loading direction on four inverse-pole-figures. Each figure considers a different set of slip planes: (a) {110}, (b) {112}, (c) {123}, and (d) all slip planes combined in an equally weighted average (i.e. τ_{CRSS} is assumed to be equal for all slip system families, see Equation 3-5). This follows a similar analysis by Hosford [52, p.34-42]. The trend in all of these figures is the same; orientations loaded away from ⟨111⟩ are less resistant to slip and more prone to accumulate plastic strain. As such, we expect the

orientations of DAGG grains to never have {111} planes orthogonal to the tensile axis. Compare the DAGG grain orientations of Figure 6-17 with the Schmid factor contour maps of Figure 6-21. There is an absence of orientations loaded along tensile loading directions between ⟨001⟩ and ⟨111⟩. This absence of orientations includes the plastically hard ⟨111⟩ tensile direction. Therefore, DAGG grains possess orientations which have a low resistance to slip. However, this Schmid factor analysis does not explain the absence of DAGG orientations in the plastically softer directions between ⟨001⟩ and ⟨112⟩. This analysis only considered single slip. Multiple slip systems are likely active. Therefore, the next section explores deformation from multiple slip systems possessing high Schmid factors.

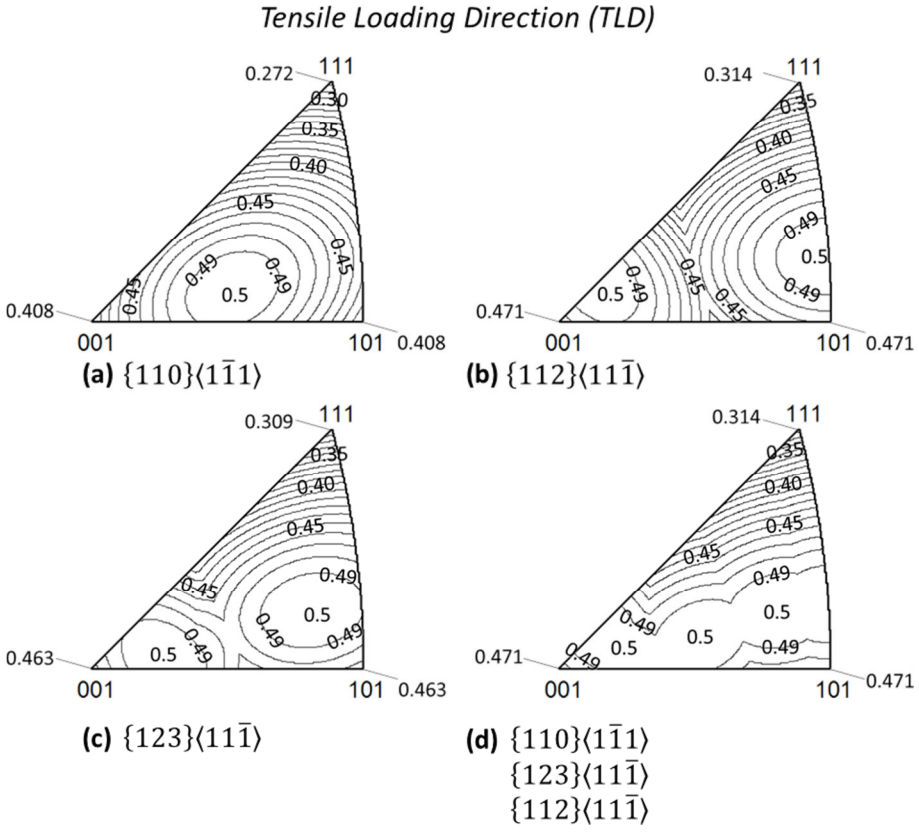

Figure 6-21: Schmid factor values for different tensile loading directions, plotted on inverse pole figures for three different bcc slip systems and all slip systems combined in an equally weighted average.

6.4.4 PLASTIC STRAIN: MULTIPLE SLIP AND PLANE STRAIN

Plane strain deformation is simultaneous extension and compression in an orthogonal pair of directions, respectively, with zero strain in the third orthogonal direction:

$$\underline{\Delta\varepsilon} = \begin{bmatrix} -d & 0 & 0 \\ 0 & 0 & 0 \\ 0 & 0 & d \end{bmatrix} \tag{6-6}$$

where $\underline{\Delta\varepsilon}$ is an incremental addition to the strain tensor, $-d$ is the compression, and d is the extension.

DAGG grains may favor plane strain deformation during uniaxial tension because of geometric constraints illustrated in Fig. 6-22. Once a DAGG grain grows across the width of a specimen, further straining in the specimen occurs in plane strain deformation. The logic behind this statement is as follows. Deformation primarily occurs in the DAGG grain due to its lower resistance to plastic flow. As the DAGG grain elongates, compatibility must be maintained at the interface between the polycrystal and DAGG grain. Because the free surface of the DAGG grain is not constrained, compatibility during elongation is most easily obtained through a reduction in thickness. This deformation condition describes plane strain ($\varepsilon_{TLD} = -\varepsilon_{STD}$; $\varepsilon_{LTD} = 0$) and is pictured schematically in Figure 6-22 for (a) a DAGG grain which has grown across the width and (b) a DAGG grain which has grown through the thickness of a specimen. In (a), the DAGG grain and polycrystalline microstructure deform in parallel. In (b), the DAGG grain and polycrystalline microstructure deform in series. In either case, plane strain deformation is expected in the DAGG grain from compatibility constraints.

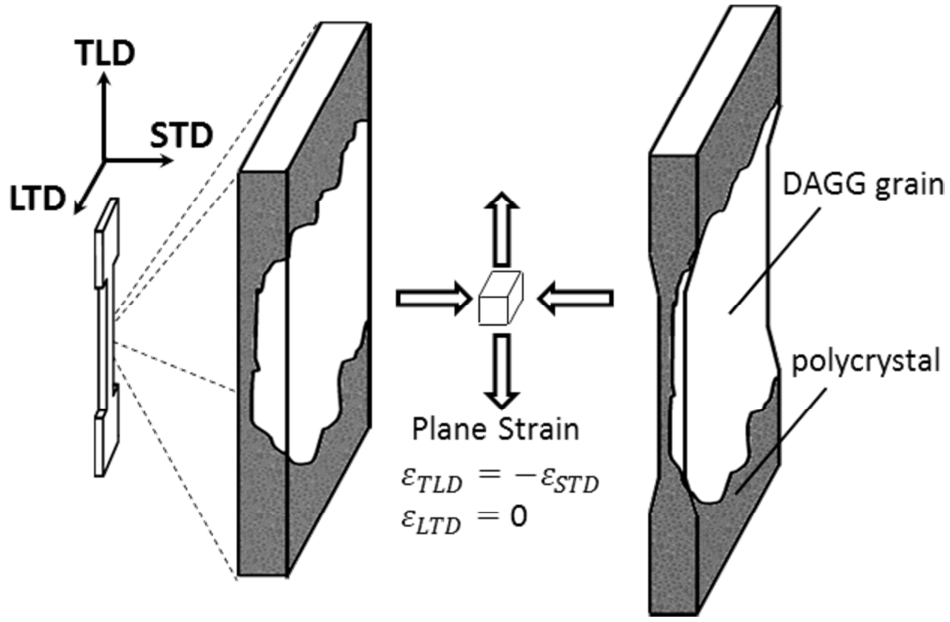

(a) Plane strain deformation after growth of DAGG grain *across the gauge width*. DAGG grain and polycrystalline microstructure deform in parallel. Harder polycrystalline microstructure limits deformation of DAGG grain.

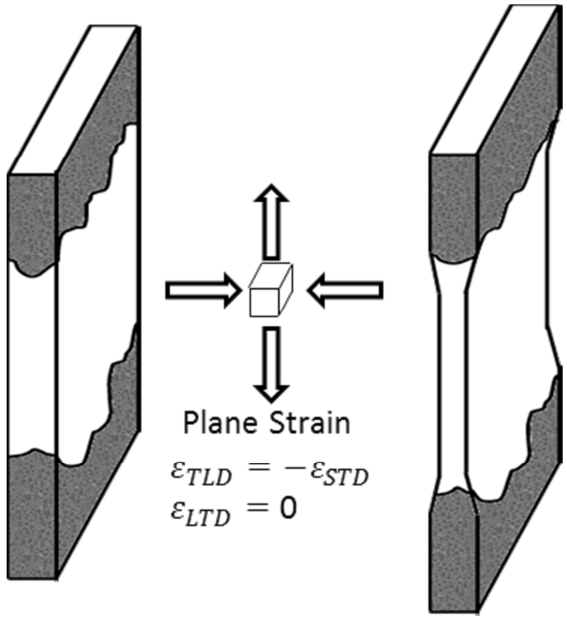

(b) Plane strain deformation after growth of DAGG grain *through the gauge thickness*. DAGG grain and polycrystalline microstructure deform in series. Harder polycrystalline microstructure does not deform, and constrains DAGG grain deformation only at its ends. Plane strain deformation of the DAGG grain is encouraged by these ends constraints.

Figure 6-22: Schematics of plane strain deformation in a DAGG grain after (a) growth across the width and (b) growth through the thickness.

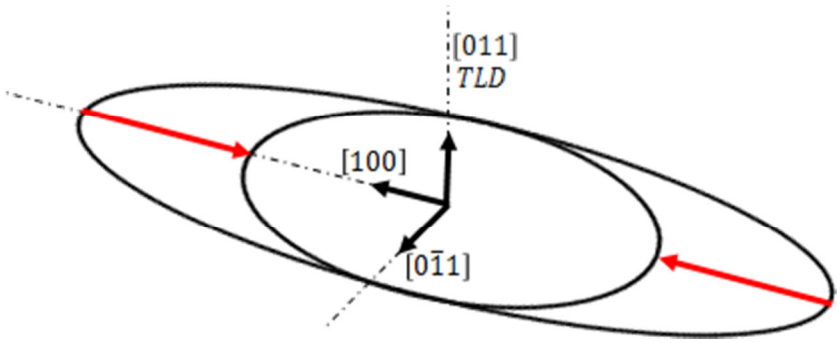

Figure 6-23: Shape change in the cross section of a bcc crystal loaded along [011] in uniaxial tension. Plane strain deformation results: extension d occurs along [011], compression $-d$ occurs along [100], and zero strain d occurs along [0$\bar{1}$1].

In body-centered-cubic (bcc) metals, a grain with a ⟨110⟩ tensile loading direction (TLD) intrinsically favors plane strain deformation [36, p. 194-195, 55, p. 157]. Appendix B considers a bcc crystal loaded along [011] in uniaxial tension. Plane strain deformation results from this loading, extension d occurs along [011], compression $-d$ occurs along [100], and zero strain occurs along [0$\bar{1}$1], as shown schematically in Figure 6-23. DAGG grains oriented with ⟨110⟩ || TLD and ⟨100⟩ || STD may deform through plane strain by slip on only four independent slip systems, as is mathematically demonstrated through the calculation supplied in Appendix B. Therefore, PM-B DAGG grains and some PM-A DAGG grains, which exhibit a ⟨100⟩ || STD, likely deform through plane strain by this process. However, all other orientations rotated about the ⟨110⟩ || TLD do not fulfill plane strain when these four slip systems alone are considered. Therefore, additional slip systems would be necessary to achieve plane strain in the AM DAGG grains and some PM-A DAGG grains, which exhibit a STD between ⟨100⟩ and ⟨111⟩. The expected ease of pencil glide at these elevated temperatures is consistent with the activation of such additional slip systems. Thus, the need to achieve plane strain deformation may be one contributing factor to the selection of DAGG grain orientations.

6.5 Chapter Summary

(1) DAGG occurs in several molybdenum materials with different microstructures. The presence of DAGG is insensitive to a specific texture or microstructure. Prior to DAGG initiation, molybdenum exhibits power-law creep behavior typical of a polycrystalline metal.

(2) The minimum temperature for DAGG in PM-B is between 1450 ºC and 1550 ºC. This is in good agreement with the minimum temperature for PM-A, which is between 1440 ºC and 1540 ºC.

(3) The critical strain for DAGG initiation decreases with increasing temperature:

Temperature	Average Critical Strain, ε_{CR}
1550 ºC	0.25
1450 ºC	0.16
1800 ºC	0.02

(4) For the same temperature and strain-rate, the critical strain varies significantly (±40% for a 95 percent confidence interval) between multiple tests.

(5) Since the tensile direction was perpendicular to the sheet rolling direction in PM-B, elongated grains from the primary recrystallized microstructure become more equiaxed during hot deformation.

(6) Substructure developed during creep of the polycrystalline microstructure prior to DAGG. This substructure is retained during unloading and cool down.

(7) Minimal texture development occurred in the PM-B material at a true plastic strain of 0.15 after tensile deformation at 1650 ºC and $10^{-4}s^{-1}$.

(8) Preferred orientations of DAGG grains come from a $\langle 101 \rangle$ fiber texture with a short transverse direction which spans $\langle 010 \rangle$ to $\langle \bar{1}1\bar{1} \rangle$. Each material exhibited a different preferred short transverse direction:

$\{\bar{1}1\bar{1}\}\langle\langle 10\bar{1}\rangle\rangle$ AM DAGG grains

$\{\bar{1}2\bar{1}\}\langle\langle 10\bar{1}\rangle\rangle$ PM-A DAGG grains

$\{010\}\langle\langle \bar{1}0\bar{1}\rangle\rangle$ PM-B DAGG grains

(9) The preferred DAGG orientations are not consistently from a minority or majority component of the primary recrystallization texture.

(10) $\{010\}\langle\langle \bar{1}0\bar{1}\rangle\rangle$ PM-B DAGG grains are preferred orientations. These orientations intrinsically fulfill the plane strain deformation condition in the specimen, once a DAGG grain has grown across the gauge width.

7 DYNAMIC ABNORMAL GRAIN GROWTH

The growth of DAGG grains was studied from the halt specimens described in Chapter 6. This chapter examines the shape of arrested DAGG grains in the halt specimens and reports on the boundary migration rates of DAGG and SAGG.

7.1 DAGG Grain Morphology

Approximately half of DAGG grains observed did not grow through the thickness of the halt specimens. That is, these grains were restricted to only one surface, front or back, of the sheet material and are hereafter referred to as *surface grains*. The other half of DAGG grains did grow through the sheet thickness of the halt specimen and are hereafter referred to as *thickness grains*. Examples of each type of grain are shown in Figure 7-1: (a) a surface grain and (b) a thickness grain. In this figure, the front and back faces of two PM-B halt specimens tested at $\dot{\varepsilon}=10^{-4}$ s^{-1} and T=1650°C were macroetched. Note that in (a) the DAGG grain is visible on the front of the specimen but not the back, while in (b) the DAGG grain is visible on both sides. Cross sections were then taken of the DAGG grain: the A-A cross sections are optical photomicrographs normal to the LTD, and the B-B cross sections are optical photomicrographs normal to the TLD. These photomicrographs clearly show that the DAGG grain in (a) is a surface grain, and the DAGG grain in (b) is a thickness grain.

The prevalence of surface grains produced in DAGG halt experiments indicates that surface growth of the DAGG grain is preferred. Indeed, the surface grain in (a) has a large TLD/STD aspect ratio of 23:1; this was measured after the removal of 200 μm from the thickness by polishing during metallographic preparation. This large aspect ratio suggests that DAGG grain growth is either strongly promoted in the TLD and/or strongly retarded in the STD in this specimen. A preference for surface growth is demonstrated

even in the thickness grain in Figure 7-1(b). This grain has an "hourglass" shape, as is shown in the A-A view of Figure 7-1(b); long arms of the unconsumed polycrystal extend into the DAGG grain at the midplane of the sheet thickness. This indicates that dynamic abnormal growth occurs more readily at the surface, and the interior of the thickness grain must be "dragged" along.

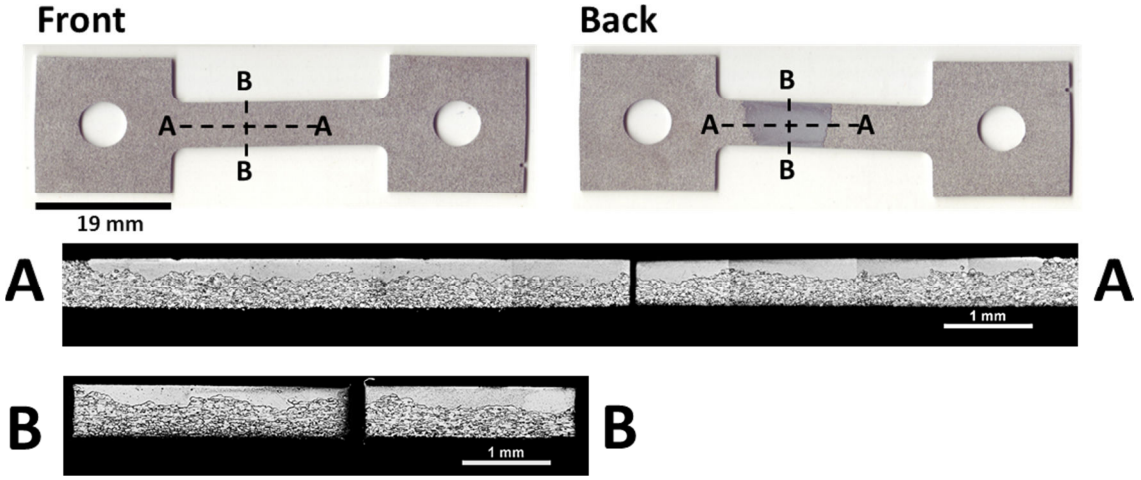

(a) surface grain

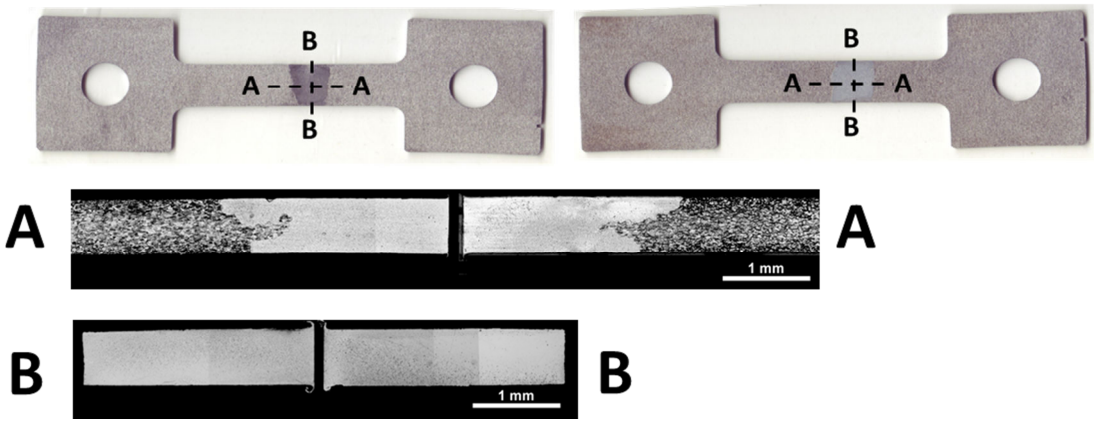

(b) thickness grain

Figure 7-1: Two different halt tests of PM-B tested at $\dot{\varepsilon}=10^{-4}$ s^{-1} and T=1650°. The front and back of the specimens are shown, along with cross sections A-A (LTD normal) and B-B (TLD normal): (a) surface grain and (b) thickness grain. The front surface is upward in cross sections A-A and B-B.

One possible explanation for the preferred surface growth is a through-thickness texture gradient, which has been reported in the following bcc refractory metals: 4 to 6 mm tantalum plate [56, 57], 0.7 mm niobium sheet [58], and Nb-V sheet [59]. The texture in these materials has a gradient from ⟨001⟩ || ND near the surface to ⟨111⟩ || ND near the centerline, although it is not always pronounced [60]. If such a gradient exists in the 0.76 mm PM-B sheet, grains with a ⟨111⟩ || ND on the sheet centerline may be more difficult to consume. Data are not available to test this hypothesis for the Mo materials in this investigation, and this hypothesis must be left to future investigations.

Other possible explanations for surface growth during DAGG are now discussed. The preference for growth of DAGG grains along the specimen surface suggests that the free surface may also be important for DAGG initiation. Surface effects are traditionally considered for abnormal grain growth only in thin films. Humphreys lists two mechanisms related to surface effects on abnormal grain growth: (1) normal grain growth inhibition due to thermal grooving and (2) a driving force from the difference in free surface energy of neighboring grains [1, p. 377]. However, both of these mechanisms apply only when the grain sizes are of the order of the sheet thickness. The material studied in the present investigation is not a likely candidate for either mechanism; PM-B has a grain size of approximately 20 μm and a sheet thickness of 762 μm. Therefore, the preference for surface growth in DAGG must result from a distinctly different mechanism or microstructural effect. Potential mechanisms for surface-preferred growth are as follows:

(1) If a grain intersects the free surface, it has fewer neighboring grains on average. The number of triple and quadruple points at its boundaries is reduced. Therefore, the boundaries of surface grains may have a higher mobility.

(2) If the rate of boundary migration during DAGG is enhanced through plastic strain accumulation, the free surface of a surface grain may serve as a source/sink for dislocations. A model of this mechanism will be developed in Chapter 8.

Microstructure away from the specimen surface suggests specific possibilities for the mechanism by which DAGG occurs. The grain-boundary curvatures between the polycrystal and DAGG grain are consistent with a boundary-curvature driving force for boundary migration. The boundaries of normal grains bulge outward into the DAGG grain. Since boundaries move toward their centers of curvature, these shapes indicate consumption of the polycrystalline microstructure by the DAGG grain. Furthermore, these observations suggest that the driving force for boundary migration in DAGG is grain boundary curvature. Grain boundary curvature, the primary driving force for static normal grain growth (SGG) and static abnormal grain growth (SAGG), is related to the reduction in grain boundary area [19].

7.2 DAGG Growth

Once a DAGG grain initiates, it rapidly consumes the entire gauge length of the Mo tensile specimen. As previously noted by Ciulik, the drop in flow stress observed in these tests is associated with the initiation and growth of an abnormal grain in the microstructure. Ciulik halted four different specimens at different points along the flow stress drop in the PM-A material, as seen in Figure 3-1 [5]. Microstructures from these halt tests indicate that the size of the DAGG grain increases as the flow stress drops. Once the drop in flow stress bottoms out (the minimum is reached), one or more DAGG grains occupy the entire gauge length, l_o.

7.2.1 BOUNDARY MIGRATION RATE

The DAGG boundary migration rate, v_{DAGG}, can be estimated by measuring the time required for the flow stress drop, Δt:

$$v_{DAGG} = d/\Delta t \ , \tag{7-1}$$

where d is the distance traveled by a DAGG grain boundary. This distance can vary, depending on where the DAGG grain initiates. If the DAGG grain initiates in the middle of the gauge length, then $d = l_o/2$, but if the initiation occurs at either end of the gauge length, then $d = l_o$. Therefore, the DAGG boundary migration rate is bounded within measureable values as:

$$\frac{l_o}{2\Delta t} \leq v_{DAGG} \leq \frac{l_o}{\Delta t} \ . \tag{7-2}$$

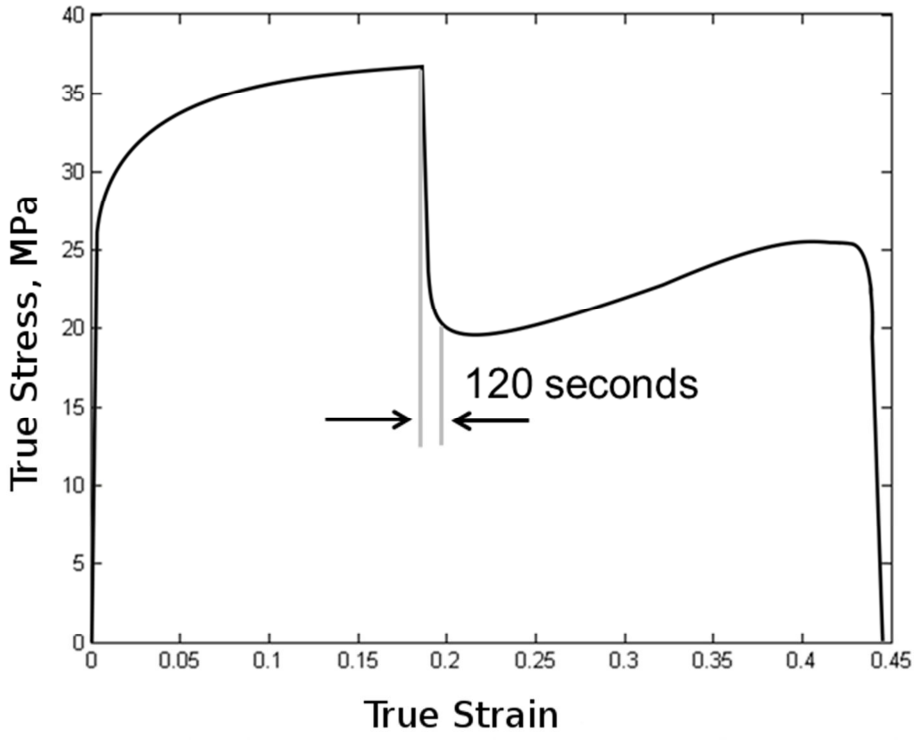

Figure 7-2: Stress-strain curve for strain to failure test of PM-B at $\dot{\varepsilon}$=10^{-4} s^{-1} and T=1650° and the time duration associated with the DAGG drop.

The stress-strain curve of a strain-to-failure test at $\dot{\varepsilon}$=10^{-4} s^{-1} and T=1650°C of PM-B is shown in Figure 7-2. In this test, the DAGG drop occurs over $\Delta t \approx 120$ s, and the gauge length of the specimen is $l_o = 2.54$ cm; therefore the DAGG boundary migration rate is bounded as follows: $0.64 \leq v_{DAGG} \leq 1.28$ cm/min at $\dot{\varepsilon}$=10^{-4} s^{-1} and T=1650°C in the PM-B material. Note that this is much faster than the fastest SAGG boundary migration rates of 0.017 cm/min (1 cm/hr) reported in Fe-Si [14].

The DAGG boundary migration rate may be compared to other solid-state crystal growth processes *via* SRX/SAGG, most notably the Fujiwara method [61, 62]. In this "strain-anneal" process, a fully-annealed metal is pre-strained (under cold deformation) past the critical strain for static recrystallization. The metal specimen is then slowly inserted into a furnace with a steep temperature gradient, such that a new grain(s) will nucleate on the leading edge of the specimen. As the specimen travels into the furnace, these "leading grains" grow into the cold-deformed microstructure along the steep temperature gradient. These grains can grow to be quite large in size. Single crystals of up to 15 cm were grown in commercial-purity Al by the Fujiwara method, and grains of centimeters in size were similarly grown in an Al-Mg alloy [63]. However, the entry rate of the specimen into the furnace, v_{entry}, is limited by the nucleation of new grains in the cold-deformed microstructure behind the temperature gradient. If v_{entry} is too fast, new grains will nucleate in the cold-deformed microstructure before the grains already growing arrive. This growth does not fit the traditional definition of classical SRX nor SAGG. The cold-deformed microstructure is consumed as in SRX; however, only a few, select grains grow, and this aspect is similar to SAGG. Accordingly, growth during the Fujiwara process may be considered as SAGG with an additional deformation energy driving force. For pure Al, the fastest v_{entry} successfully used in the Fujiwara method is approximately 0.17 cm/min, although rates of 0.03-0.07 cm/min are more typical, at a

furnace temperature of 550°C [61]. These furnace entry rates for Al are approximately an order of magnitude slower than the DAGG boundary migration rate in Mo. Although a comparison of two different metals, single crystals can be produced faster in Mo at $0.66T_M$ through DAGG than in Al at $0.88T_M$ through the method of Fujiwara, which might be considered representative of the fastest type of SAGG. Thus, the rate of grain-boundary migration under DAGG is clearly much faster than even the fastest rates previously demonstrated by other phenomena.

7.2.2 PLASTIC STRAIN ACCUMULATION

The rate of boundary migration in DAGG correlates with plastic true strain accumulation across the flow stress drop, $\Delta\varepsilon_P$. The following is an original analysis of data from the work of Ciulik [3]. The temperature at which the majority of data are available across a DAGG stress drop (nine specimens tested) is 1540ºC. For the PM-A and AM materials tested at 1540ºC, the $\Delta\varepsilon_P$ during the DAGG stress drop is 0.015 with a CI_{95} of ±0.008. The average strain accumulation during the DAGG stress drop in just the five PM-A specimens tested at 1540°C is 0.014 ± 0.004. Strain rate, including rates from 2×10^{-5} to 10^{-4} s^{-1}, has no apparent effect on these values. Thus, the time accumulated over each drop, $t = \Delta\varepsilon_P/\dot{\varepsilon}$, varies from approximately 100 to 800 s, depending on the strain rate.

This analysis of the DAGG stress drop strongly indicates that propagation distance of the DAGG front, the boundary of the abnormal grain, along the coupon gauge length is primarily a function of accumulated plastic strain, not time. This is in stark contrast to SAGG, for which boundary migration distance is a strong function of time at temperature. This result is consistent with recent simulation-based predictions of Holm and co-workers that particle pinning is not effective at preventing growth of abnormal

grains [64]. It is of note that the strain accumulation during the DAGG stress drop decreases to approximately 0.005 ± 0.002 in the PM-A material when temperature is increased to 1640°C; three PM-A specimens were tested at this temperature over strain rates from 2×10^{-5} to 10^{-4} s^{-1}. This indicates that DAGG boundary mobility increases with increasing temperature, as does the temperature dependence of the critical strain for DAGG initiation. These results are not surprising, as mobility is expected to have an Arrhenius dependence upon temperature, generally (Equation 3-3). Plastic straining during DAGG acts to increase average boundary mobility to such an extent that boundary migration distance is a direct function of plastic strain accumulation.

Note that the polycrystalline material is more resistant to plastic straining (i.e. has a much higher flow stress) than the DAGG grain. Therefore, plastic true strain accumulation primarily occurs in the DAGG grain, not the unconsumed polycrystal. Furthermore, the plastic strain accumulation is not a measure of stored defect density in the DAGG grain. Dislocations may annihilate through climb or emission at the free surface of the DAGG grain. As a result, plastic strain accumulation is necessarily a measure of defects generated during the flow stress drop, not those retained. A model for the effect of plastic strain accumulation on boundary mobility is developed in Chapter 8.

7.3 Static Anneals of Halt Specimens

Several PM-B halt specimens which contained DAGG-initiated grains were subsequently *statically* annealed at T=1650°C, the same temperature used to produce DAGG in these specimens during the mechanical halt tests. The purpose of these experiments was to determine if SAGG would occur in DAGG-initiated grains, i.e., if an abnormal grain initiated through DAGG, would it continue to grow under SAGG? A total of six specimens were statically annealed for varying lengths of time, as summarized in

Table 7-1. Specimens B and F underwent a second static anneal. All DAGG grains were indexed using Laue X-ray diffraction, which helped to identify thickness grains and surface grains. For example, X-ray diffraction data proved that the grains visible on the front and back faces of specimen E, Figure 7-7, have two different orientations; these comprise two surface grains, not a single thickness grain. Microstructures produced by this series of anneals are shown in Figures 7-3 through 7-8.

Static abnormal grain growth occurred in specimen, F, as is shown in Figure 7-8, and possibly specimen D, as is shown in Figure 7-6. It should be emphasized that SAGG did not occur in the other four specimens. Thus, SAGG does not regularly occur for DAGG-initiated grains. The crystal orientations of the DAGG grains in specimen F and D are not special within the larger group of DAGG grains orientations from the six specimens. In the following, we explore why only one out of all the DAGG grains subjected to static annealing grew significantly under SAGG.

Specimen	DAGG-initiated Grains	Anneal	Static Abnormal Grain Growth?
A	1 thickness grain	10 min	No
B	1 thickness grain	10 min 30 min	No No
C	1 surface grain	20 min	No
D	1 surface grain	20 min	Maybe
E	2 surface grains	30 min	No
F	1 thickness grain	60 min 60 min	Yes No

Table 7-1: List of static anneals on DAGG-initiated grains.

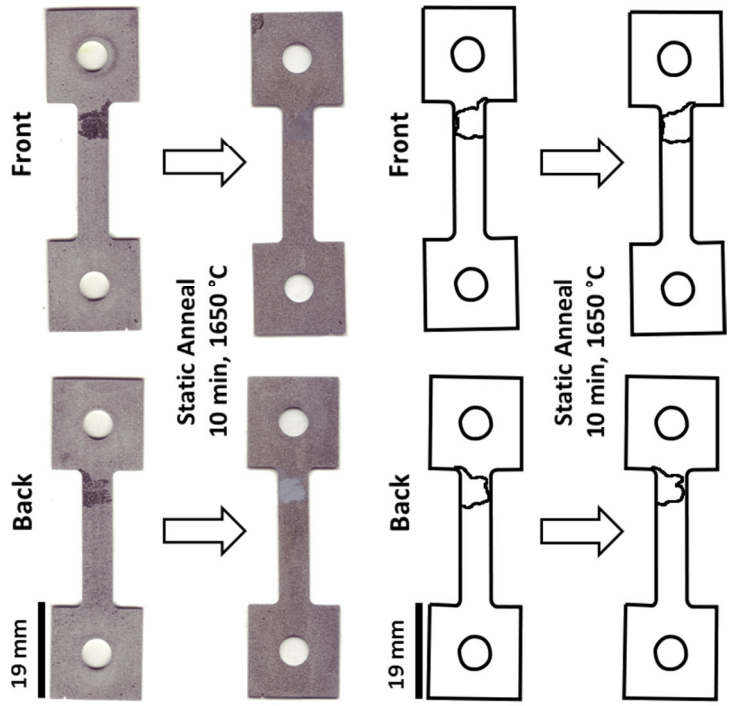

Figure 7-3: Specimen A: 10 min static anneal at 1650ºC. One thickness DAGG grain.

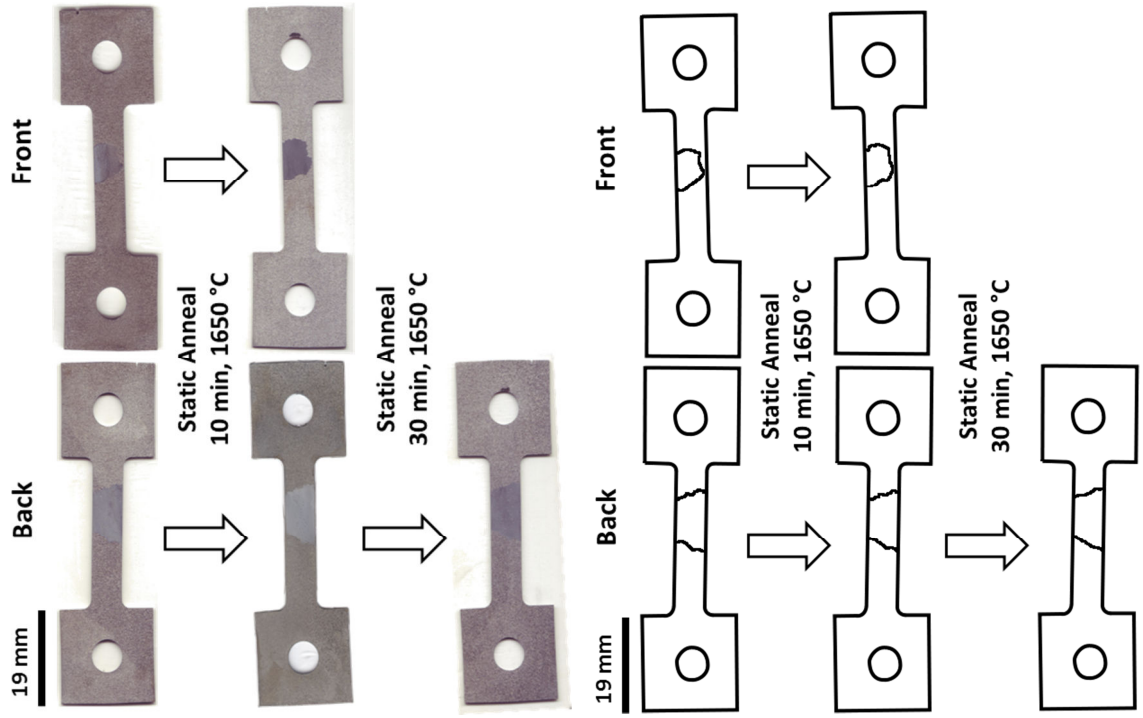

Figure 7-4: Specimen B: 10 min static anneal, followed by a 30 min static anneal at 1650ºC. One thickness DAGG grain.

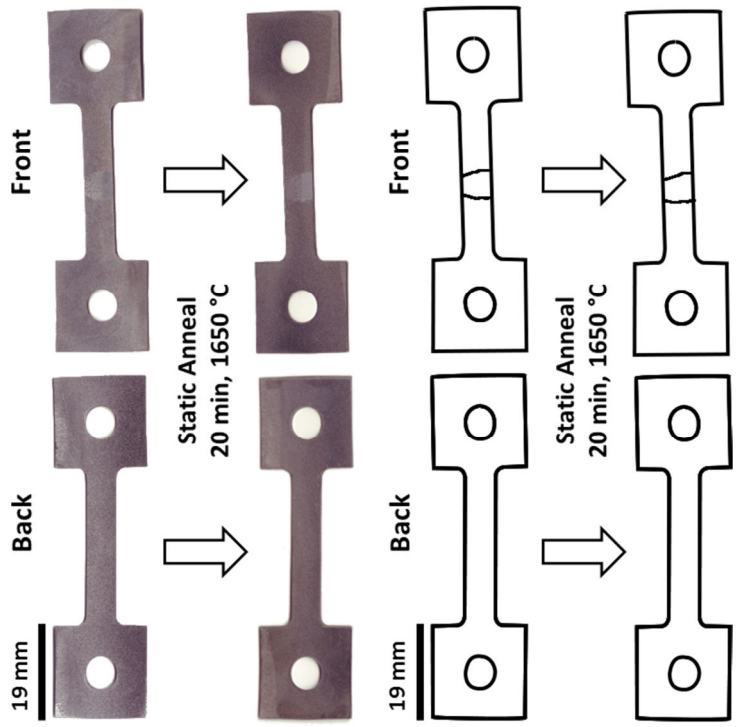

Figure 7-5: Specimen C: 20 min static anneal at 1650ºC. One surface DAGG grain.

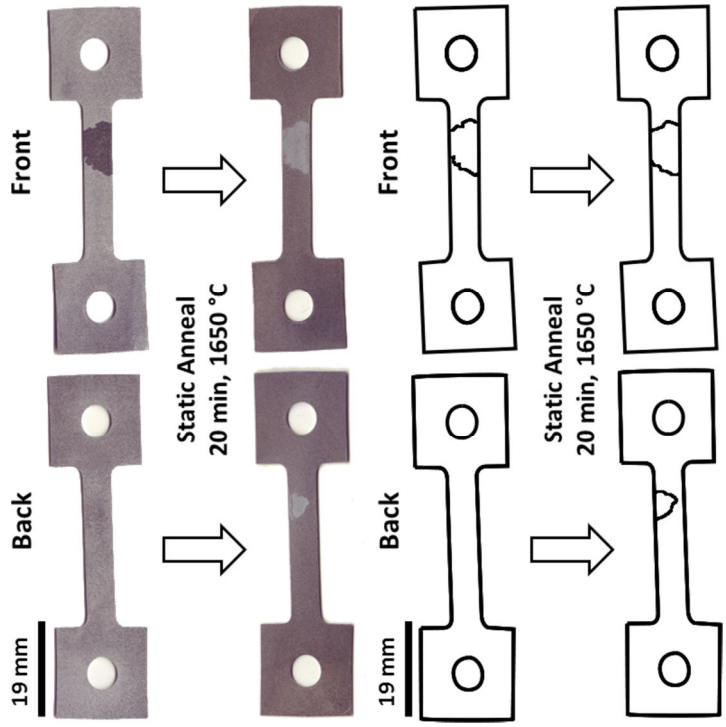

Figure 7-6: Specimen D: 20 min static anneal at 1650ºC. One surface DAGG grain before anneal.

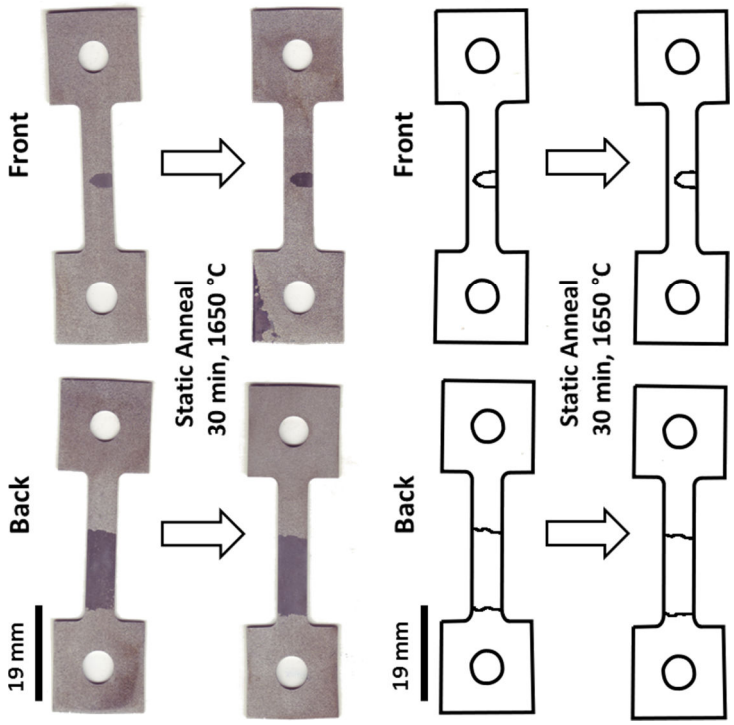

Figure 7-7: Specimen E: 30 min static anneal at 1650ºC. Two surface DAGG grains.

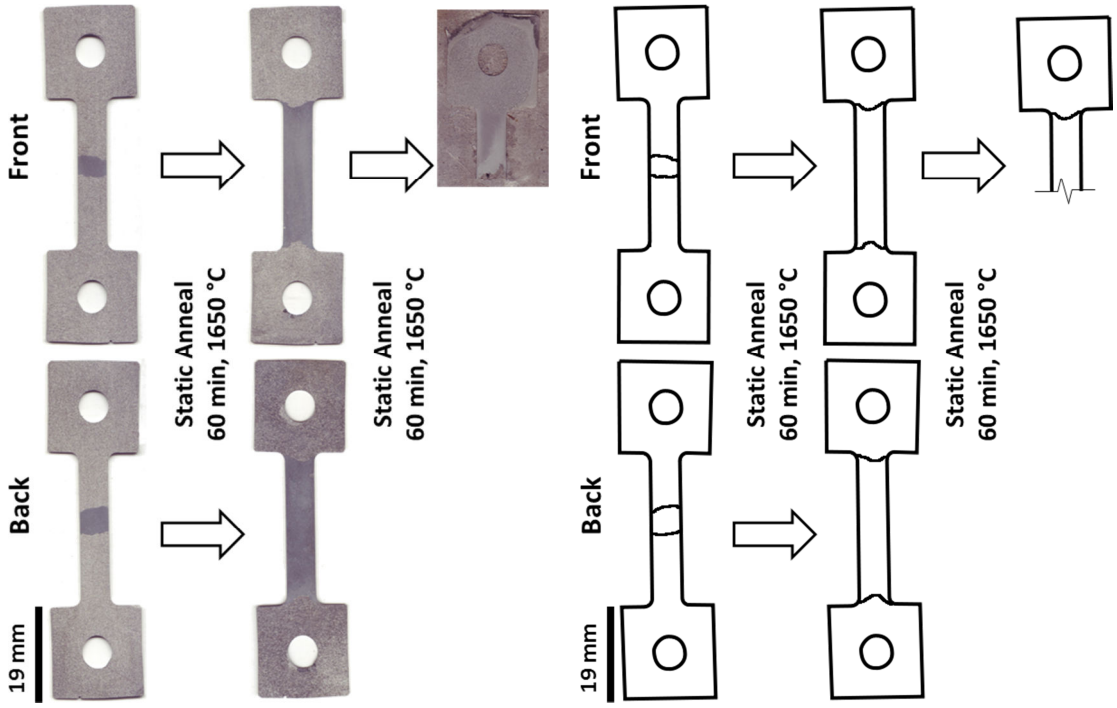

Figure 7-8: Specimen F: 60 min static anneal at 1650ºC. One thickness DAGG grain.

In specimen F, a thickness grain consumed the entire gauge length by SAGG over 60 min at 1650ºC. The growth did not extend into the grip region, even after a second 60 min anneal. The cessation of abnormal growth at the grip region is also characteristic of DAGG. Therefore, a fundamental difference must exist between the hot deformed microstructure of the gauge length and the statically annealed microstructure of the grip. As noted previously in Chapter 6 for the PM-B material, grains become more equiaxed in the hot-deformed region. However, this change in grain aspect ratio occurred in all specimens, A through F; therefore, it is an unlikely source for the SAGG observed in specimen F. Rather, the development of substructure in the hot deformed microstructure is a more likely source. Some of this substructure is retained after the halt specimens are cooled and unloaded; note the substructure shown in the EBSD images of Figure 6-13. Therefore, this residual substructure is initially present during the static annealing of the halt specimens. Substructure represents stored deformation energy, which can provide an additional driving force for grain-boundary migration. If stored deformation energy is important in the SAGG of a DAGG-initiated grain, then it is probably important in DAGG as well. Since growth of the abnormal grain stopped at the boundary of the gauge and grip regions, the actual time required for SAGG to reach this final state in specimen F is not known, other than it must be no longer than the duration of the first anneal. Thus, only a lower bound of SAGG boundary migration rate can be calculated for specimen F: $v_{SAGG} \geq 0.021$ cm/min.

In specimen D, a small SAGG grain appears to have initiated and grown on the back side of the specimen. This abnormal grain appears from an apparently polycrystalline surface after a 20-min static anneal, However, an undetected abnormal grain could have existed near this surface prior to annealing. For example, thickness removal from polishing may have exposed an existing abnormal grain. If the abnormal

grain was produced by SAGG, then a lower bound can be placed on the boundary migration rate; only a lower bound can be calculated because it is not known at what time initiation occurred during the static anneal. This lower bound for SAGG boundary migration rate can be estimated from the exposed grain area, A = 0.17 cm^2, and annealing time, t = 20 min. The abnormal grain is approximately circular; therefore, the growth distance is the radius, $d = r = \sqrt{A/\pi}$, such that $v_{SAGG} \geq \sqrt{\frac{A}{\pi}}/t = 0.012$ cm/min.

No SAGG was observed in specimens A, B, C, and E, i.e. v_{SAGG} = 0. These specimens included both surface grains and thickness grains and had annealing times from 10 to 30 min. It is important to note that if deformation of these specimens was not intentionally halted, but they were instead strained until DAGG completion, the abnormal grains would have undoubtably grown throughout the entire gauge lengths of the specimens. Therefore, SAGG appears to only infrequently occur in DAGG-initiated grains. If SAGG does occur, its boundary migration rate is approximately one order of magnitude slower than for DAGG.

7.4 Chapter Summary

(1) DAGG grains preferentially grow, and likely initiate, along the specimen surface.

(2) The boundary migration rate of DAGG in molybdenum is in the range of 0.64 to 1.28 cm/min. This migration rate is generally two orders of magnitude faster than rates for SAGG reported in the literature for other metals. SAGG did not generally occur in static anneals of DAGG-initiated grains. SAGG must involve a lower boundary mobility or a lower driving force than DAGG, or both. Accordingly, boundary migration during SAGG in molybdenum is slower than during DAGG.

(3) One DAGG-initiated abnormal grain did grow *via* SAGG. This grain only consumed the hot deformed microstructure and growth stopped at the strain-free microstructure in the specimen grip. Therefore, stored deformation energy is a likely driving force for the consumption of the microstructure in SAGG. Because stored deformation energy promotes SAGG, it is likely that it also promotes DAGG. The boundary migration rate during SAGG in this specimen is at least 0.021 cm/min.

(4) The boundary migration distance is a direct function of plastic strain accumulation during DAGG. Accumulation of plastic strain drives the flow stress drop, which corresponds to migration of the boundary during DAGG.

(5) A decreasing critical strain, ε_{CR}, and a decreasing plastic strain accumulation, $\Delta\varepsilon_P$, with increasing temperature indicate that DAGG boundary mobility is temperature dependent.

8 DAGG MECHANISM

Dynamic abnormal grain growth requires plastic straining for initiation and growth. Indeed, it is this aspect of DAGG which distinguishes it from SAGG. The following summarizes the differences between DAGG and SAGG in the PM-B material:

(1) DAGG grains initiated during tensile tests (10^{-4} s^{-1}) at 1650ºC *and* 1800ºC. SAGG grains initiated during static anneals *only* at 1800ºC. Therefore, DAGG initiation occurs at lower temperatures than SAGG initiation.

(2) DAGG grains initiated after straining for 3 to 5 min during tensile tests (10^{-4} s^{-1}) at 1800ºC. SAGG grains initiated at annealing times between 120 and 570 min at 1800ºC. Therefore, DAGG initiation requires a much shorter incubation period than SAGG initiation at the same temperature.

(3) Abnormal grains, which were initiated and grown through DAGG, did not generally grow through SAGG (i.e. static conditions) at the same temperature, 1650ºC. Therefore, DAGG requires dynamic plastic strain for boundary propagation.

(4) For 1800ºC, the largest DAGG grains had a length of 2.5 cm (i.e. the specimen gauge length), and the largest SAGG grains had a length of 0.5 cm.

These differences indicate DAGG is produced by a mechanism involving plastic strain. Plastic strain reduces the incubation period for initiation during DAGG as compared to SAGG. Furthermore, plastic strain accelerates growth of the abnormal grains; many abnormal grain boundaries were observed to only propagate under dynamic conditions. DAGG is enhanced over SAGG by either an additional driving force and/or greater boundary mobility.

8.1 Initiation

During plastic straining, the microstructure evolves into a state which is more favorable to abnormal grain initiation. DAGG initiation occurs at lower temperatures and at shorter incubation times than SAGG initiation. Microstructural features which evolve during plastic straining include grain shape, crystallographic texture, and stored deformation energy. DAGG grains initiated during either transient creep or steady-state creep. Grains elongate and rotate during both transient creep and steady-state creep. Stored deformation energy increases during transient creep and remains constant during steady-state creep. The following discussion concerns the role of grain elongation, texture evolution, and stored deformation energy in DAGG initiation.

Grain elongation does not cause DAGG initiation. PM-B specimens were machined transverse to the rolling direction (T orientation), and PM-A specimens were machined along the rolling direction (L orientation). Accordingly, the aspect ratio of grain size, d_{LTD} / d_{TLD}, decreases in PM-B specimens and increases in PM-A specimens. Because both materials exhibit DAGG, an increase or decrease in d_{LTD} / d_{TLD} does not correlate with DAGG initiation.

Texture evolution (i.e. grain rotation) in the microstructure does not cause DAGG initiation. A very small critical strain, ε_{CR} = 0.02, was observed for DAGG initiation at the highest test temperature of 1800°C. A critical strain of 0.02 at 1800°C allows no significant texture evolution, as indicated in Section 6.2.3. Therefore, texture evolution does not induce DAGG initiation because significant grain rotation is not necessary for DAGG initiation.

Although it may play some role in DAGG initiation, increasing stored deformation energy does not cause DAGG initiation. In the high-temperature tensile

tests, flow stress is used to indicate stored deformation energy in the microstructure prior to DAGG initiation. Hardening occurs (i.e. flow stress increases) due to an increase in dislocation density and the development of subgrains. Note that true strain is not used as a measure of stored deformation energy because defects introduced by plastic strain are removed through dynamic recovery. Flow stress increases during transient creep. As the microstructure approaches steady-state conditions, the hardening rate decreases until the flow stress is constant. In PM-B specimens at 1800°C, DAGG grains initiate during transient creep. In PM-B specimens at 1650°C, DAGG grains generally initiate during steady-state creep. Thus, increasing stored deformation energy is not a cause of DAGG initiation. Stored deformation energy may be a necessary condition for DAGG initiation, but it is clearly not a sufficient condition.

Grain elongation, texture evolution, and increasing stored deformation energy do not cause DAGG initiation. Therefore, some other microstructural feature which evolves during plastic straining causes DAGG initiation. One such feature may be the average grain boundary mobility. In a later section, 8.2.3, we propose that plastic straining increases average grain boundary mobility. While additional experimentation is necessary to prove or disprove this hypothesis, an increase in the average grain boundary mobility could cause DAGG initiation due to the unpinning of boundaries from particles.

8.2 Growth

Initiation involves the selection of a particular grain for DAGG in the microstructure. Once a DAGG grain is selected, rapid growth occurs through the propagation of its boundary. The rapid boundary propagation rate during DAGG could be attributed to (1) a greater driving force on grain boundaries and/or (2) an enhanced mobility of grain boundaries.

8.2.1 DRIVING FORCES

Grains grow under a boundary curvature driving force. Plastic straining may provide additional driving forces on grain boundaries. Possible additional driving forces during DAGG are stored deformation energy and stress-assisted boundary migration (SABM). This section discusses the potential of these driving forces to cause the rapid boundary migration observed during DAGG. The shape of the DAGG front is consistent with a boundary curvature driving force, as discussed in Chapter 7. Therefore, if additional driving forces operate during DAGG, their magnitude is likely not significantly greater than that of the boundary curvature driving force.

Stored deformation energy is competitive with boundary curvature at sufficiently high defect densities, as shown in Table 1-2. Stored deformation energy is retained in the deformed microstructure after a halt test, as shown in the EBSD micrograph in Figure 6-13. If stored energy in the deformed microstructure drives boundary propagation, then growth of a DAGG-initiated grain should continue under static conditions. As discussed in Section 7.4, six halt specimens were statically annealed to test this possibility. DAGG-initiated grains did not grow *via* SAGG except for Specimen F. The abnormal grain consumed the entire deformed microstructure (gauge region) but did not extend into the undeformed microstructure (grip region) in Specimen F. Therefore, stored deformation energy likely promoted consumption of the deformed microstructure in Specimen F. However, five of the six specimens in these experiments exhibited DAGG-initiated abnormal grains which did not grow *via* SAGG. The stored deformation energy density in these specimens was insufficient for SAGG.

Stress-assisted boundary migration (SABM), as illustrated schematically in Figure 8-1, has been observed in bicrystals where an imposed stress drives boundary motion.

This phenomenon has been the subject of recent publications [65-69] and is now addressed with respect to DAGG.

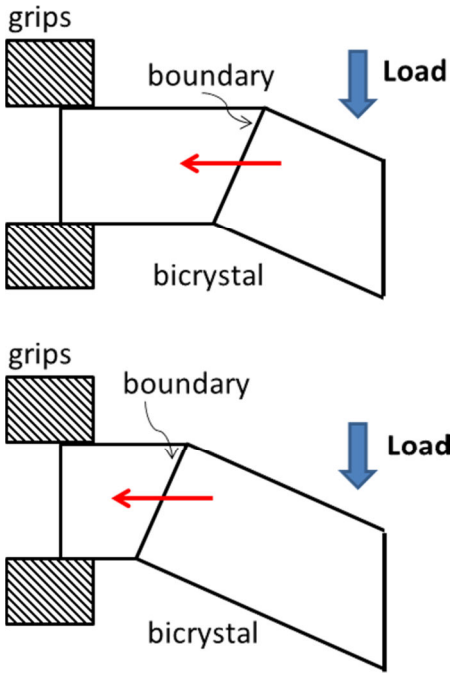

Figure 8-1: Schematic of stress-assisted boundary migration illustrating boundary motion driven by an imposed stress.

Motion of the boundary causes the bicrystal to change shape, that is, a strain is produced. Therefore, the driving force for this phenomenon is provided by energy dissipation W from boundary motion:

$$W = \int \sigma d\varepsilon > 0 \,, \tag{8-1}$$

where σ is the applied stress and ε is the strain produced in the bicrystal. SABM does not accurately describe the observed DAGG phenomenon for the following reasons:

(1) Compatibility constraints exist at grain boundaries in a polycrystalline material, such as the molybdenum studied in the present investigation. Therefore, it is highly unlikely the strain produced by SABM of a boundary for one abnormal grain would be consistent with compatibility at the boundaries of all its surrounding neighbors. Note that this is not an issue with

the bicrystals of SABM experiments that dominate the literature, where free surfaces can deform arbitrarily.

(2) Boundary motion requires the dissipation of energy. It is statistically improbable that the every grain from the polycrystal consumed during DAGG would produce strains that dissipate energy for a DAGG boundary moving in only one direction.

8.2.2 MOBILITY MODEL

It is proposed that plastic straining during DAGG acts to increase average boundary mobility such that boundary migration distance is a direct function of plastic strain accumulation. The following mechanism is proposed as a potential explanation of boundary migration during DAGG. Assume a regular array of sites, such as a dispersion of particles, which can normally pin grain boundaries against migration under static conditions. These sites are separated by an average distance l. When on a boundary, stress will concentrate at these pinning sites as the boundary attempts to migrate, such as when a boundary driving pressure, P, occurs from boundary curvature [30]. Further, assume that this local stress concentration will produce dislocations at a rate R dislocations produced per site per unit time. Finally, assume that after a certain number of dislocations are ejected from a pinning site on the boundary, the boundary will be released to migrate to the next pinning site, an average distance of l away. The rate of boundary unpinning is then proportional to the dislocation generation rate, R, through a constant of proportionality, α, where $1/\alpha$ is the average number of dislocations ejected from one site to unpin the boundary. Boundary unpinning is expected to involve thermally activated processes, which are not specified in the present model, and αR is expected to depend on temperature. Because unpinning and subsequent boundary

migration to the next pinning site are sequential processes, reaction rate theory dictates that the slowest of these will tend to control the average rate of boundary motion. Consider the case in which unpinning is much slower than migration between pinning sites. In this case, the usual relation for average boundary migration rate, $v = MP$ (Equation 3-2), is only useful if the average mobility, M, can be calculated. This is a difficult challenge. Instead, consider the average boundary migration rate as related to the rate of unpinning by dislocation generation, αR, and site spacing,

$$v = \alpha R l \, . \tag{8-2}$$

For migration of a DAGG boundary, dislocations generated at pinning sites must travel through the DAGG grain because of its significantly lower resistance to plastic flow than the polycrystalline material it consumes. Thus, unpinning is directly related to plastic strain accumulation in the DAGG grain. Each dislocation can slip through the DAGG grain to a distance at which it is no longer significant to the moving boundary, effectively annihilating or actually annihilating, such as at a free surface. Define a characteristic length, w, such that the average area swept out by a dislocation through the DAGG grain before annihilation is $A = wl$. The density of dislocation sources, which are pinning sites on the boundary, within the DAGG grain is then $M = \beta/(wl^2)$, where β is a constant related to the geometry of slip. From creep theory [70-72], the strain rate in the DAGG grain is,

$$\dot{\varepsilon} = RAMb \, , \tag{8-3}$$

where b is the magnitude of the Burgers vector. Solving for R produces,

$$R = \frac{\dot{\varepsilon} l}{\beta b} \, . \tag{8-4}$$

The average rate of DAGG boundary migration into the polycrystalline microstructure, from this rate of geometrically-necessary dislocation generation at pinning sites, is then,

$$v = \frac{\alpha l^2}{\beta b}\dot{\varepsilon} \, . \tag{8-5}$$

Integration over time reveals the average DAGG boundary migration distance, $\bar{x}$, to be linearly proportional to plastic strain accumulation,

$$\bar{x} = \frac{\alpha l^2}{\beta b}\varepsilon \, . \tag{8-6}$$

This predicted dependence of boundary migration distance on plastic strain is consistent with the experimental observations. The predicted dependence of boundary migration rate on the spacing of pinning sites suggests that boundary pinning during DAGG may be different from boundary pinning that prevents normal grain growth; compare behaviors of the AM and PM materials, which have very different resistances to normal grain growth but similar boundary migration rates during DAGG. Testing the dependence of v on l predicted by this model will, however, require significant further experimental study.

An important result of this model is that plastic strain accumulation is required for boundary migration, through the increased mobility it causes. Once the DAGG grain penetrates into the grip region, the material at that boundary will no longer accumulate plastic strain. This can explain why DAGG grains do not extend significantly beyond the gage region of tested specimens. While SAGG in specimen F did not extend beyond the gage region because of a driving force requiring strain energy, this may be only the case for SAGG. Thus, strain energy is not necessarily a significant driving force for DAGG, although it may play some role in the overall driving force. It is more likely that the

limitation of DAGG grains to the specimen gage length is a function of strain-assisted mobility, as described by the above model.

8.3 Chapter Summary

Dynamic plastic strain is necessary for both the initiation and growth of abnormal grains during DAGG. Abnormal grains do not initiate or necessarily grow under static conditions in the same material. The driving forces during DAGG are boundary curvature, and possibly, stored deformation energy. It is proposed that the mechanism behind DAGG depends upon a mobility which is enhanced by plastic strain accumulation. A boundary mobility model governed by the rate of unpinning and spacing of pinning sites is proposed to explain an increase in the average boundary mobility.

9 CONCLUSIONS

(1) ***Dynamic Abnormal Grain Initiation*:** Plastic strain accumulation must occur in the microstructure prior to DAGG initiation. DAGG initiation is not controlled by grain elongation, texture evolution, or stored deformation energy. Abnormal grains either 1. initiate sooner v*ia* DAGG than *via* SAGG at higher temperatures or 2. initiate *via* DAGG and do not initiate at all *via* SAGG at lower temperatures.

(2) ***Dynamic Abnormal Grain Growth*:** DAGG grain boundary propagation is a direct function of plastic strain accumulation in the microstructure. The drop in flow stress during DAGG is associated with the transition of the microstructure from polycrystalline to single-crystal forms (i.e. propagation of the DAGG front). These flow stress drops occurred over the same plastic strain interval at a constant temperature despite the strain-rate. DAGG grains prefer to grow, and likely nucleate, at the surface of the specimen.

(3) ***DAGG Grain Orientation:*** DAGG grains exhibited a preference for orientations from a $\langle 101 \rangle$ fiber about the tensile direction, such that: $\{\bar{1}1\bar{1}\}\langle\langle 10\bar{1}\rangle\rangle$ AM DAGG grains grew from a cube recrystallization texture $\{010\}\langle\langle\bar{1}0\bar{1}\rangle\rangle$, rotated 20º clockwise about STD; $\{\bar{1}2\bar{1}\}\langle\langle 10\bar{1}\rangle\rangle$ PM-A DAGG grains grew from a γ-fiber ($\{111\}$ || STD) recrystallization texture; and $\{010\}\langle\langle\bar{1}0\bar{1}\rangle\rangle$ PM-B DAGG grains grew from a cube recrystallization texture $\{010\}\langle\langle\bar{1}0\bar{1}\rangle\rangle$. The preferred orientations are not consistently from majority or minority components of the primary recrystallization texture. The $\{010\}\langle\langle\bar{1}0\bar{1}\rangle\rangle$ PM-B DAGG grains have an orientation which readily produces the plane strain deformation state required by a DAGG thickness grain.

(4) ***DAGG Boundary Migration Rate:*** The rate of DAGG boundary migration in molybdenum is 0.64 – 1.28 cm/min at 1650 ºC. Generally, SAGG was not observed in DAGG-initiated abnormal grains at 1650 ºC. Therefore, SAGG has a lower mobility or driving force than DAGG, and DAGG is significantly faster than SAGG. DAGG is one to two orders in magnitude faster than SAGG observed in other metals and alloys.

(5) ***Driving Forces*:** The driving forces for DAGG are stored deformation energy and boundary curvature. However, stored deformation energy as an additional driving force is not solely responsible for the rapid growth of DAGG. Rather, the mechanism behind DAGG depends upon a mobility which is enhanced by plastic strain accumulation.

(6) ***Mobility Model:*** A boundary mobility model was developed which predicts the experimentally observed linear dependence of DAGG boundary migration distance on plastic strain accumulation. In this model, boundary motion is assumed to be controlled by the rate of boundary unpinning, as mediated by the emission of dislocations from the pinning sites. Additional investigation is necessary to confirm or reject this model.

10 RECOMMENDATIONS FOR FUTURE WORK

DAGG is a scientifically interesting phenomenon which requires additional investigation. The following recommendations provide an experimental outline for future researchers:

(1) Grow DAGG grains to completion during tensile tests over a larger range of strain-rates (10^{-5} s^{-1} to 10^{-2} s^{-1}). The purpose of these tests is to observe the effect of faster strain-rates, as well as to provide additional data to test the mobility model outlined in Section 8.2.2.

(2) Conduct a Transmission Electron Microscopy (TEM) study of the hot deformed molybdenum to characterize pinning particles and deformation substructure.

(3) Test thicker specimens, if thicker sheets (or plates) of molybdenum are available. Thicker specimens may help eliminate some surface effects, and thicker single-crystals may be produced for fundamental property studies. If plate material can be found, uniaxial compression tests at elevated temperature might also be performed to test for the occurrence of DAGG during compression.

(4) Test other body-centered-cubic metals or alloys for DAGG: niobium, tantalum, tungsten, α-iron, and Fe-Si alloys. It would be especially beneficial to observe DAGG in α-iron or Fe-Si because the phenomenon could be characterized at lower test temperatures and the dynamic microstructure could be conceivably quenched.

Appendix A

LIST OF ACRONYMS

AM	Arc-Melted (Ciulik Sheet)
AGG	Abnormal Grain Growth
CDRX	Continuous Dynamic Recrystallization
DAGG	Dynamic Abnormal Grain Growth
DDRX	Discontinuous Dynamic Recrystallization
DGG	Dynamic (Normal) Grain Growth
DRV	Dynamic Recovery
DRX	Dynamic Recrystallization
EBSD	Electron Backscatter Diffraction
GBS	Grain Boundary Sliding
GDRX	Geometric Dynamic Recrystallization
IGA	Instrumental Gas Analysis
IPF	Inverse Pole Figure
LTD	(Specimen) Long Transverse Direction
ND	(Sheet) Normal Direction
ODF	Orientation Distribution Function
OM	Optical Microscopy
PF	Pole Figure
PM-A	Powder Metallurgy (Ciulik sheet)
PM-B	Powder Metallurgy (Worthington sheet)
RD	(Sheet) Rolling Direction
SABM	Stress-Assisted Boundary Migration
SAGG	Static Abnormal Grain Growth
SEM	Scanning Electron Microscopy
SGG	Static (Normal) Grain Growth
SRV	Static Recovery
SRX	Static Recrystallization

STD	(Specimen) Short Transverse Direction
TD	(Sheet) Transverse Direction
TEM	Transmission Electron Microscopy
TLD	(Specimen) Tensile Loading Direction
UTS	Ultimate Tensile Strength
XRD	X-Ray Diffraction
XRF	X-Ray Fluorescence

Appendix B

The following calculations demonstrate that a bcc crystal in sheet form is loaded along a $\langle 101 \rangle$ tensile direction deform under plane strain through slip on only four slip systems if $\langle 100 \rangle$ is normal to the sheet surface. Consider a crystal loaded in a [011] tensile direction. Slip occurs in the $\langle 111 \rangle$ direction on $\{110\}$, $\{112\}$, and $\{123\}$ planes. Slip has been reported for $\{110\}$ and $\{112\}$ planes in molybdenum, where $\{110\}$ is preferred at elevated temperatures and $\{112\}$ is preferred at low temperatures [31]. Let us initially only consider slip on $\{110\}$ planes. The maximum Schmid factor *m* is 0.408 for four slip systems: 1. $(\bar{1}10)[111]$, 2. $(\bar{1}01)[111]$, 3. $(110)[\bar{1}11]$, and 4. $(101)[\bar{1}11]$. Let us label these slip systems as Set A. The eight remaining $\{110\}\langle 1\bar{1}1 \rangle$ slip systems have an *m* of 0 and are not active. The plastic strain states produced by Set A are calculated with Equation 3-10:

$$\underline{\varepsilon}_{crystal}{}^{(1)} = \gamma_1 \begin{bmatrix} -0.408 & 0 & -0.204 \\ 0 & 0.408 & 0.204 \\ -0.204 & 0.204 & 0 \end{bmatrix},$$

$$\underline{\varepsilon}_{crystal}{}^{(2)} = \gamma_2 \begin{bmatrix} -0.408 & -0.204 & 0 \\ -0.204 & 0 & 0.204 \\ 0 & 0.204 & 0.408 \end{bmatrix},$$

$$\underline{\varepsilon}_{crystal}{}^{(3)} = \gamma_3 \begin{bmatrix} -0.408 & 0 & 0.204 \\ 0 & 0.408 & 0.204 \\ 0.204 & 0.204 & 0 \end{bmatrix}, \text{ and}$$

$$\underline{\varepsilon}_{crystal}{}^{(4)} = \gamma_4 \begin{bmatrix} -0.408 & 0.204 & 0 \\ 0.204 & 0 & 0.204 \\ 0 & 0.204 & 0.408 \end{bmatrix}.$$

These slip systems are independent from each other (see Section 3.2.2). The axes for the crystal reference frame are $x_1 = [100]$, $x_1 = [010]$, and $x_1 = [001]$.

A [011] fiber reference frame is now defined with axes $x_1' = [100]$, $x_2' = [0\bar{1}1]$, and $x_3' = [011] \,||\, TLD$. The matrix $\underline{R}$ describes rotation from the crystal reference frame to the [011] fiber reference frame:

$$\underline{R} = \begin{bmatrix} 1 & 0 & 0 \\ 0 & -1/\sqrt{2} & 1/\sqrt{2} \\ 0 & 1/\sqrt{2} & 1/\sqrt{2} \end{bmatrix} \tag{6-7}$$

where $\underline{\varepsilon}_{fiber} = \underline{R}\underline{\varepsilon}_{crystal}\underline{R}^T$. Therefore, slip systems produce the following strains in the [011] fiber reference frame:

$$\underline{\varepsilon}_{fiber}{}^{(1)} = \gamma_1 \begin{bmatrix} -0.408 & 0.144 & -0.144 \\ 0.144 & 0 & 0.204 \\ -0.144 & 0.204 & 0.408 \end{bmatrix},$$
$$\underline{\varepsilon}_{fiber}{}^{(2)} = \gamma_2 \begin{bmatrix} -0.408 & -0.144 & -0.144 \\ -0.144 & 0 & -0.204 \\ -0.144 & -0.204 & 0.408 \end{bmatrix},$$
$$\underline{\varepsilon}_{fiber}{}^{(3)} = \gamma_3 \begin{bmatrix} -0.408 & -0.144 & 0.144 \\ -0.144 & 0 & 0.204 \\ 0.144 & 0.204 & 0.408 \end{bmatrix}, \text{ and}$$
$$\underline{\varepsilon}_{fiber}{}^{(4)} = \gamma_4 \begin{bmatrix} -0.408 & 0.144 & 0.144 \\ 0.144 & 0 & -0.204 \\ 0.144 & -0.204 & 0.408 \end{bmatrix}.$$

Five independent slip systems are necessary to produce an arbitrary strain state. The strain component ε_{22} is zero in $\underline{\varepsilon}_{fiber}{}^{(1)}$, $\underline{\varepsilon}_{fiber}{}^{(2)}$, $\underline{\varepsilon}_{fiber}{}^{(3)}$, and $\underline{\varepsilon}_{fiber}{}^{(4)}$. Therefore, ε_{22} is not an independent strain component. The four independent slip systems produce an R^4 solution space of strain states

$$\underline{\varepsilon}_{fiber\_solutionspace} = \sum_{i=1}^{4} \underline{\varepsilon}_{fiber}{}^{(i)} = \begin{bmatrix} \varepsilon_{11} & \varepsilon_{12} & \varepsilon_{13} \\ \varepsilon_{12} & 0 & \varepsilon_{23} \\ \varepsilon_{13} & \varepsilon_{23} & -\varepsilon_{11} \end{bmatrix}$$

We can solve for shear strains γ_i which produce a uniaxial tensile strain. In a uniaxial tensile test, ε_{12}=ε_{13}=ε_{23}=0 and ε_{11}=ε_{22}=$-\frac{1}{2}\varepsilon_{33}$:

$$\underline{\varepsilon}_{uniaxial\_tension} = \begin{bmatrix} -0.5d & 0 & 0 \\ 0 & -0.5d & 0 \\ 0 & 0 & d \end{bmatrix}.$$

However, this strain state cannot be produced by the slip systems in Set A. Strain states produced by Set A always have an ε_{22} strain component of zero. Therefore, the BCC crystal under uniaxial tension must deform through plane strain:

$$\underline{\varepsilon}_{uniaxial\_tension} = \underline{\Delta\varepsilon} = \begin{bmatrix} -d & 0 & 0 \\ 0 & 0 & 0 \\ 0 & 0 & d \end{bmatrix}$$

Compression occurs in the $[100]$ direction, the $[0\bar{1}1]$ direction has zero strain, and extension occurs in the $[011] \,||\, TLD$. This plane strain deformation is pictured schematically in Figure 6-23 for a cross section parallel to (011). Solving for shear strains γ_i of the four independent slip systems for plane strain deformation:

$$\begin{bmatrix} \gamma_1 \\ \gamma_2 \\ \gamma_3 \\ \gamma_4 \end{bmatrix} = \begin{bmatrix} {\varepsilon_{11}}^{(1)} & {\varepsilon_{12}}^{(1)} & {\varepsilon_{13}}^{(1)} & {\varepsilon_{23}}^{(1)} \\ {\varepsilon_{11}}^{(2)} & {\varepsilon_{12}}^{(2)} & {\varepsilon_{13}}^{(2)} & {\varepsilon_{23}}^{(2)} \\ {\varepsilon_{11}}^{(3)} & {\varepsilon_{12}}^{(3)} & {\varepsilon_{13}}^{(3)} & {\varepsilon_{23}}^{(3)} \\ {\varepsilon_{11}}^{(4)} & {\varepsilon_{12}}^{(4)} & {\varepsilon_{13}}^{(4)} & {\varepsilon_{23}}^{(4)} \end{bmatrix}^{-1} \begin{bmatrix} \Delta\varepsilon_{11} \\ \Delta\varepsilon_{12} \\ \Delta\varepsilon_{13} \\ \Delta\varepsilon_{23} \end{bmatrix},$$

$$\begin{bmatrix} \gamma_1 \\ \gamma_2 \\ \gamma_3 \\ \gamma_4 \end{bmatrix} = \begin{bmatrix} -0.408 & 0.144 & -0.144 & 0.204 \\ -0.408 & -0.144 & -0.144 & -0.204 \\ -0.408 & -0.144 & 0.144 & 0.204 \\ -0.408 & 0.144 & 0.144 & -0.204 \end{bmatrix}^{-1} \begin{bmatrix} -d \\ 0 \\ 0 \\ 0 \end{bmatrix}$$

$$\begin{aligned} \gamma_1 &= 0.612d \\ \gamma_2 &= 0.612d \\ \gamma_3 &= 0.612d \\ \gamma_4 &= 0.612d \end{aligned}.$$

Now, let us consider slip on $\{112\}$ and $\{123\}$ planes. For $\{112\}$ planes, *m* is 0.471 on four slip systems, 0.236 on eight slip systems, and zero on twelve slip systems. For $\{123\}$ planes, *m* is 0.463 on four slip systems, 0.309 on four slip systems, 0.154 on four slip systems, and zero on twelve slip systems. None of these slip systems are independent from the four $\{110\}$ slip systems with an *m* of 0.408. Therefore, slip on $\{112\}$ and $\{123\}$ planes produces the same R^4 solution space of strain states ε_{sub} that slip

on {110} produces. A different set of active slip systems which includes slip on a {112} plane will now be considered. The slip system $(2\bar{1}\bar{1})[\bar{1}\bar{1}\bar{1}]$ has a m of 0.471. If the $(\bar{1}10)[111]$ slip system from Set A is replaced with $(2\bar{1}\bar{1})[\bar{1}\bar{1}\bar{1}]$, then the strain produced by slip system 1 is

$$\underline{\varepsilon}_{fiber}{}^{(1)} = \gamma_1 \begin{bmatrix} -0.471 & 0 & -0.167 \\ 0 & 0 & 0 \\ -0.167 & 0 & 0.471 \end{bmatrix}.$$

Let us keep slip systems 2, 3, and 4 the same and refer to this new set of independent slip systems as Set B. Solving for shear strains γ_i of the four independent slip systems for plane strain deformation:

$$\begin{bmatrix} \gamma_1 \\ \gamma_2 \\ \gamma_3 \\ \gamma_4 \end{bmatrix} = \begin{bmatrix} -0.471 & 0 & -0.167 & 0 \\ -0.408 & -0.144 & -0.144 & -0.204 \\ -0.408 & -0.144 & 0.144 & 0.204 \\ -0.408 & 0.144 & 0.144 & -0.204 \end{bmatrix}^{-1} \begin{bmatrix} -d \\ 0 \\ 0 \\ 0 \end{bmatrix}$$

$$\begin{aligned} \gamma_1 &= 1.061d \\ \gamma_2 &= 0 \\ \gamma_3 &= 0.612d \\ \gamma_4 &= 0.612d \end{aligned}.$$

If the critical shear stress is assumed to be the same for all active slip systems, the slip systems of Set B may be preferred over the slip systems of Set A. This is because slightly less incremental work, $dw = \tau \sum |d\gamma_i|$ [73, p. 127], is expended by slip in Set B than Set A. The summation $\sum|\gamma_i|$ is 2.28d in Set B and 2.48d in Set A. In either case, plane strain deformation conditions exist during uniaxial tensile deformation.

References

[1] F. J. Humphreys and M. Hatherly, *Recrystallization and Related Annealing Phenomena*, 2nd ed. New York: Elsevier Science, 2004.

[2] S. S. Gorelik, *Recrystallization in Metals and Alloys*. Moscow: MIR Publishers, 1981.

[3] J. Ciulik, "Creep and Dynamic Abnormal Grain Growth of Commercial-Purity Molybdenum," Ph.D. Dissertation, Materials Science and Engineering, University of Texas at Austin, Austin, TX, 2005.

[4] J. Ciulik and E. M. Taleff, "Power-law creep of powder-metallurgy grade molybdenum sheet," *Materials Science and Engineering: A,* vol. 463, pp. 197-202, 2007.

[5] J. Ciulik and E. M. Taleff, "Dynamic abnormal grain growth: A new method to produce single crystals," *Scripta Materialia,* vol. 61, pp. 895-898, 2009.

[6] A. D. Rollett, A. P. Brahme, and C. G. Roberts, *Materials Science Forum,* vol. 558-559, pp. 33-42, 2007.

[7] J. Wadsworth, T. G. Nieh, and J. J. Stephens, "Recent Advances in Aerospace Refractory Metal Alloys," *International Materials Reviews,* vol. 33, pp. 131-150, 1988.

[8] A. Gilbert, W. R. Warke, and B. A. Wilcox, "Fractography of polycrystalline molybdenum," *Journal of the Less Common Metals,* vol. 7, pp. 222-227, 1964.

[9] A. Kumar and B. L. Eyre, "Grain boundary segregation and intergranular fracture in molybdenum," *Proceedings of the Royal Society of London,* vol. A370, 1980.

[10] W. C. Coons, *The Metal Molybdenum*. Cleveland, OH: American Society for Metals, 1958.

[11] J. W. Pugh, "On the Short Time Creep Rupture Properties of Lamp Wire," *Metallurgical Transactions,* vol. 4, pp. 533-538, 1973.

[12] P. K. Wright, "The high temperature creep behavior of doped tungsten wire," *Metallurgical and Materials Transactions A,* vol. 9, pp. 955-63, 1978.

[13] K. Tanoue, "Roles of Potassium Bubbles in High Temperature Creep Resistance of Doped Tungsten Fine Wires," *Materials Science Forum,* vol. 426-432, pp. 4277-4282, 2003.

[14] J. E. May and D. Turnbull, "Secondary Recrystallization in Silicon Iron," *Trans. AIME,* vol. 212, pp. 770-781, 1958.

[15] R. D. Doherty, D. A. Hughes, F. J. Humphreys, J. J. Jonas, D. Juul Jensen, M. E. Kassner, W. E. King, T. R. McNelley, H. J. McQueen, and A. D. Rollett, "Current issues in recrystallization: a review," *Materials Science and Engineering: A,* vol. 238, pp. 219-274, 1997.

[16] A. Dehghan-Manshadi and P. D. Hodgson, "Dynamic Recrystallilzation of Austenitic Stainless Steel under Multiple Peak Flow Behaviours," *ISIJ International,* vol. 47, pp. 1799-1803, 2007.

[17] S. Agarwal, P. E. Krajewski, and C. L. Briant, "Dynamic Recrystallization of AA5083 at 450° C: the Effects of Strain Rate and Particle Size," *Metallurgical and Materials Transactions A,* vol. 39, pp. 1277-1289, 2008.

[18] J. F. Shackelford, *Introduction to Materials Science for Engineers*, 5th ed. Upper Saddle River, NJ: Prentice-Hall, Inc., 2000.

[19] A. D. Rollett, D. J. Srolovitz, and M. P. Anderson, "Simulation and Theory of Abnormal Grain Growth-- Anisotropic Grain Boundary Energies and Mobilities," *Acta Metallurgica,* vol. 37, pp. 1227-1240, 1989.

[20] T. H. Courtney, *Mechanical Behavior of Materials*, 2nd ed. Long Grove, IL: Waverland Press, Inc., 2000.

[21] O. D. Sherby and P. M. Burke, "Mechanical behavior of crystalline solids at elevated temperature," *Progress in Materials Science,* vol. 13, pp. 325-390, 1967.

[22] B. Walser and O. D. Sherby, "The Structure Dependence of Power-Law Creep," *Scripta Metallurgica,* vol. 16, pp. 213-219, 1982.

[23] C. R. Barrett and O. D. Sherby, "Influence of Stacking-Fault Energy on High-Temperature Creep of Pure Metals," *Transactions of the Metallurgical Society of AIME,* vol. 233, pp. 1116-1119, 1965.

[24] R. R. Vandervoort, "On the Possible Influence of Stacking Fault Energy on the Creep of Pure Bcc Metals," *Transactions of the Metallurgical Society of AIME,* vol. 245, pp. 2269-2272, 1969.

[25] M. A. Meyers, J. C. La Salvia, and B. K. K. Nesterenks, in *REX '96 The Third Inter Conference on Recrystallization and Related Phenomena*, Monterey, CA, 1997, pp. 279-286.

[26] B. Zhang, P. S. Bate, and N. Ridley, "The Effect of Strain Rate History on the Dynamic Grain Growth Behaviour of AA 5083," *Materials Science Forum,* vol. 551-552, pp. 627-632, 2007.

[27] K. B. Hyde and P. S. Bate, "Dynamic grain growth in Al-6Ni: Modelling and experiments," *Acta Materialia,* vol. 53, pp. 4313-4321, 2005.

[28] B.-N. Kim, K. Hiraga, Y. Sakka, and B.-W. Ahn, "A Grain-Boundary Diffusion Model of Dynamic Grain Growth During Superplastic Deformation," *Acta Metallurgica,* vol. 47, pp. 3433-3439, 1999.

[29] J. R. Seidensticker and M. J. Mayo, "Dynamic and Static Grain Growth During the Superplastic Deformtion of 3Y-TZP," *Scripta Materialia,* vol. 38, pp. 1091-1100, 1997.

[30] G. Gottstein and L. S. Shvindlerman, *Grain Boundary Migration in Metals: Thermodynamics, Kinetics, Applications*, 1st ed. Boca Raton, FL: CRC Press, 1999.

[31] W. F. Gale and T. C. Totemeir, Eds., *Smithells Metals Reference Book*. Oxford, UK: Elsevier Butterworth-Heinemann, 2004, p.^pp. Pages.

[32] D. Yesilleten and T. A. Arias, "Atomic-level physics of grain boundaries in bcc molybdenum," *Physical Review B,* vol. 64, 2001.

[33] D. A. Porter and K. E. Easterling, *Phase Transformations in Metals and Alloys*, 2nd ed. Workingham, Berkshire, UK: Van Nostrand Reinhold (UK) Co. Ltd, 1981.

[34] G. I. Taylor, "Plastic Strain in Metals," *Journal Institute of Metals,* vol. 62, pp. 307-324, 1938.

[35] R. Von Mises, "Mechanik der plastischen Formänderung von Kristallen," *Zeitschrift für Angewandte Mathematik und Mechanik,* vol. 8, pp. 161-184, 1928.

[36] A. D. Rollett and S. I. Wright, "Typical Textures in Metals," in *Texture and Anisotropy*, U. F. Kocks, C. N. Tome, and H.-R. Wenk, Eds., ed Cambridge, U.K.: Cambridge University Press, 1998, pp. 178-238.

[37] H. Kurishita, Y. Kitsunai, Y. Hiraoka, T. Shibayama, and H. Kayano, "Development of Molybdenum Alloy with High Tougness at Low Temperatures," *Materials Transactions, Japan Institute of Metals,* vol. 37, pp. 88-97, 1996.

[38] E. A. Gulbransen, K. F. Andrew, and F. A. Brassart, "Oxidation of Molybdenum 550°C to 1700°C," *Journal of the Electrochemical Society,* vol. 110, pp. 952-959, 1963.

[39] P. E. Blackburn, M. Hoch, and H. L. Johnston, "The Vaporization of Molybdenum and Tungsten Oxides," *The Journal of Physical Chemistry,* vol. 62, pp. 769-773, 1958.

[40] Y. Hiraoka, T. Fujii, T. Kainuma, M. Okada, and R. Watanabe, in *Physical Metallurgy and Technology of Molybdenum and its Alloys, AMAX*, Ann Arbor, MI, 1985, pp. 81-86.

[41] T. Fujii, R. Watanabe, Y. Hiraoka, and M. Okada, "Preparation of a Large-Scale Molybdenum Single-Crystal Sheet by Means of Secondary Recrystallization," *Journal of the Less Common Metals,* vol. 96, pp. 297-304, 1984.

[42] Y. Hiraoka, T. Fujii, T. Kainuma, M. Okada, and R. Watanabe, "Mechanical Properties of Molybdenum Single Crystals Produced by Means of Secondary Recrystallization," *Journal of Nuclear Materials,* vol. 133-134, pp. 332-336, 1985.

[43] C. L. Briant, F. Zaverl, and E. L. Hall, "Warm Rolling of Sintered Tungsten Ingots," *Materials Science and Technology,* vol. 7, pp. 923-936, 1991.

[44] C. L. Briant, F. Zaverl, and W. T. Carter, "The Effect of Deformation on Abnormal Grain Growth in Tungsten Ingots," *Acta Metallurgica,* vol. 42, pp. 2811-2821, 1994.

[45] R. L. Barto and L. J. Ebert, "Deformation stress state effects on the recrystallization kinetics of molybdenum," *Metallurgical Transactions,* vol. 2A, pp. 1643-1649, 1971.

[46] A. International, "Standard Test Methods For Determining Average Grain Size," vol. Standard Designation E 112-9, ed. 100 Barr Harbor Drive, P.O. Box C700 West Conshohocken, PA 19428-2959: ASTM International, 1996.

[47] C. S. Barrett and T. B. Massalski, *Structure of Metals*, 3rd ed. New York: Pergamon, 1980.

[48] P. Cotterill and P. R. Mould, *Recrystallization and Grain Growth in Metals*. New York: John Wiley & Sons, 1976.

[49] T. E. Tietz and J. W. Wilson, *Behavior and Properties of Refractory Metals*. Stanford, CA: Stanford University Press, 1965.

[50] P. E. Armstrong and H. L. Brown, "Dynamic Young's Modulus Measurements above 1000°C on Some Pure Polycrystalline Metals and Commercial Graphites," *Trans. AIME,* vol. 230, pp. 962-966, 1964.

[51] J. Askill and D. H. Tomlin, "Self-diffusion in molybdenum," *Philosophical Magazine,* vol. 8, pp. 997-1001, 1963.

[52] W. F. Hosford, *The Mechanics of Crystals and Textured Polycrystals*. Oxford, UK: Oxford University Press, 1993.

[53] U. F. Kocks, "Simulation of Deformation Textures for Cubic Metals," in *Texture and Anisotropy*, U. F. Kocks, C. N. Tome, and H.-R. Wenk, Eds., ed Cambridge, U.K.: Cambridge University Press, 1998, pp. 390-419.

[54] L. Vitos, A. V. Ruban, H. L. Skriver, and J. Kollar, "The surface energy of metals," *Surface Science,* vol. 411, pp. 186-202, 1998.

[55] O. Enger and V. Randle, *Texture Analysis: Macrotexture, Microtexture, and Orientation Mapping*, 2nd ed. Boca Raton, FL: CRC Press, 2010.

[56] S. I. Wright, G. T. Gray III, and A. D. Rollett, "Textural and Microstructural Gradient Effects on the Mechanical Behavior of a Tantalum Plate," *Metallurgical and Materials Transactions A,* vol. 25A, pp. 1025-1031, 1993.

[57] H. Klein, C. Heubeck, and H. J. Bunge, "Inhomogeneous Textures in Tantalum Sheets," *Materials Science Forum,* vol. 157-162, pp. 1423-1434, 1994.

[58] H. Jiang, T. R. Bieler, C. Compton, and T. L. Grimm, "Cold rolling evolution in high purity niobium using a tapered wedge specimen," *Physica C: Superconductivity,* vol. 441, pp. 118-121, 2006.

[59] R. A. Vandermeer and J. C. Ogle, "The Development of Rolling Texture in a Nb(Cb)-40 Pct V Alloy," *Metallurgical and Materials Transactions B,* vol. 1, pp. 1461-1463, 1970.

[60] J. F. Bingert, B. L. Henrie, and D. L. Worthington, "Three-Dimension Characterization of Incipiently Spalled Tantalum," *Metallurgical and Materials Transactions A,* vol. 38A, pp. 1712-1721, 2007.

[61] T. Fujiwara and T. Hudita, *Journal of Science Hiroshima University,* vol. 8, p. 239, 1938.

[62] T. Fujiwara and K. Koizumi, *Journal of Science Hiroshima University,* vol. 16, p. 81, 1952.

[63] N. A. Pedrazas, "Solid-State Production of Single-Crystal Aluminum and Aluminum-Magnesium Alloys," Master of Science in Engineering, Department of Mechanical Engineering, University of Texas at Austin, Austin, TX, 2010.

[64] E. A. Holm, A. D. Hoffman, A. D. Rollett, and C. G. Roberts, "Particle-assisted grain growth," in *Recrystallization and Grain Growth, 2010*, Sheffield, UK, To appear.

[65] M. Winning, G. Gottstein, and L. S. Shvindlerman, "Stress induced boundary motion," *Acta Materialia,* vol. 49, pp. 211-219, 2001.

[66] M. Winning, G. Gottstein, and L. S. Shvindlerman, "Migration of grain boundaries under the inflluence of an external shear stress," *Materials Science and Engineering: A,* vol. A317, pp. 17-20, 2001.

[67] M. Winning, G. Gottstein, and L. S. Shvindlerman, "On the mechanisms of grain boundary migration," *Acta Materialia,* vol. 50, pp. 353-363, 2002.

[68] J. W. Cahn and J. E. Taylore, "A unified approach to motion of grain boundaries, relative tangential translation along boundaries, and grain rotation," *Acta Materialia,* vol. 52, pp. 4887-4898, 2004.

[69] J. W. Cahn, Y. Mishin, and A. Suzuku, "Duality of dislocation content of grain boundaries," *Philosophical Magazine,* vol. 86, pp. 1-11, 2006.

[70] J. Weertman, "Steady-State Creep through Dislocation Climb," *Journal of Applied Physics,* vol. 28, pp. 362-364, 1957.

[71] J. Weertman, "Steady-State Creep of Crystals," *Journal of Applied Physics,* vol. 28, pp. 1185-1189, 1957.

[72] J. Weertman, "Creep of Indium, Lead, and Some Of Their Alloys with Various Metals," *Trans. Met. Soc. AIME,* vol. 218, pp. 207-218, 1960.

[73] W. F. Hosford, *Mechanical Behavior of Materials*, Second Edition ed. Cambridge, UK: Cambridge University Press, 2010.

[74] R. Brautigan, "A Short Story About Contemporary Life in California," in *Revenge of the Lawn*, ed New York: Houghton Mifflin Company, 1963.

Vita

There are thousands of stories with original beginnings. This is not one of them.

-Richard Brautigan in A Short Story About Contemporary Life in California [74, p.26]

Daniel Lee Worthington is from Lafayette, California, a suburb of San Francisco. During his years at Campolindo High School, he was interested in sketching, painting, programming, web publishing, and video games. He enrolled as a Computer Science major upon admission to the University of California, Davis. After realizing he enjoyed his physical science and engineering classes much more than programming, he changed his major and began undergraduate research on metal matrix composites. Other academic activities as an undergraduate included building an underwater remotely operated vehicle, interning at Los Alamos National Laboratory in New Mexico, and deriving impurity diffusivities in ferrite from first-principles calculations. He earned a B.S. in Mechanical Engineering and Materials Science in 2007 from UC Davis, and immediately began graduate studies at the University of Texas at Austin.

dlworthington@gmail.com

This dissertation was typed by the author.